UNIVERISTY OF TECHNOLOGY SYDNEY

THE EFFECT OF SURFACE DEFECTS ON THE OPTICAL AND ELECTRICAL PROPERTIES OF ZnO NANORODS

by

Suranan Anantachaisilp

A thesis submitted in partial fulfilment for
the degree of Doctor of Philosophy

in the

School of Mathematics and Physical Sciences

Faculty of Science

2015

Declaration of Authorship

I, Suranan Anantachaisilp, declare that this thesis titled, "The Effect of Surface Defects on the Optical and Electrical Properties of ZnO Nanorods" and the work presented in it is my own. I confirm that: This work was done wholly or mainly while in candidature for a co-tutelle research degree at this University and the Mahidol University.

- Where any part of this thesis has previously been submitted for a degree or any other qualification at this University and Mahidol University or any other institution, this has been clearly stated.

- Where I have consulted the published work of others, this is always clearly attributed.

- Where I have quoted from the work of others, the source is always given.

- With the exception of such quotations, this thesis is entirely my own work.

- I have acknowledged all main sources of help.

- Where the thesis is based on work done by myself jointly with others, I have made clear exactly what was done by others and what I have contributed myself.

Signed:_____

Suranan Anantachaisilp

Date:_____

ABSTRACT

This thesis reports on the effect of native point defects on both the NH_3 gas sensing properties and the surface electronic structure of ZnO nanorods. Low temperature hydrothermal growth at 90°C was utilised to synthesize ZnO nanorods approximately 55 ± 5 nm in diameter. The type and density of intrinsic surface defects on the ZnO nanorod was controlled using post growth annealing in O_2 gas and Zn vapor environments. Low voltage cathodoluminescence (CL) spectroscopy confirmed that the heat treatment process produced different surface defect structures. The as-grown, O_2, and Zn annealed nanorods exhibited broad CL peaks centered at 1.90 eV (YL), 1.70 eV (RL), and 2.44 eV (GL), which were attributed to O interstitials or Li_{Zn} deep acceptors, acceptor-like V_{Zn} complexes, and donor-like V_O related centers, respectively.

The first part of this thesis focuses on the influence of deep level surface defects on NH_3 gas response of ZnO nanorods. Electrical and gas sensing measurements revealed that the NH_3 gas sensitivity was 4.1 for the as-grown (YL), 22.6 for O_2 anneal (RL), and 1.4 for Zn vapor anneal (GL) samples. Hydrogen plasma treatment quenched the RL and inverted the ammonia electrical response due to the incorporation of shallow hydrogen donors. Changes to the gas sensing response were attributed to a shift in the ZnO Fermi level position relative to the ammonia gas chemical potential due to the formation near surface donor or acceptor centers.

In the second part of this thesis the effect of native point defects on the surface electronic structure of all ZnO nanorod samples was studies utilizing X-ray photoemission spectroscopy (XPS), X-ray Absorption Near-Edge Structure (XANES), electron spin resonance (ESR), low voltage CL spectroscopy, sub band gap photoluminescence (PL) spectroscopy and electrical I-V measurements. Correlative characterization measurements established that the degree of surface band bending and surface conductivity is controlled by the amount of adsorbed ambient gas species (O_2, H_2O and OH), which is mediated by type and concentration of intrinsic surface point defects.

The last part of this thesis concentrates on the chemical origin of RL peak and its optical properties. A wide range of analysis techniques, including PL and CL

spectroscopy, XANES and ESR was used to comprehensively characterize the RL emission. From these data, the RL has been assigned to highly lattice coupled V_{Zn}-related acceptor-like center. No correlation was found between the RL and nitrogen impurities.

KEY WORDS: ZnO NANORODS, HYDROTHERMAL GROWTH, SURFACE
                        ELECTRONIC PROPERTIES, GAS SENSING PREOPERTIES, RED
                        LUMINESCENCE

ACKNOWLEDGEMENTS

CONTENTS

CONTENTS (cont.)

CONTENTS (cont.)

CONTENTS (cont.)

CONTENTS (cont.)

LIST OF PUBLICATIONS

Refereed Journal Publications

S. Anantachaisilp, S.M. Smith, C. Ton-That, S. Pornsuwan, A.R. Moon, C. Nenstiel, A. Hoffmann, M.R. Phillips, Nature of Red Luminescence in Oxygen Treated Hydrothermally Grown Zinc Oxide Nanorods, *Journal of Luminescence*, **168** (2015) 20-25.

S. Anantachaisilp, S.M. Smith, C. Ton-That, T. Osotchan, A.R. Moon, M.R. Phillips, Tailoring Deep Level Surface Defects in ZnO Nanorods for High Sensitivity Ammonia Gas Sensing, *The Journal of Physical Chemistry C*, **118** (2014) 27150-27156.

Matthew R. Phillips, Suranan Anantachaisilp, Liangchen Zhu, Laurent L. Cheong Lem, Christian Nenstiel, Siwaporn Meejoo Smith, Cuong Ton-That, Axel Hoffmann, Visible Luminescence in Bulk and Nanostructured ZnO (Invited Paper), *2014 SPIE Photonics West*, San Francisco, California, USA. February 1–6, 2014.

Conference Presentations

S. Anantachaisilp, S.M. Smith, C. Ton-That, T. Osotchan, A.R. Moon, M.R. Phillips, ZnO Nanowires with Enhanced Sensitivity for Ammonia Gas Sensing at Room temperature by Regulating Deep Level Surface Defects. *2014 MATERIALS RESEARCH SOCIETY Fall Meeting & Exhibit*, Boston, Massachusetts. November 30-December 5, 2014.

Matthew Phillips, Suranan Anantachaisilp, Liangchen Zhu, Christian Nenstiel, Nadja Jankowski, Siwaporn Meejoo Smith, Cuong Ton-That and Axel Hoffrnann, Chemical Origin of Red Luminescence in Zn. *8th International Workshop on Zinc Oxide and Related Materials*, Niagara Falls, Ontario, Canada. September 8 - 11, 2014.

LIST OF TABLES

LIST OF FIGURES

LIST OF FIGURES (cont.)

LIST OF FIGURES (cont.)

LIST OF FIGURES (cont.)

LIST OF FIGURES (cont.)

LIST OF FIGURES (cont.)

LIST OF FIGURES (cont.)

LIST OF SCHEMES

LIST OF ACRONYMS

A^0	Neutral acceptor
BB	Band bending
BX	Bound exciton
CB	Conduction band
CC	Configurational coordinate
CCD	Charge-coupled device
CL	Cathodoluminescence
D^0X	Neutral donor bound exciton
DAP	Donor-acceptor pair
DL	Deep level
EPR	Electron paramagnetic resonance
ESR	Electron spin resonance
FBT	Free-to-bound transition
FWHM	Full width at half maximum
FX	Free exciton
GL	Green luminescence
HMT	Hexamethylene tetramine
$I\text{-}V$	Current-Voltage

LIST OF ACRONYMS (cont.)

LO	Longitudinal optical
NBE	Near band edge
OL	Orange luminescence
PL	Photoluminescence
RL	Red luminescence
S	Sensitivity
sccm	standard cubic centimetres per minute
SEM	Scanning electron microscopy
TEY	Total electron yield
TFY	Total fluorescence yield
UV	Ultra-violet
VB	Valence band
XANES	X-ray absorption near edge spectroscopy
XPS	X-ray photoelectron spectroscopy
XRD	X-Ray diffraction
YL	Yellow luminescence

CHAPTER I
INTRODUCTION TO ZnO

Metal-oxide semiconductors are widely acknowledged as crucial technological materials for the development of novel electronic and photonic devices.[1] ZnO is one of the metal oxide semiconductors which has attracted great attention in this field because of its wide band gap (3.44 eV at low temperature and 3.37 eV at room temperature), large exciton binding energy (60 meV) and the ease of growth of its nanostructures on a variety of substrates. Consequently, ZnO has emerged as an important potential candidate as a functional material applicable in variety of novel nano-devices.[2-4] Furthermore, ZnO nanomaterials of different morphologies; such as nanorods, nanowires, nanotubes, nanobelts and nanoparticles, show great potential as enabling materials in broad range of applications, such as field effect transistors, optically pumped lasers, photodetectors, optical switches and sensors due to their unique and exciting electronic, optical and piezoelectric properties.[5] In addition, ZnO nanostructures have also received much attention for chemical detection applications owing to the strong sensitivity of its surface conductivity to the presence of adsorbed species.[6] Gas sensors, pressure sensors and biosensors are based on the change in conductance with the reversible chemisorption process of reactive gases on the ZnO surface, piezoelectric property, biocompatibility and nontoxicity of ZnO, respectively.[7]

However, numerous promising applications of ZnO critically depend upon the development of growth and processing techniques to control the concentration and distribution of the bulk and surface point defects [8-9] that mediate the optical and electrical properties.[10] Of equal importance is the establishment of methods to regulate the surface morphology of ZnO nanostructures because it is well known that the surface-to-volume ratio also has a significant effect on the material's physical properties.

1.1 Motivation of the Research

One of the most widely emitted gases in our atmosphere is ammonia (NH_3) gas. It is emitted from both its natural origin as well as direct and indirect human activities. There are variety of ammonia sources including the chemical industry. It is commonly utilized in the production of petrochemicals, fertilizer and paper as well as used as a refrigerant in commercial refrigeration, food and beverage industry, air-conditioning, pharmaceuticals production, and in power plants. However, it has a substantial effect on both environment and our health which need to be concern. It is one cause of global warming. In addition, it has a high toxicity when anhydrous ammonia mixes with water. The human respiratory system has a high moisture content and therefore anhydrous ammonia is easily mixed with water and irritates or burns the respiratory tract depending on the concentration. It also causes chronic lung disease. The level of ammonia in all industries needs to be detected for which an ammonia gas sensor has been used. An ammonia gas sensor is also used in medical applications. For example, some diseases such as kidney disorders or stomach ulcers caused by *Helicobacter pylori* bacterial stomach infection, are diagnosed by measuring the ammonia levels in exhaled air.[11-13] Table 1.1 shows a summary of ammonia gas sensor applications.

Recently, semiconducting metal oxide materials have been extensively utilized as the gas sensors due to their low cost. ZnO is one of the most promising ammonia gas sensors since it is chemically and thermally stable. It operates on the change of conductance principle after gas molecules are adsorbed on the sensing layers. However, use of ZnO as an ammonia gas sensor still need development. In some ammonia gas sensor applications, high sensitivity, short response time and ability to operate at low temperatures is required, as shown in Table 1.1. In order to improve the electrical response of ZnO nanostructures, the nanostructural properties (morphology, particle size and surface area) as well as the carrier concentration need to be controlled.[14-18] In addition, the surface point defects have a significant effect on the gas sensitivity. However, the exact role of the surface point defects on the surface conductivity remains controversial. This research therefore focuses mainly on a study of the relationship between the surface point defects and the ammonia gas sensing properties.

Table 1.1: Summary of ammonia gas sensor applications Taken from Timmer *et al.*[19]

Application	Detection limit	Require response time	Temperature range	Remarks
Environmental				
Monitoring ambient condition	0.1 ppb to >200ppm[20]	Minutes	0-40 °C	Reduce environmental pollution
Measure in stables	1 to >25 ppm[21]	~ 1 min	10-40 °C	Protect livestock animals and farmers
Automotive				
Measure NH_3 emission from vehicles	4->200 g/min[22] (concentration unknown)	Seconds	Up to 300 °C	NH_3 emission is not regulated at this time
Passenger cabin air control	50 ppm[23]	~1 s	0-40 °C	Automotive air quality sensor mainly aim on NO_X and CO levels[21]
Detect ammonia spill	1-100 ppm[24]	Seconds	Up to 600 °C	Control Urea injection in SCR NO_X reduction
Chemical				
Leakage alarm	20->1000 ppm[23, 25]	Minutes	Up to 500 °C	Concentrations can be very high at NH_3 plants and can even be explosive
Medical				
Breath analysis	50-2000 ppb[11, 13]	~ 1 min	20-40 °C	Diagnosis of peptic ulcer cause by bacteria, small gas volumes

The surface electronic structure of all samples with different types of defects are also studied in order to understand the mechanisms of gas adsorption as well as the interactions between native point defects and ambient gas species. These provide more information about the role of surface point defects which are useful for gas sensor applications.

The O_2 annealed ZnO sample emitted red luminescence (RL) provides the highest NH_3 gas sensitivity and the chemical origin of RL is still under debate, the chemical origin of this peak and its optical properties were comprehensively studied.

1.2 Objectives of the Research

This research mainly focuses on the systematic introduction of different types of surface point defects in ZnO nanorods through controlled growth and thermal processing in oxidizing (O_2) and reducing (Zn vapor) atmosphere. ZnO nanorods having surface defects of various types were further employed for fabrication of gas sensing devices and their electrical responses to gas exposure probed and compared with the native point defect on the surface. In this work, ammonia gas was employed as a model of a reductive gas in order to illustrate the inter-relationships between deep level surface defects, electrical properties, and sensing performance in ZnO nanorods.

The following are the summary of the main objectives of this research:

- To introduce various types of surface point defects into low temperature hydrothermally grown ZnO nanorods systematically
- To investigate the influence of the deep level surface point defects on electrical and gas sensing properties of ZnO nanorods
- To investigate the effect of native point defects on the surface electronic structure of ZnO nanorods
- To investigate the chemical origin of the RL peak and its optical properties

1.3 Thesis Outline

This thesis mainly focuses on the role of surface defects on the physical properties in ZnO nanorods. The thesis is structured as follow:

Chapter 1 gives a general introduction to ZnO and provides a brief overview of utilizing ZnO as a semiconductor gas sensor. In addition, it provides the motivation as well as the objectives of the research. The final section of this chapter presents the outline of the thesis.

A literature review is provided in chapter 2. It presents some fundamental properties of ZnO, including physical, chemical, optical, electrical, and gas sensing properties. The relationship between defects and optical transitions in ZnO is introduced. It also includes the characteristics of gas sensor and the gas sensing mechanisms of ZnO. Finally, some of ZnO nanostructures synthesis methods are presented.

Chapter 3 provides a full description of chemical and experimental details utilized in this work: details of chemicals and instruments, sample preparation and post growth processing, and details of each characterization technique.

Chapter 4, 5, and 6 present the experimental results and discussions. Chapter 4 focuses on the influence of deep level surface defects on the electrical and ammonia gas sensing properties of ZnO nanorods. Chapter 5 studies the effect of native point defects on the surface electronic structure of ZnO nanorods. Chapter 6 mainly investigates the nature of red luminescence in O_2 annealed ZnO nanorods.

Chapter 7 provides the general conclusions of the research.

CHAPTER II

OPTICAL, ELECTRICAL, AND GAS SENSING PROPERTIES OF ZnO AND ITS SYNTHESIS: LITERATURE REVIEWS

In this chapter, an overview of ZnO properties including physical, chemical, optical, electrical, and gas sensing properties are provided. In the first section, the details of ZnO defects and their formation processes are given. The effect of defects on the optical properties is also discussed. A history of ZnO gas sensors and their sensing mechanism are introduced as well. In the last section, some of the ZnO nanostructures synthesis methods are presented.

2.1 Physical and Chemical Properties of ZnO

ZnO is a binary II-VI direct wide band gap semiconductor with large exciton binding energy. It mostly crystallizes in hexagonal wurtzite structure under ambient conditions. General physical and chemical properties of ZnO are demonstrated in Table 2.1.

Table 2.1: General physical and chemical properties of ZnO

Physical and chemical properties	Values
Molar mass	81.408 g/mol
Density	5.606 g/cm^{-3}
Melting point	1975°C (decomposes)
Solubility	0.16 mg/100 ml (at 300K)
Crystal system	Wurtzite (at 300K)
Space group	*P6₃mc*
Lattice constant: *a*	3.2496 Å
c	5.2065 Å

Energy gap	3.37 eV (at 300K)
Exciton binding energy	60 meV (at 300K)
Intrinsic carrier concentration	$<10^6$ cm^{-3} (max n-type doping $>10^{20}$ cm^{-3}) electrons
Electron effective mass	$m_e^* = 0.24\, m_e$
Electron Hall mobility for low n-type conductivity	200 cm^2/V·s (at 300K) $m_h^* = 0.59\, m_e$
Hole effective mass	5.50 cm^2/V·s (at 300K)
Hole Hall mobility for low p-type conductivity	

2.1.1 Crystal Structure

In particular, binary II-VI compounds have strong ionic bonding and wide band gaps. By contrast, ZnO has stronger covalent bonding than ionic bonding leading to strong crystal strength. ZnO has three main crystal structures which are rocksalt (B1), zinc blende (B3), and wurtzite (B4) as displayed in Figure 2.1. B1, B3, and B4 are strukturbericht symbols utilized to identify crystal structures. The crystal structure of ZnO depends on its environment. Among all crystal structures, wurtzite structure is the most thermodynamically stable phase of ZnO compared with other possible crystal structures. This also confirms that covalent bonding is dominating because tetrahedral coordination in wurtzite structure is representative of sp^3 covalent bonding.

In ZnO wurtzite crystal structure, there are two atoms per unit cell. It consists of two hexagonal close packed sub-lattices; HCP Zn^{2+} and HCP O^{2-} stacking along the c-axis. The lattice parameters are $a = 3.2495$ Å and $c = 5.2069$ Å.[26] The hexagonal wurtzite ZnO has an open structure where Zn atoms occupy half of the tetrahedral sites. While the octahedral sites are empty; thus, there are many sites for ZnO to accommodate intrinsic defects and extrinsic dopants.[27]

In wurtzite ZnO, there are four interested face terminations; the nonpolar m $(10\bar{1}0)$ face, the semipolar a $(11\bar{2}0)$ face as well as the polar c (0001)-Zn and $(000\bar{1})$-O faces. Between the two polar surfaces, the chemical and physical properties are different. The polar c surfaces are flat and stable since there is no reconstruction.[28] By comparison, the semipolar a face is less stable and has rougher surface than the polar c

and the nonpolar *m* faces. These different properties have significant effects on the ZnO nanostructures growth processes.
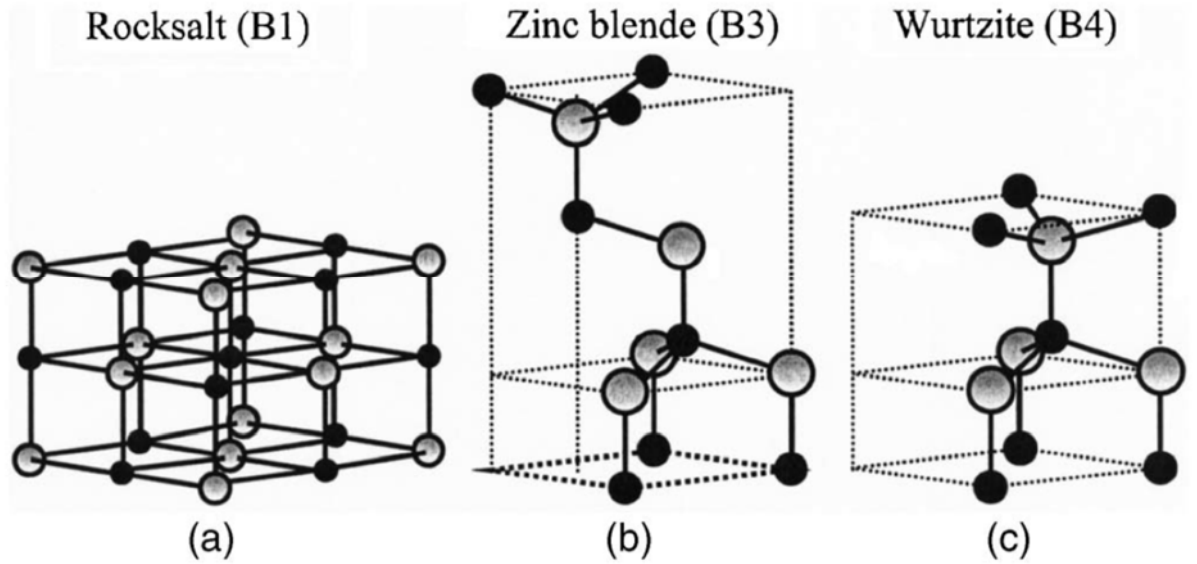
Figure 2.1: Unit cells of ZnO crystal structures: (a) cubic rocksalt (B1), (b) cubic zinc blende (B3), and (c) hexagonal wurtzite (B4). Zn atoms are represented in gray whereas O atoms are represented in black.[29]

2.1.2 Electronic Band Structure

The electrical properties of semiconductors can be defined by the electronic band structure since they relate to crystal translational order. Understanding the band structure, consequently, is necessary to incorporate materials in device applications. A number of theoretical methods with varying complexity have been utilized to calculate the electronic band structure of ZnO.

ZnO is a direct and wide band-gap semiconductor with a high exciton binding energy ($E_b = 60 \; meV$). The ZnO band gap is 3.37 eV at room temperature and 3.44 eV at low temperature. The calculation of its band structure is shown in Figure 2.2a.The band structure is located along high symmetry lines in hexagonal Brillouin zone. Since ZnO is a direct band gap semiconductor, its highest valence band maximum and lowest conduction band minimum sit at the Γ-point of the Brillouin zone. The conduction band is s-like two-fold degenerate containing the empty zinc 4s orbital whereas the valence band is p-like consisting of the fully occupied oxygen 2p orbitals.[30]

The benefits of its wide band gap are high breakdown voltages, ability to sustain large electric fields, low noise enervation, and high temperature and high power operation.[29]
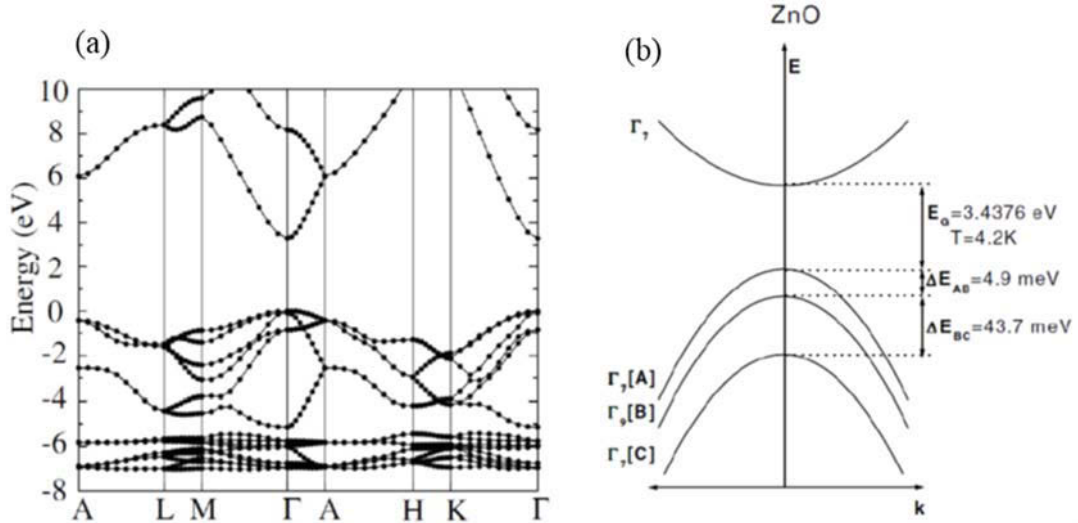
Figure 2.2: (a) The calculation of ZnO band structure using the HSE hybrid functional. The valence-band maximum energy is at zero. (b) Hexagonal ZnO band structure and symmetries. The valence band splits into three sub-bands; A, B, and C resulting from the effects of crystal-field splitting and spin-orbit coupling.[31-32]

Due to the effects of crystal-field splitting and spin-orbit coupling, the valence band of ZnO is split into three sub-band states; A, B, and C (Figure 2.2b). The A and C sub-bands have Γ_7 symmetry while the B posses Γ_9 symmetry.[32] The valence band order of these three sub-bands is Γ_7-Γ_9-Γ_7 which is consistent with Δ_{so}.[33] The energetic differences of these sub-bands are $\Delta_{AB} = 4.9\ meV$ and $\Delta_{BC} = 43.7\ meV$.[32]

The electronic band structure depends on temperature and pressure. The band gap at Γ point expands with decrease in temperature. The band gap temperature dependence can be described by the following empirical relationship.[34]

$$E_g(T) = E_g(T = 0) - \frac{\alpha T^2}{T+\beta} \qquad (2.1)$$

where $E_g(T)$ is the energy gap at temperature T, $E_g(T = 0)$ is the energy gap at 0 K, α and β are the temperature coefficients for which $\alpha = 5.05 \times 10^{-4}$ eV K^{-1} and β = -900 K for temperature up to 300 K.[35]

2.1.3 Defect Chemistry

Defects play an important role in the performance and reliability of semiconductors; therefore, understanding the role of defects on the physical properties

of these materials is essential for their development and improvement.[36] Like other semiconductors, the applications of ZnO also depend upon the control of defects as well as their associated charge carriers. Before studying ZnO defects and the effect of the defects on its properties in depth, it is important to know the basic of crystal lattice defects or imperfections. Defects in materials can be classified by their dimension.[37]

3D-Defects

The 3-dimensional defects; volume or bulk defects, are the aggregation of atoms or vacancies. This type of defect can be categorized into 4 classes by their size and effect on the materials properties. First are precipitates, small particles distributed in the lattice through solid state reaction increasing the strength of materials. Dispersants are a second type of volume defects. They are larger particles which can be large precipitates, grains, or polygranular particles distributed in the microstructure. Inclusions are another type of 3-dimensional defects which are extraneous particles or large precipitate particles with undesirable components in microstructure. The last type of bulk defects are voids or pores which are gases bubbles or clustering of vacancies in solid state, decreasing the materials strength.

2D-Defects

Interfaces or planar defects are called 2-dimensional defects. This type of defects are caused by the distortion in a crystal across the plane divided into 2 main types; stacking fault and grain boundary.

A stacking fault is usually found in close packed structures - face centre cubic (FCC) and hexagonal closed pack (HCP). It occurs due to the change in stacking sequence over a few atomic planes. In the FCC structure, the normal arrangement ABCABCABC can be changed to ABCAB_ABC causing by stacking fault. The pattern ABABABAB of HCP arrangement is broken into ABABA_AB which also known as a stacking fault.

A grain boundary is another type of planar defects. The interface of small crystallites or grains are called as grain boundaries. The atoms in the boundary regions are often in poor arrangement causing an irregular growth to the solid during crystallization. They are generally found in polycrystalline materials and have a significant effect on the mechanical properties of materials.

1D-Defects

The 1-dimensional defects; dislocations or line defects, are the deviation of an entire row of lattice points row from a perfect pattern; they are usually undesirable. and always act as electrical defects in semiconductors and optical materials. Line defects consist of two major types; edge dislocation and screw dislocation.

An edge dislocation happens when an extra half-plane of atoms terminates in the midway of a crystal causing the distortion in the adjacent planes of atoms. In order to preserve the arrangement of crystal planes on both sides, the extra plane breaks and joins bonds around the edge of the terminating plane. In this type of dislocation, the Burgers vector; the magnitude and direction of distortion in the crystal lattice, is perpendicular to the dislocation line.

A screw dislocation is more difficult to visualize. It is formed by a similar method as the edge dislocation but in a helical path. Unlike an edge dislocation, the Burgers vector is parallel to the dislocation line.

0D-Defects

Point defects are defined as 0-dimensional defects since they disturb the crystal structure at only one point or around one lattice point. Point defects can be divided into two groups which are intrinsic defects and extrinsic defects. Intrinsic defects in a pure material consist of vacancies, interstitials as well as antisites. On the other hand, extrinsic defects are initiated by another host atom or impurity atom called substitutional or impurities. In semiconductors, point defects play an important role on their various electronic and optical properties. Defects have been investigated for several decades in bulk semiconductors; however, their role in nanostructured materials is the subject of recent research. In particular, the impact of surface defects on the physical properties of nanostructures requires further investigation owing to the small length scales and large surface-to-volume ratio.[27] Despite its simple formula, ZnO has very rich defect chemistry[38] with native vacancy and interstitial point defects and inadvertently included impurities such as hydrogen and lithium being the major centres. Moreover in nanostructured ZnO, as established in this thesis, surface point defects have a major effect on its electronic and optical properties.
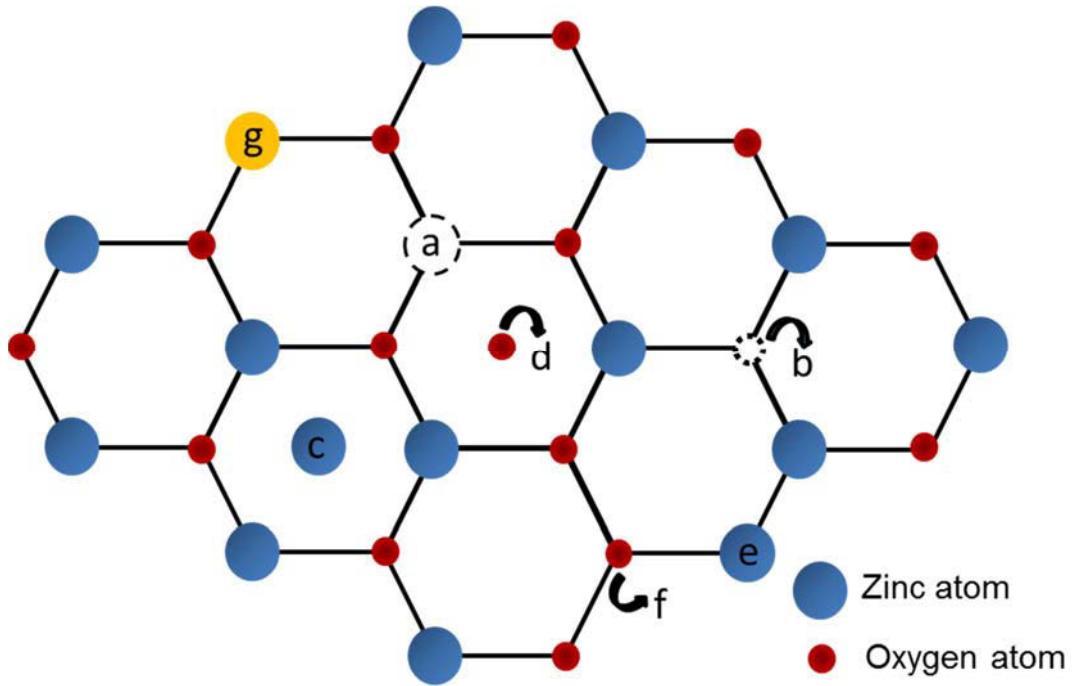
Figure 2.3: Illustration of point defects in ZnO crystal structures: (a) Zinc vacancy V_{Zn}, (b) Oxygen vacancy V_O, (c) Zinc interstitial Zn_i, (d) Oxygen interstitial O_i, (e) Zinc antisite Zn_O, (f) Oxygen antisite O_{Zn} and (g) Substitutional impurity at a zinc site e.g. Li_{Zn}, Cu_{Zn} or Al_{Zn}.

2.1.3.1 Vacancies

A vacancy is an intrinsic defect which is formed when some atoms are missing from their normal lattice sites in crystal. In all crystalline materials, vacancies mostly appear in high concentration. They also have an effect on the atoms migration in the crystal lattice.[30] They can diffuse through the lattice after filling by neighbouring atoms. The surrounding crystal structure needs to be stabilized to avoid vacancy collapse. The common vacancies in ZnO are zinc (V_{Zn}) and oxygen (V_O) vacancies where zinc and oxygen atoms are absent from the ZnO lattice, respectively (Figure 2.3a and b). Furthermore, they are the most prevalent defects in ZnO.
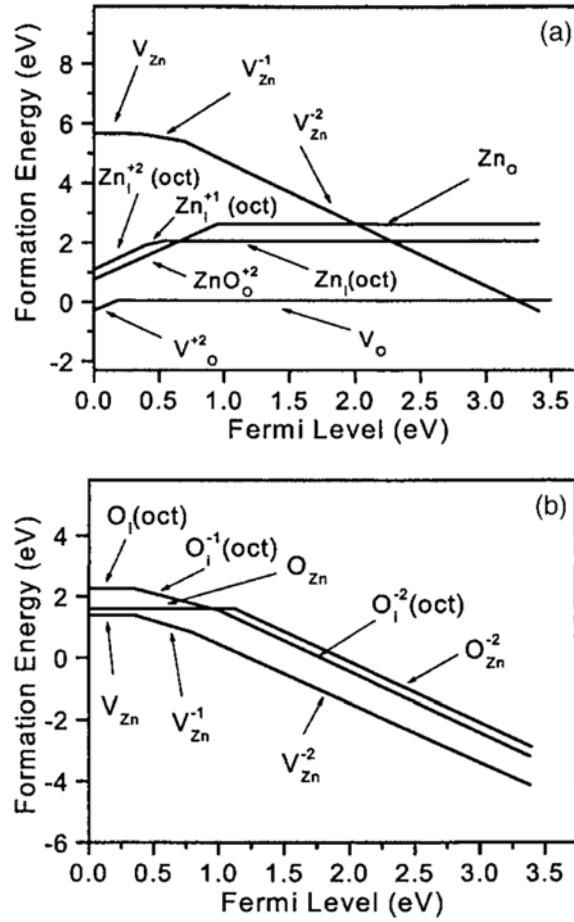
Figure 2.4: Calculated defect formation energy for ZnO native point defects in (a) Zinc-rich conditions and (b) Oxygen-rich conditions.[39]

Zinc vacancies (V_{Zn}) electronic structure in ZnO can be modelled by utilizing molecular orbital theory. V_{Zn} involves four O dangling bonds and six electrons. The absence of a Zn atom in ZnO lattice makes V_{Zn} an acceptor. It can receive up to two additional electrons. V_{Zn} is much easier to form in *n*-type than *p*-type ZnO due to the very high formation energies in *p*-type ZnO.[34] In an oxygen-rich condition, V_{Zn} is the dominant species among other point defects in *n*-type ZnO. Between the three charge state configurations; V_{Zn}^0, V_{Zn}^-, and V_{Zn}^{2-}, the most favourable V_{Zn} species is V_{Zn}^{2-} because of its lowest formation energy as shown in Figure 2.4(b). According to a first principle calculation, 0/1- and 1-/2- charge states transitions of V_{Zn} deep acceptors exist at 0.1-0.2 eV and 0.8-1.2 eV above the valence band maximum, respectively.[29, 33, 40-41] Consequently, a transition from the conduction band or a shallow donor to the V_{Zn} deep acceptor would emit luminescence in the range of 2.2-2.6 eV, which is green. Thus the green luminescence is typically attributed to V_{Zn}.[33, 42-43]

An Oxygen vacancy (V_O) is a deep donor defects. It is the most dominant species in zinc-rich conditions owing to its lowest formation energies even if comparing with interstitial zinc (Zn_i) as presented in Figure 2.4(a). The electronic structure of V_O is also able to be explained by molecular orbital theory similar to V_{Zn}. It contains four Zn dangling bonds and two electrons. According to this simple model, there are three possible charge states which are doubly occupied (neutral; V_O^0), singly occupied (+1; V_O^+), and empty (+2; V_O^{2+}). The stability of charge states depends upon the Fermi level position in the bandgap. The formation energy of V_O^+ is much higher than that of V_O^0 and V_O^{2+} in all Fermi levels; hence, V_O is recognized as a negative-U defect and V_O^+ is always thermodynamically unstable.[44] According to a first principle calculation, 0/2+ charge states transition of V_O deep donors occurs at approximately 0.5-0.8 eV above the valence band maximum.[45-46] The 0/2+ transition level has been estimated to be around 1-2 eV below the conduction band minimum by band gap estimation error of local density approximation.[47-49] The broad green luminescence band centred in the range of 2.4-2.5 eV is usually assigned to 2+/0 state transition of V_O.[39, 50-52]

2.1.3.2 Interstitials

An interstitial is also an intrinsic defect where an atom occupies an interstitial site; a lattice site on which an atom does not normally appear. Interstitials are moderately unusual defects since they are high energy defects. In most crystalline materials, the interstitial sites are quite small in size and rarely have a bonding configuration.[30] Zinc (Zn_i) and oxygen (O_i) interstitials are regular interstitials in ZnO which are shown in Figure 2.3c and d.

A Zinc interstitial (Zn_i) is a shallow donor defect which can occupy in both tetrahedral and octahedral sites in the wurtzite ZnO. However, it is more stable at the octahedral site because of fewer geometrical constraints.[34] In n-type ZnO, Zn_i has a high formation energy even under zinc-rich conditions (Figure 2.4a). By comparison, the formation energy of Zn_i^{2+} is much lower in p-type ZnO resulting in a possible source of charge compensation in p-type ZnO.[53] Zn_i also has a very low migration barrier of 0.57 eV making it is unstable and highly mobile at room temperature.[35, 42] In addition, Zn_i generally form complexes with impurities due to its high formation energy and mobility.

An Oxygen interstitial (O_i) is a deep acceptor defect. It can occupy the octahedral or tetrahedral interstitial sites or form split interstitials.[34] Nevertheless, the tetrahedral site is unstable. O_i in this site also freely relaxes into a split-interstitial configuration. The O_i atom stays in a lattice site with one of the nearest-neighbour O atoms. O_i which occupy the octahedral site ($O_i(oct)$) are electrical active interstitials. $O_i^{2-}(oct)$ which can accept two electrons has the lowest formation energy compared with $O_i(oct)$ and $O_i^{1-}(oct)$ as presented in Figure 2.4b. The deep acceptor transition levels for the 0/1- and 1-/2- charge states are at 0.72 and 1.59 eV above the valence band maximum.[35]

2.1.3.3 Antisites

An Antisite is one type of intrinsic defect which is found in compounds containing weakly ionized atoms. This energetically allows atoms to exchange sites; therefore, an A-atom can sit on the lattice spot of B-atom or vice versa, where A and B are atoms in host material. The antisites in ZnO are zinc (Zn_O) and oxygen (O_{Zn}) antisites, as displayed in Figure 2.3e and f. Both Zn_O and O_{Zn} have high formation energies (Figure 2.4a and b); thus, they have less influence than other native defects.

A Zinc antisite (Zn_O) is a double donor defect in *n*-type ZnO. The transitions of Zn_O are located in the conduction band. This type of defect can split into Zn_i and V_O resulting from its migration. In *n*-type ZnO, the dissociation barrier of Zn_O^{2+} into Zn_i^{2+} and V_O^0 is around 1.3 eV.[35]

An Oxygen antisite (O_{Zn}) is a deep acceptor defect which is rarely found under equilibrium conditions. Nonetheless, it can be formed under non-equilibrium conditions *e.g.* under irradiation and ion implantation. The transition levels 0/1- and 1-/2- of O_{Zn} are at 1.52 and 1.77 eV above the valence band maximum, respectively.[35] The splitting of O_{Zn} into V_{Zn} and O_i requires higher migration barrier than that of vacancies or interstitials.

2.1.3.4 Impurities

An impurity is an extrinsic point defect which forms by introducing external atoms into the host material. It can be either a substitutional or an interstitial defect depending on its occupational site. Substitutional impurities are created when external atoms occupy a lattice site while an external atom occupies an

interstitial site for interstitial impurities. Due to the small size of interstitial sites, large atoms are regularly substitutional whereas small atoms frequently fill in interstitial sites.[30] If the impurities have different charges from that of host lattice ion, the excess charge is compensated by a paired vacancy or interstitial via a charge compensation mechanism to maintain overall charge neutrality. In semiconductors, impurities play an important role on most of engineering properties especially electrical properties by introducing donor or acceptor levels in the band gap. The substitutional atoms with a different charge from the host semiconductor serve as electron donors or acceptors. In order to control ZnO conductivity, donor and acceptor impurities have been doped into ZnO. The common shallow donor impurities which have been doped into ZnO are aluminium (Al), gallium (Ga), indium (In), fluorine (F) and hydrogen (H). Lithium (Li), sodium (Na), copper (Cu) and nitrogen (N) are some examples of acceptor impurities usually doped in ZnO. Figure 2.3g shows the diagram of a substitutional impurity at a zinc site in ZnO lattice e.g. Li_{Zn}, Cu_{Zn} or Al_{Zn}.

The impurities introduced into ZnO create new energy levels in the band gap which associated with excitons bound to impurities. The new energy levels can be observed by the additional luminescence peaks. For instance, the fine structure luminescence centred at around 2.4 eV is introduced by copper impurities; the yellow-orange luminescence centred at 2.1 eV is related to excitons bound to lithium impurities at a zinc site (Li_{Zn}).[54-55]

2.1.3.5 Formation Energies and Processes of Native Defects

Native point defects have a strong effect on electrical and optical properties of a semiconductor and, of course, on ZnO. In order to succeed in the use of ZnO devices applications, it is important to understand how the defects are incorporated into ZnO. The formation energies and their processes, transition between charge states as well as migration, allow us to predict point defect concentrations and know their incorporation during growth and processing. The formation energies and electronic structure of native point defects in ZnO; V_{Zn}, V_O, Zn_i, O_i, Zn_O, and O_{Zn}, were calculated by Janotti et al.[35] and Kohan et al.[33] using a first principle, plane-wave pseudopotential technique with a supercell approach. Under thermodynamic equilibrium and no defect-defect interaction, the concentration of point defects (c) depends upon its formation energy (E^f) which can be calculated by the following equation:

$$c = N_{sites}\exp\left(-\frac{E^f}{k_BT}\right) \tag{2.2}$$

where N_{sites} is the number of sites in the crystal where the defect can take place, k_B is the Boltzmann constant, and T is the temperature. According to equation 2.2, the defects with high formation energies rarely form while the defects with the low formation energies form in high equilibrium concentration. For a point defect in charge state (q), the formation energy is computed as

$$E^f(q) = E^{tot}(q) - n_{Zn}\mu_{Zn} - n_O\mu_O - qE_F \tag{2.3}$$

where $E^{tot}(q)$ is a total energy of a system, n_{Zn} and n_O are the number of zinc and oxygen atoms, μ_{Zn} and μ_O are zinc and oxygen chemical potentials, and E_F is the Fermi energy.

The chemical potential is related to the growth conditions; Zn-rich, O-rich or in between. μ_{Zn} is equal to $\mu_{Zn(bulk)}$ in a Zn-rich condition and μ_O is also equal to its bulk chemical potential ($\mu_{O(bulk)}$) in an O-rich condition. In intermediate ratios between zinc and oxygen, both μ_{Zn} and μ_O are less than their bulk chemical potential ($\mu_{Zn(bulk)}$ and $\mu_{O(bulk)}$). Note that Zn and O chemical potentials are in equilibrium with ZnO: $\mu_{Zn}+\mu_O < \mu_{ZnO}$.

The intrinsic point defects, in general, have low formation energies; therefore, they usually form during growth processes. The formation energies of ZnO native points defects; V_{Zn}, V_O, Zn_i, O_i, Zn_O, and O_{Zn}, are presented in Figure 2.5. These formation energies and charge transition levels were calculated from first principles.

Most of defects are electrically active. They typically produce levels in the semiconductors band gap including transitions between different charge states in the same defect.[56] The energy levels of defects in different charge states can also be calculated from first principles derived from the formation energy calculation. The defect transition levels $\varepsilon(q/q')$ in the calculations are defined as the Fermi-level positions for which the formation energies of q and q' charge states are equal. $\varepsilon(q/q')$ can be calculated by equation 2.4.

$$\varepsilon(q/q') = \frac{E^f(D^q;E_F=0)-E^f(D^{q'};E_F=0)}{q'-q} \tag{2.4}$$

where $E^f(D^q; E_F = 0)$ is the defect D in the charge state q formation energy when $E_F = 0$.
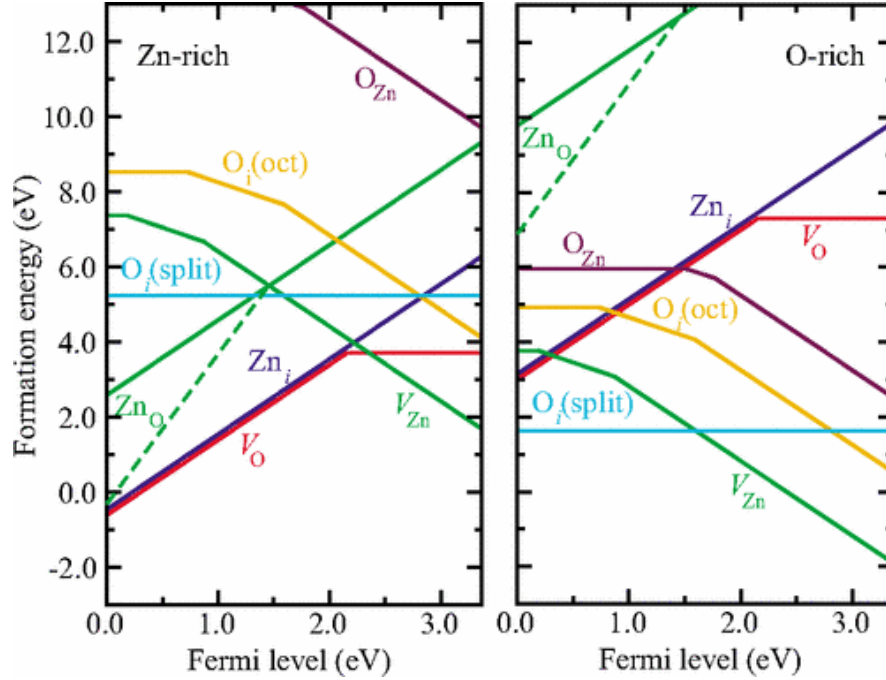
Figure 2.5: Calculated ZnO native point defect formation energies as a function of Fermi-level position in both Zn-rich (left) and O-rich (right) conditions. Valence band maximum is located at the zero of Fermi level. Different slopes represent different charge states.[35]

The thermodynamic transition levels for native point defects in ZnO are demonstrated in Figure 2.6. These thermodynamic transition levels relate to thermal ionization energies. A shallow level is the transition level to which the defect is thermally ionized at room temperature; by contrast, a deep level is the transition level that it is not ionized at room temperature. For shallow centres, they can happen in two cases. First, they happen when the transition level in the band gap is located near the band edges; valence-band maximum or conduction-band minimum. Another occurs when the transition level is a resonance in the conduction or valence band. Notably, some of transition levels $\varepsilon(q/q')$ cannot be observed in optical spectroscopy experiments.

Migration of native point defects in the crystal lattice is also important to study since it provides a key to understanding how point defects are incorporated during growth and processing as well as providing self-diffusion and impurity diffusion

models. These diffusions are often moderated by native defects. Equation 2.5 show the calculation of the activation energy for self-diffusion (Q) which is the summation of the formation energy of the defect that mediates the self-diffusion (E^f) and its migration energy barrier (E_b).[57]

$$Q = E^f + E_b \tag{2.5}$$
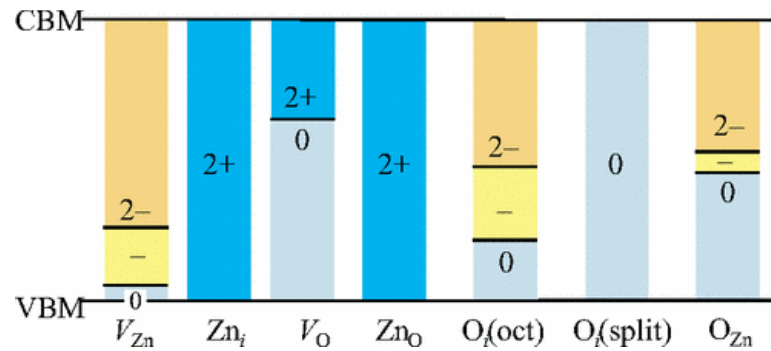
Figure 2.6: Thermodynamic transition levels for ZnO native point defects.[35]

2.2 Optical Properties and Processes in ZnO

Optical properties and processes in ZnO have been studied for several decades. Like other semiconductors, ZnO optical properties have their origin in both intrinsic and extrinsic effects. Intrinsic transitions occur between the electrons in the conduction band and the holes in the valence bands as well as between free and bound excitons while extrinsic transitions are introduced by dopants, impurities, point defects or complexes, generating electronic states in the band gap.

Luminescence is light emission from a material after external excitation through any process except blackbody radiation. The emission spectrum is related to intrinsic processes (without any defect and impurity) as well as extrinsic processes (with simple or complex defects and impurities). Consequently, the luminescence properties provide valuable information for studying defects and defect levels in materials. Both intrinsic and extrinsic processes can be investigated by numerous luminescence techniques. Different techniques have different types of excitation energy sources such as heat (thermoluminescence), voltage (electroluminescence), photons (photoluminescence), and electrons (cathodoluminescence).

Photoluminescence (PL) and Cathodoluminescence (CL) are the two main characterization tools for studying ZnO light emission processes. Photoluminescence spectroscopy is a powerful tool to characterize ZnO optical processes and is highly sensitive to point defects; therefore, it reveals characteristic radiative transition channels. The cathodoluminescence of ZnO has received great attention as the signal originates from a recombination of electrons and holes at defects and chemical impurities produced in the fabrication process. In addition, the ZnO cathodoluminescence is very sensitive to the surface state of the ZnO and impurities under low voltage excitation (1 – 5 kV).[58]

The characteristic emission spectra of ZnO consist of two major peaks which are near band edge (NBE) emission and deep level (DL) emission related to defects as shown in Figure 2.7. The NBE emission peak located at approximately 3.3 eV is dominated by free and bound exciton emission (FX and D^0X) along with LO phonon replicas. The DL emission band usually appears in the range of 1.7 eV to 2.4 eV depending on defect types or impurities.

2.2.1 Excitons

The exciton is formed by the electrostatic Coulomb attraction between a free excited electron and a hole. The attractive force between an electron and a hole is defined as the exciton binding energy (E_X). The exciton binding energy or ionization energy can be calculated by equation 2.6 utilizing a hydrogen-like model.[59]

$$E_X = \frac{m_r^* e^4}{2\hbar^2 \varepsilon^2 n^2} \tag{2.6}$$

where n is the quantum number (n = 1 corresponding to exciton at ground state), m_r^* is the reduced mass of the electron-hole pair, e is the elementary charge, $\hbar$ is the reduced Plank's constant, and ε is the dielectric constant.

ZnO has a large exciton binding energy of 60 meV; hence it has a significantly high percentage of excitons at room and higher temperatures. This also leads to the high emission efficiency of ZnO based devices.
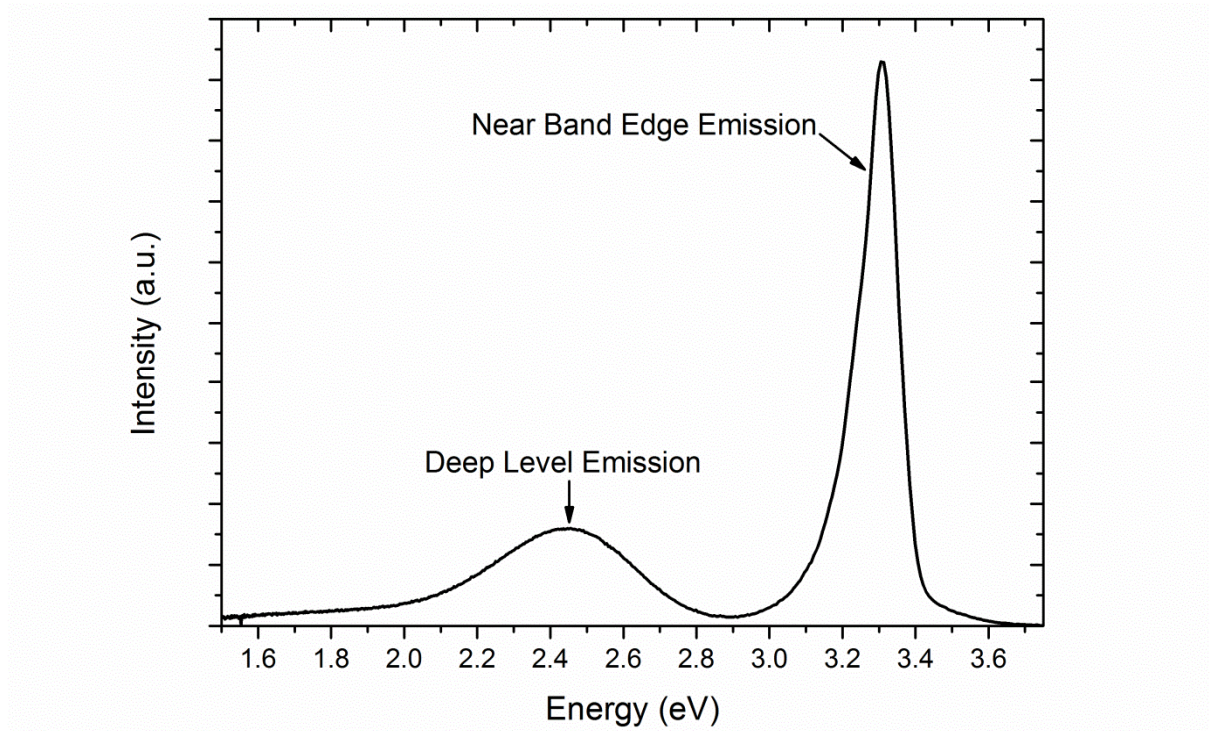
Figure 2.7: Characteristic ZnO luminescence spectrum presenting the near band edge peak (NBE) and the broad deep level emission (DL).

2.2.2 Radiative Recombination

After electrons are excited from the valence band, an electron-hole pair is generated (Figure 2.8a). An electron in the conduction band can then recombined with a hole in the valence band. In radiative recombination, the excess energy is emitted in the form of photon. The relative intensity depends on the concentration of a particular defect and its capture cross-section.[58] Due to self-absorption effects, ZnO radiative emission from excitons reaches the material surface when the recombination happens near the surface only. As shown in Figure 2.8, there are several possible radiative recombination mechanisms.

2.2.2.1 Near Band Edge Emission

In ZnO, Near Band Edge (NBE) emission is a radiation emitted in the UV region at approximately 3.3 eV. The most common recombination mechanism is band to band recombination in which the excited electron in the conduction band falls back to an empty free hole in the valence band (Figure 2.8b). Then it emits excess energy in the form of photon with an energy equal to the band gap energy (E_g). However, the

NBE emission in ZnO is dominated by free and bound exciton emission (FX, D^0X, A^0X) along with LO phonon replicas because of the very large and stable exciton binding enrgy of 60 meV. This leads to a decrease in the recombination energy gap ($E = E_g - E_X$) as presented in Figure 2.8c. The bound exciton recombination exhibits a variety of different sharp exciton lines, around 40 μeV in width, and usually observed at low temperature. At higher temperature, these peaks are broader and merge at room temperature. Their photon energies are characteristic for each defect with a narrow energy range between 3.348 and 3.374 eV. The sharp lines are labeled as I lines. Since there are 12 transitions, the lines are labeled from I_0 to I_{11} previously used by Renolds *et al.*[60] There is a number of the assignment of the I lines as shown in Table 2.2 but their assignment is still controversial.

In addition, the energy recombination gap can be more reduced by free to bound (Figure 2.8d and e), donor-acceptor pair (Figure 2.8f), and some point defects or transition metal impurity (Figure 2.8g).

2.2.2.2 Defect-Related Deep Level Emission

The point defects with deep levels in ZnO typically produce a broad luminescence band in the visible range located between 2.9 eV and 1.5 eV in the emission spectra. These deep level luminescence emissions are commonly observed as green, yellow as well as red luminescence. There are a number of assignments of the defect-related luminescence bands including native defects and impurities with point defects such as oxygen and zinc vacancies (V_O and V_{Zn}), zinc interstitial (Zn_i), substitutional lithium on zinc site (Li_{Zn}) and etc. For example, the GL band in ZnO was assigned as a transition from oxygen vacancy (V_O) to the valence band and the YL band at 1.96 eV is attributed to substitutional lithium on a zinc site (Li_{Zn}) in ZnO.[61] Although the defect-related bands have been assigned in articles, a conclusion on the emission origin is still under debate.
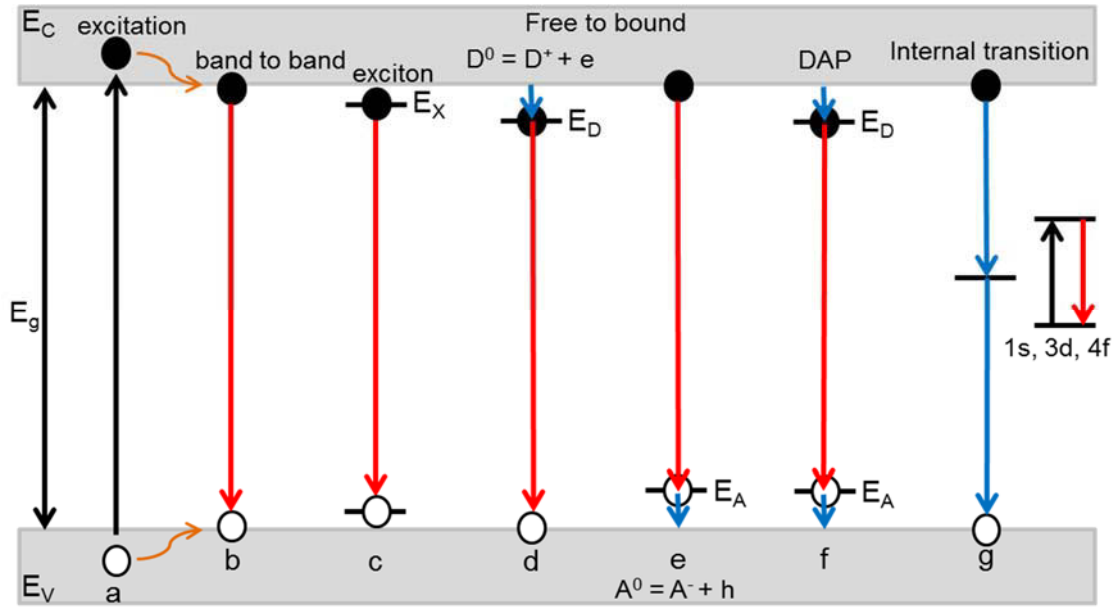
Figure 2.8: Schematic diagram of the radiative recombination mechanisms;

a Excitation

b Band to band $\qquad\qquad\qquad\qquad$ $E = E_g$

c Free and bound exciton $\qquad\qquad$ $E = E_g - E_X$ $\quad$ [FX, (D^0X), (A^0X)]

d Free hole to donor bound electron $\qquad$ $E = E_g - E_D$ $\qquad\qquad$ [D^0, h]

e Free electron to acceptor bound hole $\quad$ $E = E_g - E_A$ $\qquad\qquad$ [e ,A^0]

f Donor-acceptor pair $\qquad\qquad\qquad$ $E = E_g - E_D - E_A - \dfrac{q^2}{4\pi\varepsilon_o\varepsilon r}$ $\quad$ [D^0, A^0]

g internal excitation 1s levels point defects, 3d and 4f levels transition metals

where E_g is the bandgap of the material.

$\qquad$ E_X is the exciton bonding energy.

$\qquad$ E_D is the energy of the donor levels as measured from the bottom of the E_C.

$\qquad$ E_A is the energy of the acceptor levels as measured from the top of the E_V.

$\qquad$ $\dfrac{q^2}{4\pi\varepsilon_o\varepsilon r}$ is the Coulombic interaction between the electron and the hole.

Table 2.2: Bound exciton peak energies (eV) in ZnO

Line	Energy (eV)
I_0	3.3707^{62}, 3.3724^{63}, 3.3725^{53}, 3.3741^{62}, 3.3754^{62}, 3.3772^{62}
I_1	3.3679^{53}, $3.3702^{62,\,64}$, 3.3714^{63}, 3.3718^{53}, 3.3741^{62}, 3.3754^{62}
I_2	3.3662^{63}, 3.3670^{63}, 3.3674^{53}, 3.3686^{62}, 3.3693^{62}, 3.3707^{62}
I_3	3.3640^{65-66}, 3.3650^{62}, 3.3652^{63}, 3.3653^{66}, 3.3660^{53}, 3.3664^{62}, 3.3665^{53}, 3.3693^{66}
I_4	
I_5	3.3622^{66}, 3.3624^{63}, $3.3628^{53,\,65}$, 3.3632^{66}, 3.3634^{62-63}, 3.3643^{62}
I_6, I_7	3.3610^{63}, 3.3611^{65}, 3.3614^{53}, 3.3618^{62}, 3.3620^{64}
I_8	3.3600^{53}, 3.3602^{63}, 3.3604^{53}, 3.3605^{62}, 3.3606^{65}, 3.3608^{53}, 3.3610^{64}
I_9	3.3592^{66}, 3.3593^{53}, 3.3594^{63}, 3.3597^{66}, $3.3598^{53,\,62}$
I_{10}	3.3562^{63}, 3.3564^{62}, 3.3566^{65}, 3.3567^{53}, 3.3580^{64}
I_{11}	3.3530^{62}, 3.3531^{53}
	3.3481^{62}, 3.3484^{53}

2.2.2.2.1 Green Luminescence

The green luminescence in ZnO is emitted in the range of 2.4 to 2.6 eV. In earlier studies, the green luminescence was attributed to copper impurities.[54] However, later evidence suggests that the intrinsic defects oxygen and zinc vacancies are more favourable for the broad GL band. From the defect formation energy calculation of native point defects in ZnO, V_O appears to be the most favourable in zinc rich growth conditions whereas V_{Zn} is the most common in oxygen rich conditions.[33] Copper impurities give a fine structure GL band centred at 2.4 eV while native point defects (V_O and V_{Zn}) show a structureless band at the same energy with an equal peak width.

The fine structure GL band is mainly correlated with copper impurities. According to the Dingle study,[49] the broad GL band at approximately 2.45 eV with two sharp lines on zero-phonon line is related to a divalent copper ion Cu^{2+} in a ZnO zinc lattice site (Cu_{Zn}). The EPR results are closer to the EPR observation of Cu_{Zn} acceptor ground state in ZnO ($g_{//} = 0.7383 \pm 0.0003$, $g\perp = 1.5237 \pm 0.003$) studied by Dietz *et al*.[67]

The structureless GL band in ZnO was ascribed to native point defects and complex defects such as V_{Zn} acceptor,[33, 68] Zn_i,[69] O_{Zn},[70] and V_O[45, 71-74]. The GL band was explained by various types of electron transitions. Vanheusden et al.[72] explained GL by the transition of electron from V_O donor level near conduction band to the valence band (D–h-type recombination). Guo et al.[68] described it by a DAP transition in which electrons move from V_O or other donor levels to deep V_{Zn} acceptor levels. Kohan et al.[33] proposed that GL is the electron transition from the conduction band to the V_{Zn} acceptor (e–A type). In addition, GL was elucidated by a transition of an electron between two states of V_O (intracenter transition).[74] Leiter et al.[74] have shown in their model that the two-electron ground state of the neutral V_O is a diamagnetic singlet state.

2.2.2.2.2 Yellow Luminescence

ZnO also emits yellow luminescence centred at $2.0 - 2.2$ eV. According to PL studies of undoped ZnO, the YL has been attributed to excess oxygen in samples[75] and oxygen interstitials (O_i) occurring during hydrothermal processes.[76-78] The production of YL from the hydrothermally grown ZnO nanorods was also observed and systematically studied by PL.[79] It was also suggested that the PL yellow emission was due to the presence of OH groups or $Zn(OH)_2$ on the surface of ZnO nanorods rather than oxygen interstitials. Some studies also reveal that YL is also related to lithium impurities. It has been shown that the YL in hydrothermally grown ZnO could be related to deep Li_{Zn} acceptors.[55, 80] YL is believed to result from a donor-acceptor pair transition from a shallow donor to the Li_{Zn} acceptors.[81] Notably, adsorption of OH groups on the ZnO surface is favourable under hydrothermal treatments, and the chemical origin of YL produced by hydrothermally grown ZnO could be different from those obtained by other preparation methods.

2.2.2.2.3 Red Luminescence

The red luminescence in ZnO has a peak centred at $1.7 -1.9$ eV. The red and orange-red emissions were previously assigned as originating from oxygen interstitials (O_i),[80, 82] zinc vacancies (V_{Zn}),[83] and substitutional nitrogen defects on oxygen sites.[84] The RL in ZnO is also frequently related to excess zinc since it appears after annealing ZnO in zinc rich atmosphere.[85-86] Annealing ZnO in zinc vapour with hydrogen in the environment leads to the RL generation as well. This process is able to

be reversed by removing hydrogen; therefore, the RL may be associated with the interaction between oxygen vacancies and hydrogen.[87] In the most recent work, Chen *et al*. have studied the nature of RL in ZnO single crystals. They proposed that the RL is related to the optical transition between a shallow donor and Zn_i-V_O complex or $V_{Zn}V_O$ di-vacancies defect centres.[88]

2.2.3 Temperature-Dependence Luminescence

In order to understand the physical processes of optical materials like ZnO in depth, temperature dependence measurements are utilized. These allow us to recognize the interaction of energy levels with phonons. The levels over the interaction provide information of energy shifts,[89] broadening,[90] and energy levels dissociation.[53] From low temperature to room temperature, the spectroscopic features overlap into one due to the broadening and energy shift. At low temperature, the separation of peaks reveals the dominant processes.

The temperature dependence measurement is a very interesting method for the free excitons temperature dependence investigation; however, there is still limited knowledge about the temperature dependence of ZnO spectral reflectivity properties.[91] One difficulty is precise determination of the ZnO electronic structure at room temperature since the features broaden and overlap into one broad peak at temperatures above 150K. The temperature intervals have to be small enough between each scan in order to see the effect of the increase in phonon interaction on energy levels. The spectroscopic feature gradually changes in both energy and intensity when the temperature changes. Additionally, the intensity of fine structure resulting from energy levels with tiny localization or binding energies significantly decreases at the temperature equals to its dissociation energy.

2.3 Electrical Properties of ZnO

ZnO is undoubtedly attractive for a variety of electronic and optoelectronic applications at room temperature owing to its direct and large bandgap as well as high exciton binding energy (60 meV at 300K). The large bandgap leads to numerous advantages such as high temperature and power operation, lower noise generation,

higher breakdown voltages as well as large electric fields sustainability.[92]   However, electrical properties of ZnO are difficult to measure since there is wide range of sample qualities.

The electron effective mass and the hole effective mass are 0.24 m_0 and 0.59 m_0, respectively. For a low *n*-type conductivity, the corresponding electron Hall mobility at 300K is μ = 200 $cm^2/V\bullet s$ while μ = 5-50 $cm^2/V\bullet s$ for a low *p*-type conductivity. [93] Due to the relatively high electron mobility, ZnO overpowers other wide bandgap materials for photo-electro-chemical applications.

The point defects also have a substantial effect on the conductivity of ZnO. According to Van de Walle's results, hydrogen is a dominant background donor in ZnO since it is effortlessly ionized with quite low formation energy.[94] Furthermore, other results confirmed that hydrogen shallow donors in ZnO play a significant role in the conductivity of ZnO.[95-97] On the other hand, V_O and Zn_i are deep donors with high ionization energy leading to difficult free electrons production.[33] Consequently, they do not make a significant contribution to conductivity of ZnO. In addition, Zn_i has a limited ability to contribute to *n*-type conductivity because of its high formation energy although some theoretical studies suggested that it is a shallow donor.[98-99] However, the Zn_i complexes (Zn_i-N_O) play a considerably role in ZnO conduction.[100]

In order to study the electrical properties of ZnO, two electrodes are needed. Therefore, ohmic and schottky contacts to ZnO must be considered.

2.3.1 Ohmic Contacts to ZnO

The ohmic contact is a low resistance junction carrying electrical current from metal to semiconductor as well as in the opposite direction. The current-voltage relationship is a linear and symmetric in both positive and negative voltages with a fast response for a small voltage and no parasitic resistance. The parasitic resistance is one of the main problems for long-lifetime optical and electrical devices operations. Moreover, the high-resistance metal-semiconductor ohmic contacts resulting from thermal stress and poor contact reduce the device performance.

To achieve a high performance of ZnO-based optical and electrical devices, ohmic contacts need to be thermally stable and reliable as well as low in resistance. There are two methods to attain this high performance: first, decrease the metal

semiconductor barrier height by carrying out surface preparation leading to an increase in carrier tunnelling probability; the other is enhancing the effective carrier concentration near the surface.[101-103]

2.3.2 Schottky Contacts to ZnO

A Schottky contact is a metal-semiconductor contact having a large barrier height. In addition, it has low doping concentration which is less than the density of states in the conduction band or valence band. There are numerous difficulties in the formation of Schottky contacts; for example, the chemical reactions between the metal and the semiconductor, the surface states, the contaminants, the surface layer defects as well as the metal diffusion into the semiconductor.[94]

For ZnO device applications, high quality Schottky contacts are required. It is still a challenge to understand and control ZnO Schottky barriers according to the wide and variable range of barrier heights from the same metal on a ZnO surface.[104] Additionally, ZnO barrier heights are strongly affected by extrinsic factors *i.e.* the quality of crystal and surface treatment.[104] However, a high work function can be applied to a ZnO crystal surface so that a useful ZnO Schottky barrier is created.

2.4 Gas Sensing Properties of ZnO

ZnO is one of the most interesting semiconducting metal oxides for the high performance gas sensors utilized in the ppm-sensitivity range. Moreover, one-dimensional (1D) ZnO nanostructures provide higher gas sensing performance according to their high surface area to volume ratio.[105-107] They can detect various kinds of gases including both reductive gases and oxidative gases such as H_2,[108-111] NH_3,[112-114] H_2S,[115-116] CO,[117-118] C_2H_5OH,[119] H_2O,[120-121] O_2,[122] O_3,[111, 123] and NO_2.[124-125] The detection of gas molecules can be attained by measuring the change in resistivity or conductivity with the reversible chemisorption process of reactive gases on the ZnO surface.[94, 111] However, high sensitivity and selectivity as well as low operating temperature are still a big challenge in making commercial ZnO gas sensors.[7, 126]

2.4.1 Gas Sensor Characteristics

The measured principal parameter of the semiconducting oxide sensors is resistance (R) or conductance (I, $\frac{1}{R}$). All sensor operating characteristics are resulting from this simple measurement. Resistance or conductance is a simple and easily measured parameter but it is a second-order parameter. Hence, the elementary steps of the sensing processes are still undeveloped.

The fundamental characteristics of gas sensor performance are the sensitivity, selectivity, and the sensing response reversibility. These three characteristics are measurable parameters.

2.4.1.1 Sensitivity

The sensitivity is one of the key characteristics of gas sensor revealing the lowest analyte gas concentration that gas sensor can detect. To consider the donor gases adsorption on *n*-type semiconducting oxides, sensitivity is the easiest parameter to study. At equilibrium states in a gas sensor, the sensitivity of sensor is the ratio of the change in signal amplitude to the original signal. Since the resistance or current of sensors is recorded, the sensitivity can be calculated by equation 2.7 for *n*-type semiconductor.

$$S = \frac{R_a}{R_g} = \frac{I_g}{I_a} \tag{2.7}$$

where S is a sensitivity of gas sensor at a particular concentration of gas, R_a and I_a are the resistance and current of the sensor when exposed to air (baseline resistance and current), where R_g and I_g are the resistance and current when exposed to the analyte gas. I_a and I_g are shown in Figure 2.9. A high value of S is high in sensitivity.

2.4.1.2 Selectivity

Selectivity demonstrates how well sensor recognizes one gas amongst others. In general, one semiconducting gas sensor can detect more than one gas; therefore, it exhibits poor selectivity. Under the same operating conditions, analyte gas is always desired to provide higher sensitivity than other interfering gases. With the coexistence of interfering gases in the atmosphere, the selectivity of the sensor can be described by equation 2.8.

$$Selectivity = \frac{Sensitivity\ of\ interfering\ gas}{Sensitivity\ of\ analyte\ gas} \tag{2.8}$$

Similar to other semiconducting gas sensors, pure ZnO also has poor selectivity. ZnO exhibits the same responses to various types of reductive gases and organic vapour. Nonetheless, the ZnO sensor with certain functional groups affecting the adsorption processes can overcome this problem.[127-128]

2.4.1.3 Response Time and Recovery Time

Response time and recovery time are significant parameters displaying how fast gas sensors are able to respond to analyte gases and how fast they recover. Response time is the time required by sensor to reach 90% of the saturation value of resistance or current when exposed to an analyte gas. Recovery time is the time required by the sensor to achieve 90% of its original signal state after changing back to exposure to clean air.

To be a good sensor, both response time and recovery time need to be small. ZnO nanorods gas sensors exhibit a long response time as well as long recovery time as shown in Figure 2.9.
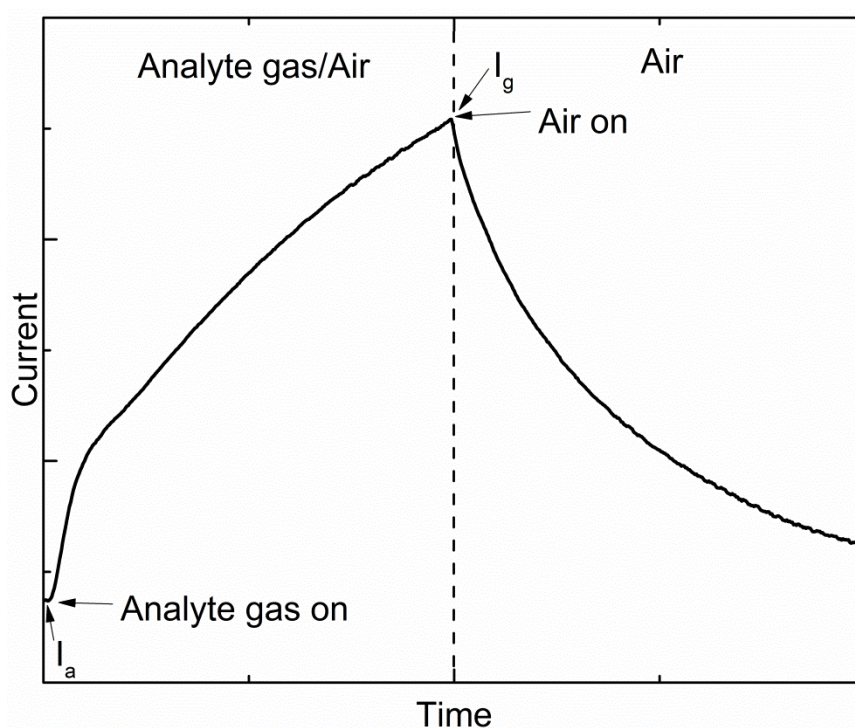
Figure 2.9: Characteristic current-time sensing peak of ZnO nanorods annealed in O_2 atmosphere response to ammonia gas.

2.4.2 Gas Sensing Mechanisms of ZnO

The gas sensing mechanism is a change of sensor's properties when the environment changes, allowing the monitoring of the varying properties of the sensor. The interaction of the sensor surface with the analyte gas can be explained by two key functions; receptor and transducer functions. The receptor function is an electronic change of the oxide surface through a gas-solid interaction with a target gas while the transducer function is an electrical resistance change of the sensor through a surface phenomenon. According to receptor and transducer functions, the various electronic states are created by the interaction of the sensor surface with the analyte gas. The electronic properties of oxide semiconductors are modified in both the oxidative and reductive gases but in the opposite direction for *n*-type semiconductor and *p*-type semiconductors. The charge carriers are electrons and holes in an *n*-type semiconductor and *p*-type semiconductor, respectively. Consequently, the electron concentration is low in the for *n*-type semiconductor leading to an increase in the resistance whereas the resistance decreases in air for *p*-type semiconductor.

In this study, we mainly focus on *n*-type ZnO. First, consider the adsorption and desorption phenomena on the ZnO surface exposed to normal air atmosphere. Since oxygen is one of the most active components in the air, surface reactions in ZnO always involve adsorbed oxygen species (O_s^{-n} where n and s = 1 or 2). The oxygen gas molecules can bind to the ZnO surface through both physisorption and chemisorption processes depending upon the temperature. The following reactions represent the oxygen adsorption processes in different temperature,[14, 111, 129-130]

At low temperature:

$$O_{2(gas)} \leftrightarrow O_{2(ads)} \tag{2.9}$$

$$O_{2(gas\ or\ ads)} \leftrightarrow O_{2(ads)}^{-} \quad (\text{at T} < 150\,°C) \tag{2.10}$$

At high temperature:

$$O_{2(gas)} + 2e^{-} \leftrightarrow 2O_{(ads)}^{-} \quad (\text{at } 150\,°C < T < 250\,°C) \tag{2.11}$$

$$O_{2(ads)}^{-} + e^{-} \leftrightarrow 2O_{(ads)}^{-} \quad (\text{at } 150\,°C < T < 450\,°C) \tag{2.12}$$

$$O_{2(gas)} + 4e^{-} \leftrightarrow 2O_{(ads)}^{2-} \quad (\text{at T} > 250\,°C) \tag{2.13}$$

$$2O_{(ads)}^{-} + e^{-} \leftrightarrow O_{(ads)}^{2-} \quad (\text{at T} > 450\,°C) \tag{2.14}$$
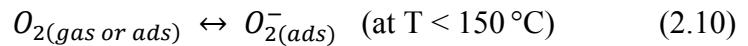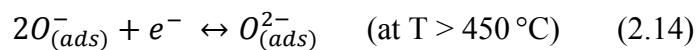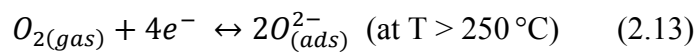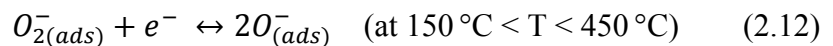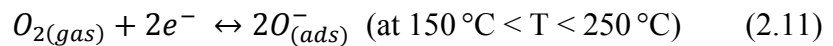
where (gas) are free gases, (ads) are species adsorbed on the ZnO surface and e^- are electrons contributed by ZnO.

When oxygen gas molecules adsorb onto ZnO surface, they trap electrons from the ZnO conduction band leading to an increase in resistance (a decrease in conductivity). Meanwhile, the depletion layer (space-charge layer) is formed as shown in Figure 2.10. The depletion layer is a deficient carriers region because of the electron trapping by adsorbed oxygen species. The general depletion thickness (space-charge thickness or Debye length) is approximately 30 nm for undoped ZnO.[131]

After the depletion layer is formed, ZnO gas sensor is subsequently exposed to an analyte gas which can be either oxidative or reductive. The response to oxidative or reductive gases can be detected by measuring the resistance or conductivity of ZnO gas sensing materials. Oxidative and reductive gases provide different contributions.
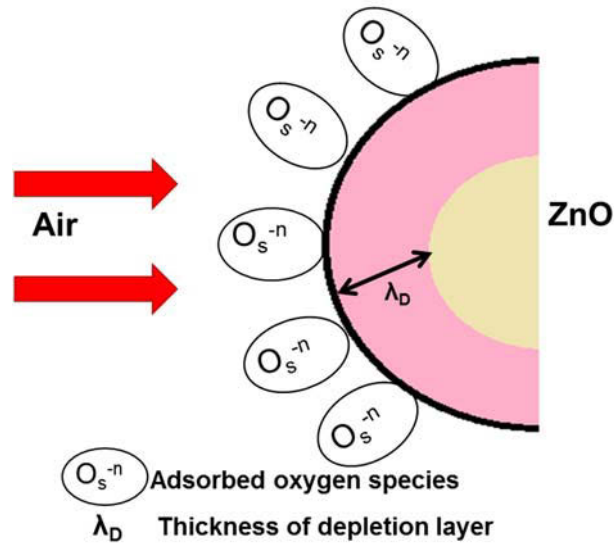
Figure 2.10: Schematic diagram of oxygen adsorption on the ZnO surface; n = 1 or 2 and s = 1or 2. (Adapted from Kim *et al.*)[111]

2.4.2.1 Oxidative Gas

The oxidative gases; for example, O_2,[122] O_3,[111, 123] and NO_2,[124-125] can be detected by ZnO. After the adsorption of adsorbed oxygen species (O_s^{-n}) on the ZnO surface, the oxidative gas molecules react with them and remove more electrons from the conduction band, resulting in thicker depletion layer as shown in Figure 2.11. The thicker depletion layer is due to the lower carrier concentration. This result also leads to a reduced conductivity.

2.4.2.2 Reductive Gas

ZnO can also detect reductive gases such as H_2,[108-111] NH_3,[112-114] H_2S,[115-116] CO,[117-118] C_2H_5OH,[119] and H_2O[120-121] but the mechanism is opposite to that of the oxidative gases. Moreover, it provides relatively high sensitivity. These gases react with surface adsorbed oxygen (O_s^{-n}) and subsequently remove it and release electrons back to the ZnO conduction band, leading to a decrease of the depletion layer thickness as shown in Figure 2.12. In addition, it leads to an increase of conductivity.
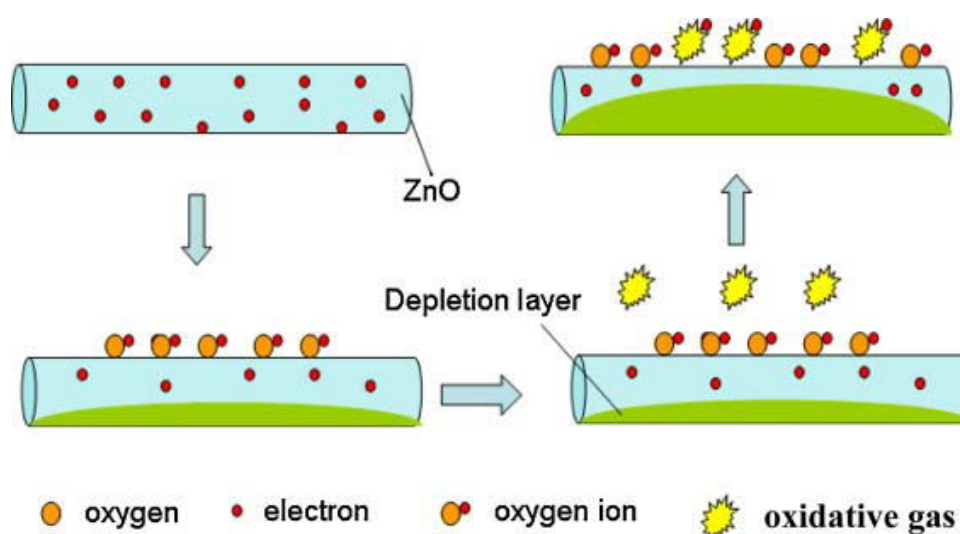
Figure 2.11: Schematic diagram of the oxidative gas sensing mechanism on ZnO surface.[107] (Green area is the depletion layer.)
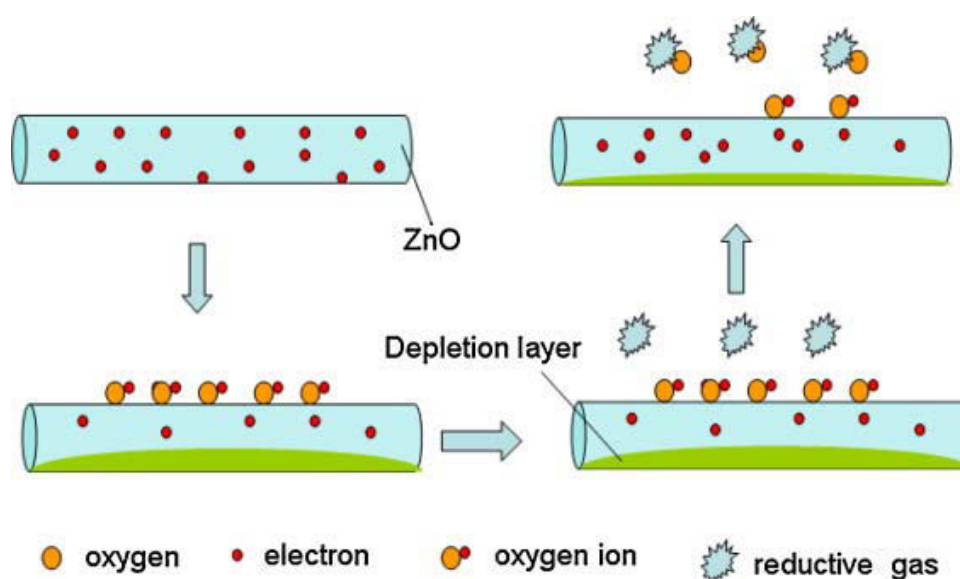
Figure 2.12: Schematic diagram of the reductive gas sensing mechanism on ZnO surface.[107] (Green area is the depletion layer.)

2.4.2.2.1 Ammonia Gas

In this work, ammonia (NH_3) gas was employed as a model reductive gas. Possible surface reactions related to the NH_3 gas response sensitivity of sensors fabricated by the ZnO are given as follows.

$$NH_{3(gas)} + 3O_{2(ads)}^{-} \leftrightarrow 6H_2O_{(gas)} + 2N_{2(gas)} + 3e^{-} \quad \text{(at T} < 150\,°C) \quad (2.15)$$
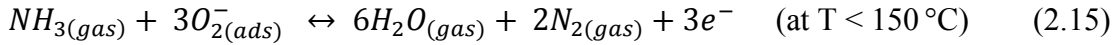
Figure 2.13 shows how NH_3 gas reacts with adsorbed oxygen species on ZnO surface.
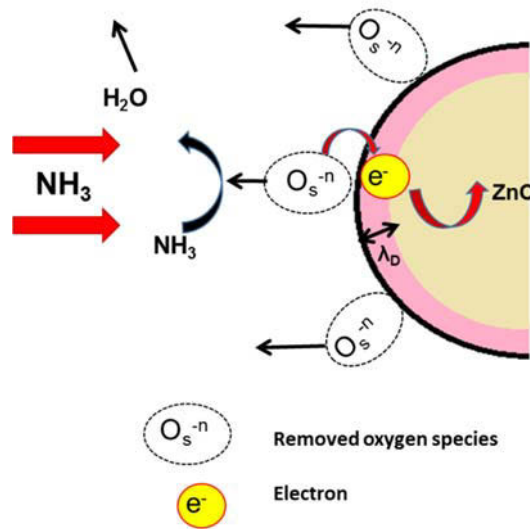
Figure 2.13: Schematic diagram of ammonia gas sensing mechanism on the ZnO surface; n = 1 or 2 and s = 1or 2.

2.5 Synthesis of ZnO Nanostructures

Several methods have been developed over the previous decade to prepare nanomaterials with unique structural and physical properties; for example, template-assisted, vapour-liquid-solid (VLS), colloidal micelle and electrochemical processes.[1] The high-temperature vapor-phase approaches; physical vapor deposition [132-133] as well as chemical vapor deposition, [134-135] have been widely utilized for controlled aligned ZnO nanoarray growth. However, these approaches are typically expensive and energy-consuming. Fortunately, there are various low temperature solution-phase approaches; such as aqueous chemical growth (ACG) and hydrothermal growth (HTG). These methods have been developed to fabricate controllable ZnO nanostructures on substrates

in recent decades due to their potential for scale-up of production, commercial feasibility and low energy-consumption.[133]

Growth of well-controlled ZnO nanostructures can be carried out by a variety of methods, including both high-temperature and low-temperature approaches.

2.5.1 High Temperature Approaches

The high temperature synthesis of ZnO nanostructures is typically carried out at temperatures in the range of 500°C to 1500°C. It is usually a gas phase synthesis performed under gaseous environment in closed chambers. There are several common gas phase methods; for instance, vapour phase transport, including vapour solid (VS) and vapour liquid solid (VLS) growth,[136-139] physical vapour deposition,[140] chemical vapour deposition,[141] metal organic chemical vapour deposition (MOCVD),[142] thermal oxidation of pure Zn and condensation,[143] and microwave assisted thermal decomposition.[144] These methods can control the formation of ZnO nanostructures in designed patterns; however, they require complicated equipment and consume high energy.

2.5.2 Low Temperature Approaches

The low temperature approaches for ZnO nanostructures growth are generally carried out in the solution phase. The growth of ZnO in the solution phase synthesis occurs in liquid phase. The processes are regularly carried out in an aqueous solution which is called hydrothermal growth. Other examples of the ZnO nanostructures solution phase synthesis are Zinc Acetate Hydrate derived nano-colloidal sol-gel route,[145] Zinc Acetate Hydrate in alcoholic solutions with sodium hydroxide or tetra methyl ammonium hydroxide,[146-148] template assisted growth,[149] spray pyrolysis for growth of thin films,[150-151] and electrophoresis.[152]

2.5.2.1 Hydrothermal Growth

In this study, hydrothermal growth (HTG) is employed owing to its controllable ZnO nanostructures on various substrates, potential for scale-up production, commercial feasibility and low energy-consumption.

In basic wet chemical methods, the crystallization of ZnO happens via the hydrolysis of Zn salts in a basic solution. The ZnO nanostructures

formation needs an alkaline solution since divalent metal ions do not hydrolyse in acidic solutions. Both KOH and NaOH are the most common alkali compound utilized in the formation of ZnO nanostructures. For hydrothermal synthesis of ZnO nanostructures, Zinc nitrate [$Zn(NO_3)_2$] and hexamethylenetetramine ($C_6H_{12}N_4$) are generally used. Zn^{2+} ions are produced by $Zn(NO_3)_2$. HMT is believed to act as a weak base but the exact function of HMT during the growth is still unclear. It should slowly hydrolyze in the water solution and gradually produce OH^-.
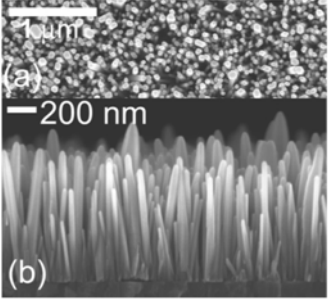
The following is the possible formation process of ZnO nanostructures by $Zn(NO_3)_2$ and HMT:[153]

$$C_6H_{12}N_4 + 6H_2O \leftrightarrow 4NH_3 + 6HCHO \qquad (2.16)$$

$$H_2O + NH_3 \leftrightarrow OH^- + NH_4^+ \qquad (2.17)$$

$$Zn^{2+} + 4NH_3 \leftrightarrow [Zn(NH_3)_4]^{2+} \qquad (2.18)$$

$$Zn^{2+} + 2OH^- \leftrightarrow Zn(OH)_2 \quad \text{or} \quad Zn(NH_3)_4^{2+} + 2OH^- \leftrightarrow Zn(OH)_2(NH_3)_4 \quad (2.19)$$

$$Zn(OH)_2 / Zn(OH)_2(NH_3)_4 \rightarrow ZnO + H_2O \qquad (2.20)$$
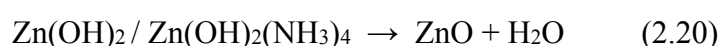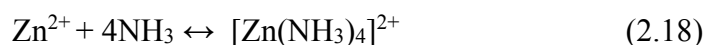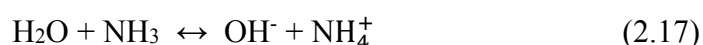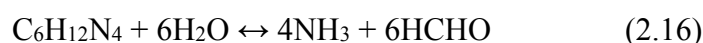
All of the five reactions can be controlled by adjusting the reaction parameters; precursor concentration, growth temperature and growth time.

The following table (Table 2.3) represents a summary of some hydrothermal growth and the resulting morphology of the synthesis of ZnO nanostructures.

Table 2.3: Summary of hydrothermal growth of ZnO nanostructures and their morphology

Synthesis conditions	Resulting morphology
• Deposition of ZnO seed layer on substrate. • Growing ZnO nanosturcture in seed solution (equimolar of $Zn(NO_3)_2.6H_2O$ and HMT, $C_6H_{12}N_4$) at different temperature, time and pH in sealable container.	 Representative SEM image of the ZnO nanorods: (a) top view and (b) side view.[154]
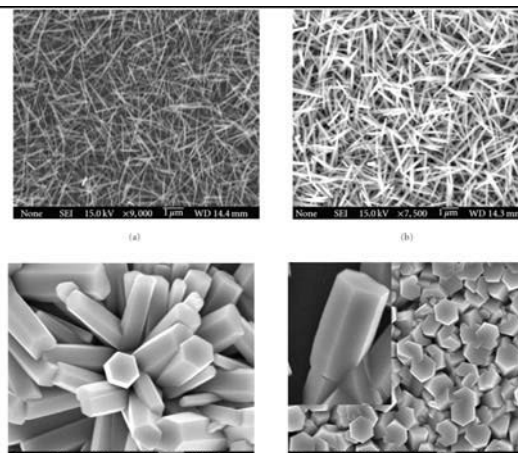
SEM images of ZnO NSs on Si substrate with different precursor concentrations of the growth aqueous solution (a) at 25mM; (b)50 mM; (c) 100 mM; (d) 300 mM. Inset shows the magnified view of the ZnO NSs (scale bar = 100 nm).[155]
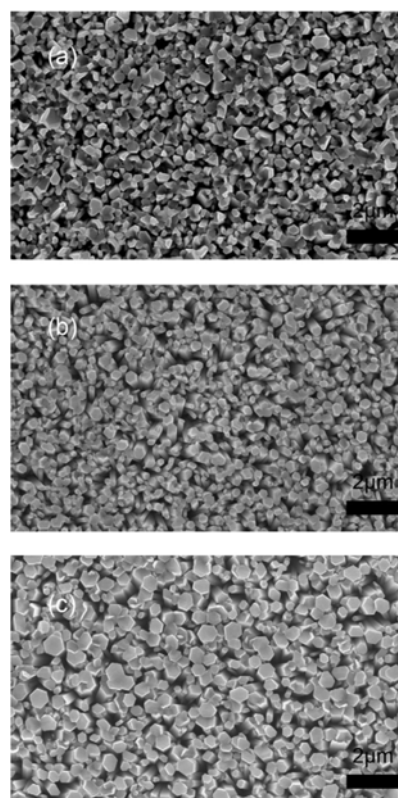
SEM images of ZnO nanorods grown on Si substrates with different ZnO seed layers: (a) plane view of ZnO nanorod arrays grown on ZnO-A seed layer; (b) plane view of ZnO nanorod arrays grown on ZnO-B seed layer; and (c) plane view of ZnO nanorod arrays grown on ZnO-C seed layer.[156]

CHAPTER III
CHEMICALS AND EXPERIMENTAL DETAILS

In this chapter, the synthesis of ZnO nanorods and post growth processes are described. The experimental techniques utilized in this research to characterize morphology, crystal structure, optical, electrical, and gas sensing properties of ZnO nanorods will also be outlined.

3.1 Chemicals and Instruments

Chemicals utilized in this research are shown in Table 3.1. All chemicals are analytical reagent grade and used as received without further purification. MilliQ water and ethanol were used as the solvent in all the experiments.

Table 3.1: List of Chemicals

Chemicals	Supplier
Zinc nitrate hexahydrate, 98%, $Zn(NO_3)_2 \cdot 6H_2O$	SIGMA-ALDRICH
Zinc acetate dihydrate, 98+%, $(C_2H_3O_2)_2Zn \cdot 2H_2O$	SIGMA-ALDRICH
Hexamethylenetetramine, HMT, $\geq$99.0%, $C_6H_{12}N_4$	SIGMA-ALDRICH

The synthesized ZnO samples were subsequently modified and characterized by various techniques to study general, optical, electrical, and gas sensing properties. Details of instruments used in this research are shown in Table 3.2.

3.2 Sample preparation

ZnO nanorods samples were prepared in two main steps. First, ZnO nanostructures were synthesized via a hydrothermal method. Then the synthesized ZnO samples were modified by post growth processing; annealing and plasma treatment.

Table 3.2: List of Instruments

Instruments	Model	Location
Field Emission Scanning Electron Microscope (FESEM)	Zeiss Supra 55VP SEM	MAU, UTS
X-Ray Diffraction (XRD)	Siemens D5000	MAU, UTS
Environmental Scanning Electron Microscope (ESEM) with Cathodoluminescence System	FEI Quanta 200 ESEM with Gatan MONOCL3	MAU, UTS
Photoluminescence Spectroscopy (PL)	HeCd laser with Spex-1404 double monochromator	TU Berlin
ELECTROMETER/HIGH RESISTANCE METER	Model 6157A, Keithley	Physics, MU
Gas Measurement System	Homebuilt	Physics, MU
Photoemission Yield Spectroscopy (PYS)	Homebuilt	MAU, UTS

Note: MAU is Microstructural Analysis Unit, UTS is University of Technology Sydney, TU Berlin is Technical University of Berlin and MU is Mahidol University.

3.2.1 ZnO nanostructures growth

In this work, silicon and sapphire wafers were chosen as the substrates. The pieces of substrates were cleaned by a standard cleaning process:

- 15 minutes ultrasonic bath in ethanol
- 15 minutes ultrasonic bath in isopropanol
- 15 minutes ultrasonic bath in MilliQ water
- Dried in air at room temperature

Subsequently, the cleaned substrates were deposited with a ZnO seed layer and followed by ZnO growth.

3.2.1.1 Seed layer deposition

The cleaned substrates were coated with a seed layer, as in the following steps:

- Dropped Zinc acetate solution (5mM in ethanol) on the substrate until it fully covered the surface
- Rinsed it with ethanol after 10 seconds
- Dried in air at room temperature

These steps were repeated 5 times to obtain complete coverage.

- Put the seed layer coated substrate into the oven at $250^{\circ}C$ for 20 minutes

All seed layer coating steps were repeated twice.

3.2.1.2 Hydrothermal growth

After the deposition of a seed layer, ZnO nanostructures were grown by a low temperature approach; hydrothermal growth (HTG). The pre-coated substrate was suspended in a seed solution containing 0.025M zinc nitrate hexahydrate and 0.025M hexamethylenetetramine at 90°C for 3 hours.[157-158]
The following shows the HTG steps:

- Put the pre-coated substrate in the seed solution in the Teflon lined autoclave

Figure 3.1 shows the photograph of Teflon lined autoclave.

- Seal and put the autoclave into the oven at 90°C for 3 hours

After the growth

- Cool Teflon lined autoclave naturally
- Take out and wash the resulting samples with MilliQ water to eliminate residual salts or amino complex D
- Dry in air at room temperature

Figure 3.1: Photograph of Teflon Lined Autoclave used as a reactor in hydrothermal growth.

3.2.2 Post growth processing

In order to modify the surface defect structure of ZnO, the resulting samples have been annealed in both oxidative and reductive environments after the growth. Some of samples were then treated in hydrogen plasma.

3.2.2.1 Annealing

The resulting samples have been annealed at annealing temperatures of 650°C in different gases; Inert gas (Ar), Oxidative gas (O_2) and Reductive gas (5%H_2 in Ar and zinc vapor) at approximately 2 Torr pressure and

100sccm flow rate for 30 minutes. All samples were annealed in the Lindberg Blue Mini-mite Tube Furnace (Figure 3.2). The maximum annealing temperature of the furnace is 1100°C. Annealing process can be done under vacuum or controlled gaseous environments.

Figure 3.2: Photograph of Lindberg Blue Mini-mite Tube Furnace.

3.2.2.2 Hydrogen Plasma Treatment

Hydrogen plasma treatment was accomplished utilizing mild hydrogen radio-frequency plasma for 20 minutes. Typically, hydrogen can be incorporated in ZnO in the temperature range of 25°C to 450°C. The hydrogen incorporation is as fast as 10 seconds. The energetic hydrogen radicals were ionised from hydrogen gas. Subsequently, they penetrated into the sample and diffused in. In this work, hydrogen radicals were generated by Radio Frequency power of 10W with 10 sccm H_2 flow rate. An AG 0202-HV OS high voltage plasma generator from T&C Power Conversion, Inc. was used to produce plasma. An Apex mass flow controller was used to flow hydrogen gas into the evacuated chamber and pressure was examined by Lam research series capacitance diaphragm gauge. ZnO samples were also heated at 100°C during plasma cycle to activate hydrogen diffusion. The samples were then naturally cooled in a hydrogen atmosphere chamber after plasma treatments. The overall setup of plasma chamber is demonstrated in Figure 3.3.
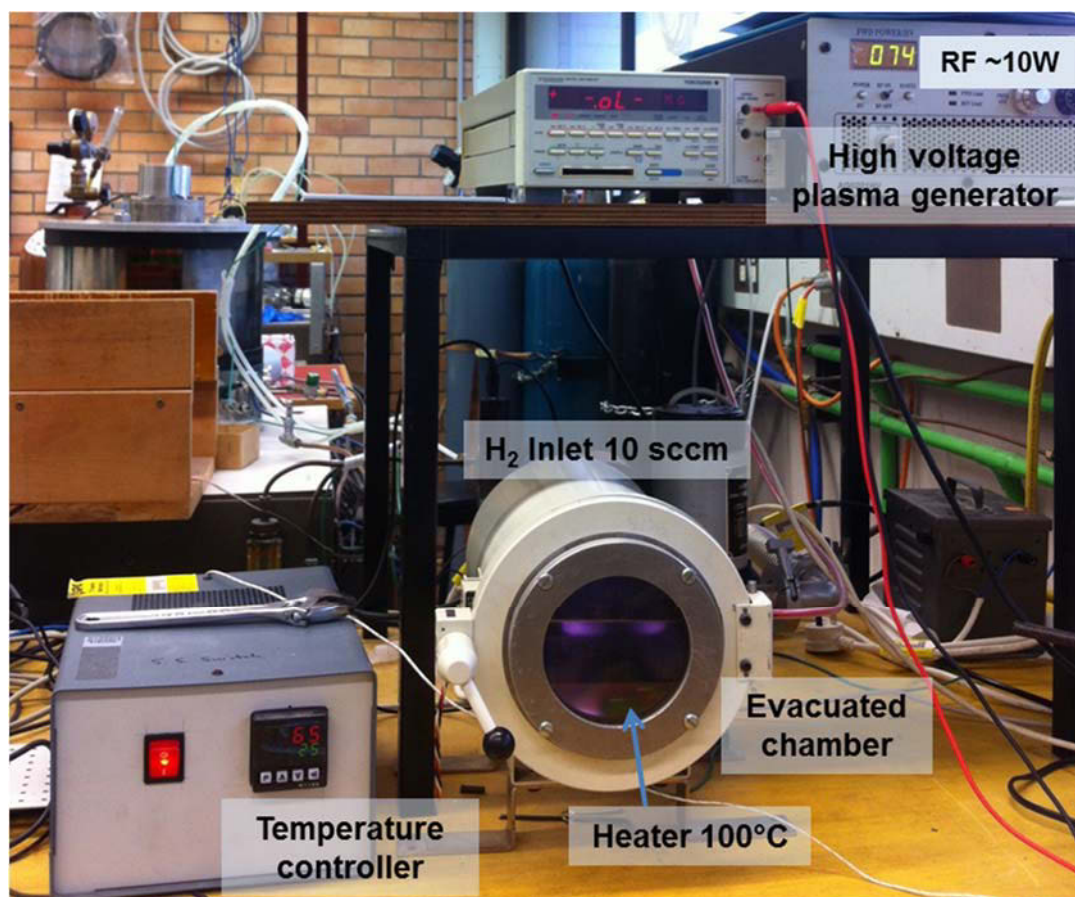
Figure 3.3: Photograph of plasma chamber showing the overall setup.

3.3 Scanning Electron Microscopy (SEM)

The morphology and the average diameter of the ZnO nanorods were investigated at 20 kV using a Zeiss Supra 55VP SEM. The Zeiss Supra 55VP SEM is a high resolution "Field Emission Scanning Electron Microscopes" (FESEM). The spatial resolution of the microscope is 1.0 nm, 1.7 nm, 3.5 nm, 4.0 nm, and 2.0 nm at 15 kV, 1 kV, 0.2kV, 1kV, and 30 kV (VP mode), respectively. Its high efficiency in-lens detector produces exceptional quality scanning electron images down to 0.1 kV. The samples were attached onto the specimen holders using carbon conductive tape.

During SEM examination, high energetic electrons from the incident electron beam interact with the sample and generate two types of electrons; secondary electron and backscattered electrons, as well as X-rays and light (Figure 3.4). Each emission is used for difference purposes. Low energy secondary electrons are ejected

during inelastic scattering of the primary electron beam providing topology information of the sample surface while high energy backscattered electrons bounce out of the sample after beam collides with sample nucleus giving the composition information. X-rays and light assign element concentration and defect information, respectively.
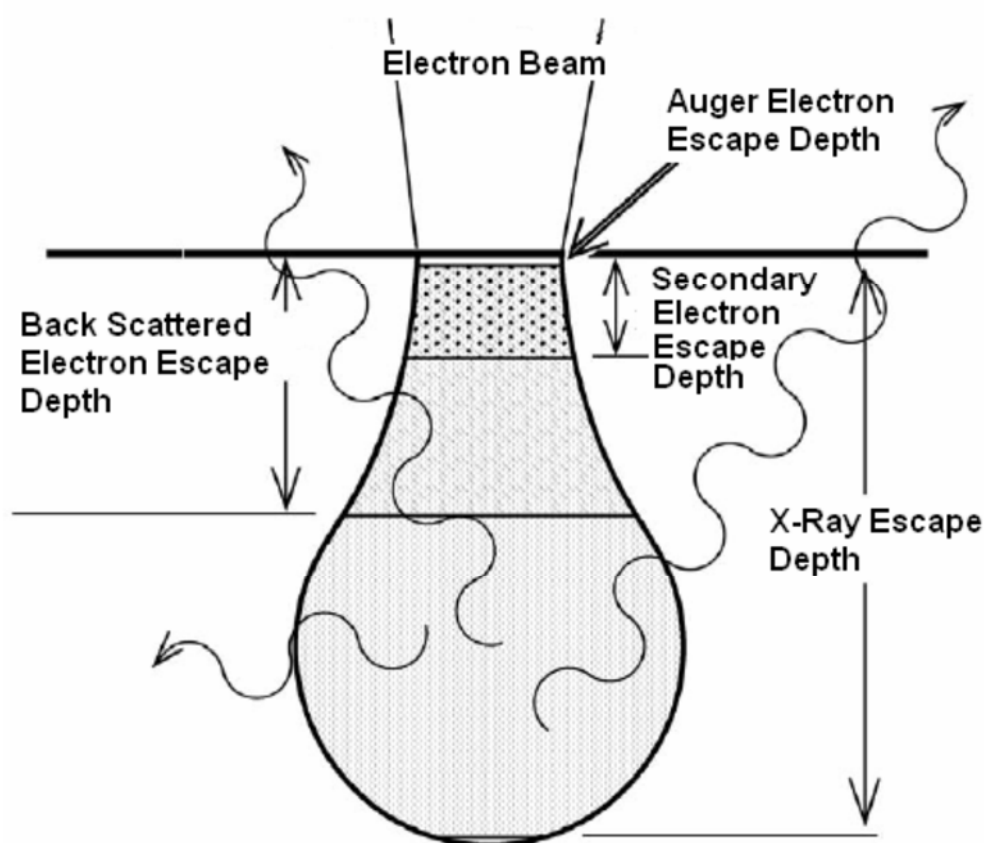
Figure 3.4: Penetration range of the primary electron beam with the origin of electrons, x-rays and light.[159]

3.4 X-Ray Diffraction (XRD)

Crystal structure and lattice parameters of the ZnO nanorods before and after annealing were characterized by a Siemens D5000 X-ray Diffractometer with Cu-K$_\alpha$ radiation and a wavelength of 1.5418Å. X-ray diffraction was performed in θ -2θ scanning mode in the range of 30°-65°. The crystalline phase and lattice constants were calculated by ICSD using POWD-12++.

In typical XRD, an incident beam of X-rays interacts with sample generating constructive interference from lattice planes when conditions satisfy Bragg's Law only (Equation 3.1). Bragg's Law reveals the relationship between electromagnetic radiation wavelength (λ), diffraction angle (θ) and lattice spacing (d) in samples.

$$n\lambda = 2d \cdot \sin\theta \qquad\qquad (3.1)$$

3.5 Cathodoluminescence Spectroscopy (CL)

Cathodoluminescence is an emission of light from a material during irradiation by an energetic beam of electrons. An emission of cathodoluminescence light is generated via electron-hole pair formation mechanism. A characteristic luminescence is emitted from the crystal under electron beam irradiation where the relative intensity depends on the concentration of a particular defect and its capture cross-section.[58] In addition, the ZnO cathodoluminescence is very sensitive to the surface state of the ZnO crystal and impurities under low voltage excitation (1 − 5 kV).[58] Accordingly, in order to understand the characteristics of the ZnO surface defects, the cathodoluminescence of ZnO under low voltage excitation (5kV) was studied in this project.

All CL spectra were carried out inside an FEI Quanta 200 ESEM. The spatial resolution of the microscope is 3.0 nm and 10 nm at 30 keV and 3 keV, respectively. The microscope chamber was operated at pressure lower than 10^{-5} Torr. A Faraday cup was used to measure beam current. The layout of the cathodoluminescence setup is presented in Figure 3.5. The samples were placed on a cold stage, which allowed fast cooling from room temperature (300K) down to liquid nitrogen temperature (80K) and liquid helium temperature (5K). The samples were located at the focus point of a parabolic mirror, photons generated from the sample was collected by the mirror and subsequently directed through optical fibers to a detector. In this work, two detectors; an Ocean Optics QE65000 detector and a Hamamatsu S7011-1007 CCD sensor, were utilized on the CL system to collect full range CL spectra and high resolution CL of the near band edge region of ZnO, respectively. The QE65000 consists of a 1024 X 54

active pixel area with acquisition range of 200 to 1100 nm with 5 nm in a spectral resolution. The active pixel area of Hamamatsu S7011-1007 CCD sensor is 1044 X 124. The sensor was placed inside a head of a Hamamatsu C7021 detector. The light was dispersed by an Oriel MS 257 1⁄4m monochromator with a 1200 lines/mm grating. The spatial resolution of this set up is 0.1 nm over a 53 nm range.
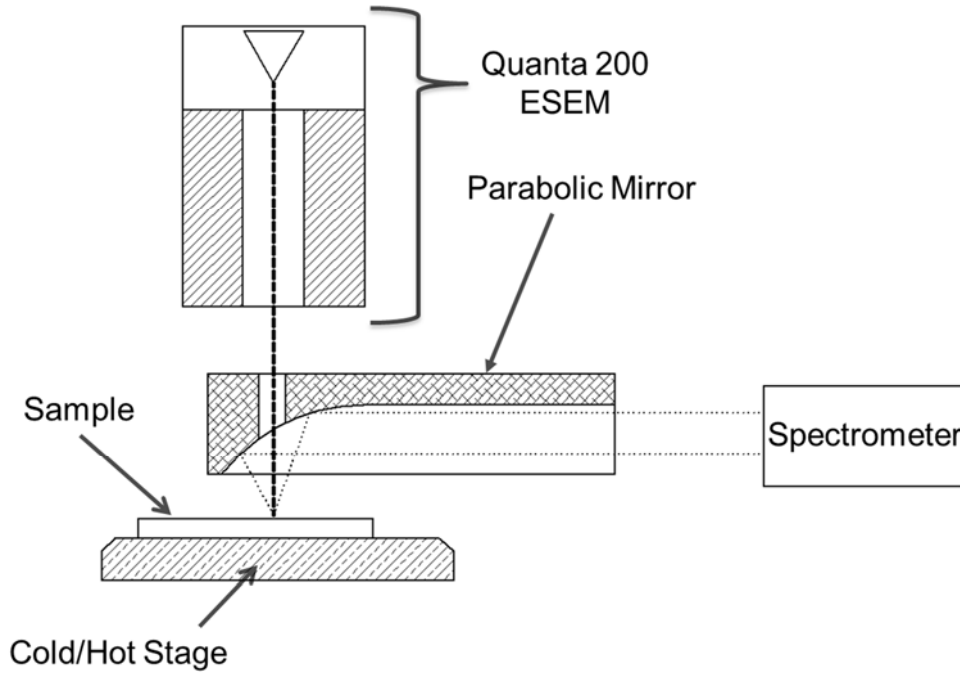
Figure 3.5: Schematic of CL experimental setup.

Both intensity and wavelength of all CL spectra were calibrated by an Oriel 63355 200W QTH calibrated lamp and mercury lamp, respectively. Equation 3.2 was used to calculate the intensity correction curve.

$$\text{Correction curve} = \frac{Normalized\ reference\ intensity}{Normalized\ measured\ intensity} \qquad (3.2)$$

The wavelength calibration curve of high resolution CL spectra was done by measuring atomic spectral lines of mercury after the ZnO spectra acquisition. The calibrated wavelength was subsequently converted into electron volts (eV) by the following equation:

$$\text{Photon energy (eV)} = \frac{1239.841856}{\lambda\ (nm)} \qquad (3.3)$$

To study temperature dependent CL, a Gatan C1002 liquid nitrogen cold stage was used for cooling samples down to 80K. A Gatan CF302 continuous flow liquid

helium cold stage was also used for cooling to 5K for collecting high resolution CL spectra. Finally, Peak-O-Mat program was utilized to do curve fitting and data analysis.

3.6 Photoluminescence Spectroscopy (PL)

Photoluminescence spectroscopy (PL) is an important tool for investigating a semiconductor's optical processes. It is sensitive to point defects and the signal generally originates near material surfaces. Since the characteristic radiative transition channels are regularly induced by point defects, PL is often used to determine electronic energy levels, binding energies as well as the chemical origin of point defects. It provides a large number of defect related luminescence information i.e. excitons, donor-acceptor pairs (DAP), phonon replica, thermal activation and quenching behaviour of transition lines etc. The non-radiative channels for carrier recombinations related to deep levels formation in the band gap can also be recognized from the PL intensity. In addition, PL is attractive for using with materials with poor conductivity since the electrical excitation or detection can be ignored.

In order to study the behaviour of surface defects of ZnO nanorods samples, PL measurements were done in a liquid helium bath cryostat allowing measurements from 7K to 300 K. A HeCd Laser with the 325 nm emission line and an output power of 36 mW was used to excite the ZnO samples above the band gap. The emitted light was dispersed by a Spex-1404 double monochromator (spectral resolution 50 μeV) and detected by a bi-alkali photodetector.

3.7 Synchrotron Light Experiments

Accelerated electrons moving with 99.9997% speed of light under magnetic field action emit the electromagnetic radiation known as Synchrotron light. Synchrotron light is a particularly high intensity light with a wide range of energies in the electromagnetic spectrum from infrared light to hard x-rays. It has several unique properties including high brightness, wide energy spectrum, tunable, highly polarised, and emitted in very short pulses. Due to a large number of useful properties of synchrotron light, it was used in an extensive range of advanced research in various

fields such as biosciences, medical research, environmental sciences, agriculture, minerals exploration, engineering, forensics as well as advanced materials even at the nanostructure scale. All synchrotron light experiments; X-ray photoemission spectroscopy (XPS) and x-ray absorption near-edge structure (XANES) were conducted on the Soft X-ray Spectroscopy beamline, Australian Synchrotron.[160]

3.7.1 X-Ray Photoelectron Spectroscopy (XPS)

X-Ray Photoelectron Spectroscopy (XPS) measures the energy of the detected electrons emitted from the sample after irradiation by monochromatic soft x-ray photons. XPS is used to determine the chemical identity and element concentrations in the sample by the following equation.

$$E_b = h\omega - E_k - \emptyset_d \qquad (3.4)$$

where E_b is the known binding energies of the elements, E_k is the kinetic energies of the emitted electrons, $h\omega$ is the energy of the X-ray photon, and $\emptyset_d$ is the work function of the detector.

The energy of the X-ray photons is finely tuned when performing XPS measurements at synchrotron facilities. At the Australian Synchrotron facility, the photon energy of the X-ray source covers wide range of energies from 90 eV to 1500 eV. By comparison, the XPS setups in normal laboratory utilize aluminium or magnesium targets as X-ray source with photon energies of 1486.6 eV (Al Kα) or 1253.6 eV (Mg Kα). Therefore, performing XPS measurements at synchrotron facilities allows for the XPS signal optimization at a specific photoemission by selecting the appropriate photon energy.

XPS is a highly surface sensitive analysis technique. Although the penetration power of X-ray photons in solids is in the range of 1 μm to 10 μm, the electron interaction with matter is higher than that of photons. Thus, the electrons mean free path is only tens of angstroms. The XPS signal is generated from only the photoelectrons created directly below the surface.

3.7.2 X-Ray Absorption Near Edge Spectroscopy (XANES)

X-Ray Absorption Near Edge Spectroscopy (XANES) is accomplished by measuring the X-rays absorption as a function of X-ray photon energy. Utilizing

XANES, the oxidation state as well as element coordination number in a material, and the elements site symmetry can be determined. In addition, the conduction band of the materials information is also provided by XANES since it is probing empty states. The X-ray photon energy is scanned over the core levels energy of primary elements in the samples. The electrons are excited from their levels and the holes are then generated. Subsequently, the electrons in a higher energy state recombine to the vacancy and release the energy in the form of photons or excite the electrons from a higher state to form Auger electrons.

XANES spectra cover over hundreds of electron volts above the core absorption edge. The peaks in an oscillatory fine structure shape in XANES spectra relate to the transitions of internal electrons between core levels. The oscillations in the XANES spectrum reflect a standing wave formation causing scattering between the photoelectron and neighbouring atoms.

XANES implemented in the Total Fluorescence Yield (TFY) and Total Electron Yield (TEY) mode was performed around the N K-edge. The incident X-ray beam was linearly polarized and perpendicular to the substrate surface. The photon energy scale was calibrated against the Au $4f_{7/2}$ peak at 84 eV from a clean gold film in electrical contact with samples.

3.8 Electrode Deposition and Gas Sensor Device Assembly

In order to assemble a gas sensor device and study the electrical properties of ZnO nanorods samples, the sensing ZnO nanorods arrays need two electrodes. A large active area is needed to achieve the highest interaction with gases; therefore, several pairs of electrodes are used in the sensor. The sensing layer is located between two sides of electrodes. The most common electrode pattern providing a large active area is an interdigitated pattern.

In this research, the electrodes are made from aluminium by a thermal evaporation technique and shaped into twelve fingers interdigitated pattern, as shown in Figure 3.6a. The dimension of each finger is 100 μm spacing and 900 μm length. The white area represents the active area (ZnO nanorods arrays) and aluminium electrodes are displayed in gray. To establish a device, the sensing layer with aluminium electrodes

is attached to a polycarbonate board and wired at the connectors as shown in Figure 3.6b. Copper tape and silver paste were used at the connectors (black dot in Figure 3.6b).

3.9 Current Voltage Characteristic Measurement

Current-Voltage analyses of ZnO nanorods samples with interdigitated aluminium electrodes were investigated at room temperature in the measurement chamber under an ambient air atmosphere utilizing source measurement unit; model 6157A electrometer/high resistance meter, Keithley. The measurement of current-voltage is carried out by applying a DC voltage (V) between two electrodes and monitoring the DC current (I).

An ideal current-voltage characteristic shows a linear curve obeying Ohm's law (Equation 3.5). General resistors reveal linear current voltage characteristic. The resistance (R) is constant in an ideal resistor. In a sample with good Ohmic behaviour, the junction resistance between metal (Al electrodes) and semiconductor (ZnO nanorods) can be neglected.

$$V = I \cdot R \tag{3.5}$$

The charge carrier mobility of samples can be inferred by measuring current-voltage characteristic since the electrical conductivity directly changes with the charge carrier mobility as shown in Equation 3.6.

$$\sigma = qn\mu \tag{3.6}$$

where σ is the conductivity, q is carrier charge, n is carrier concentration and μ is drift mobility of the carriers.

3.10 Gas Sensing Measurement

The sensing performance of ZnO nanorods gas sensors were evaluated using ammonia gas in air at room temperature. The gas sensor devices were investigated using a constant voltage of 1V, and the current was subsequently recorded as a function of time over the designed experiment cycles utilizing 6157A electrometer/high resistance meter, Keithley.

3.10.1 Gas Measurement System

The two main components in the gas measurement system are a gas flow controller unit and gas response recorder. Figure 3.7 shows the diagram of the gas flow controller unit consisting of a start switch (SW1), a stop switch (SW2), a programmable logic controller (PLC), a solenoid valve (SV), and two mass flow controllers (MFC1, and MFC2). The start and stop signals from SW1 and SW2 as well as the flow rates of MFC1 and MFC2 were obtained by PLC. Additionally, SV and two output flow rates were controlled by the PLC outputs. The second main component; the gas response recorder consisted of a Keithley Co, Ltd. electrometer model 6157A wired into the sensing chamber which was used to supply voltage and collect current.

The electrometer with 82350B PCI GPIB Interface Card from Agilent Technologies Co, Ltd. is connected to a computer. LabVIEW software from National Instrument Co, Ltd. was programmed in the computer to record the signal during the measurement cycles.
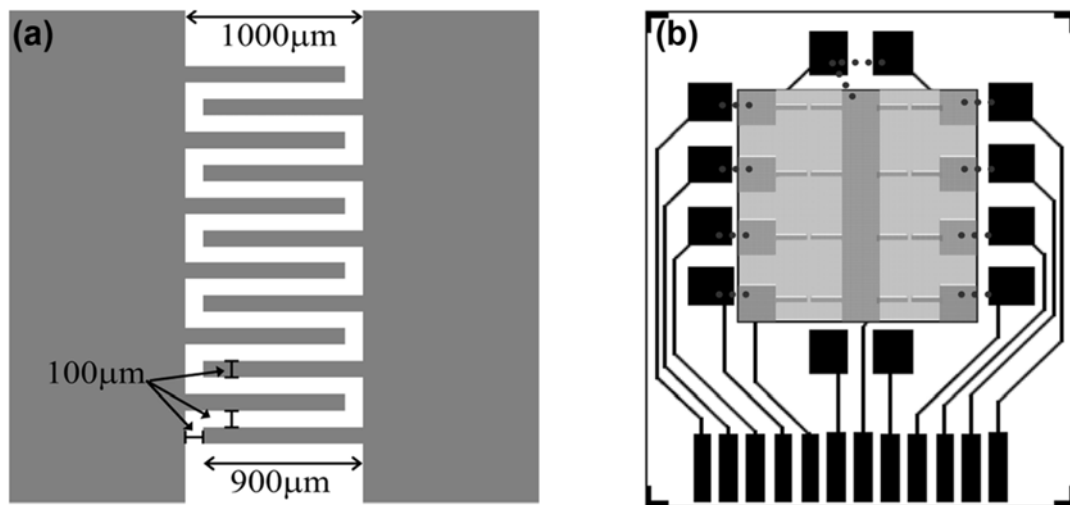
Figure 3.6: (a) Twelve fingers of the interdigitated electrode (shown in gray). (b) Gas sensor device comprised of ZnO sensing layer (light gray square), aluminum electrodes (gray), polycarbonate board (outermost square) with conduction line (black line), and connection wires (black dot).
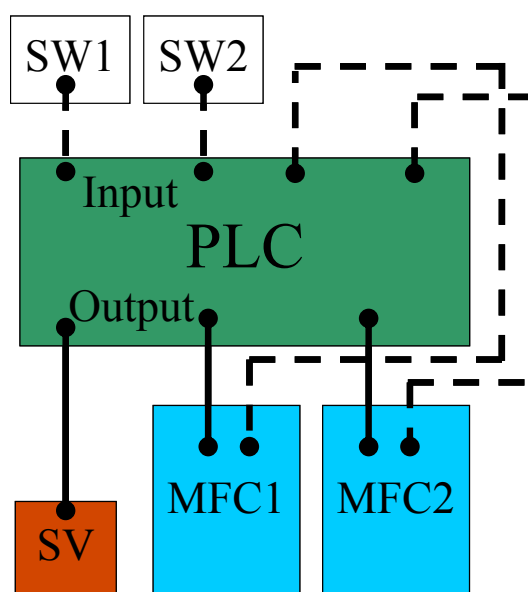
Figure 3.7: Gas flow controller unit diagram; input channels are shown in dash lines and output channels are shown in solid lines.

The gas measurement system consisted of 5 parts; gas sources, flow regulators, sensor chamber, signal acquisition, and waste disposal. The homebuilt gas measurement system used in this project is shown in Figure 3.8. The ammonia vapour was generated by flowing carrier gas (air) into the liquid ammonia analyte reservoir. The flow rates of ammonia gas and carrier gas were regulated by MFC1 and MFC2, respectively. Both gases were introduced into the sensor chamber and subsequently mixed and then exhausted into the waste reservoir. The ammonia gas concentration in the sensor chamber was adjusted by controlling the flow rates of MFC1 and MFC2 in the fixed total flow rate of 100 mL/min.

3.10.2 Designed Experimental Procedure

The gas sensor devices were put into the measurement chamber and the electrical properties measured. A constant voltage of 1V is applied to the gas sensor devices and then the current is recorded over the experiment cycles as a function of time using a Keithley model 6157A electrometer/high resistance meter.

There are four steps to run experiments and control the external parameters:

(i)   Leave the sensors under ambient air in the chamber for 1 hour.

(ii) Purge air for 30 minutes.

(iii) Apply voltage and obtain baseline for 20 minutes.

(iv) Flow analyzed (NH$_3$) and clean with air for 10 and 10 minute cycles.

The pre-measurement steps; step (i) and (ii), were done to control the external parameters. To start the measurement cycles, the 20 ppm ammonia gas was purged into the sensor chamber and switched with air during the cleaning period. Then the ammonia concentrations systematically increase by 20 ppm in each cycle to highest concentration 100 ppm. After the gas responses were received, the sensitivities were then calculated by Equation 3.7.

$$S = \frac{I_g}{I_a} \qquad\qquad (3.7)$$

where S is a gas sensitivity, I_g is a current response at each ammonia concentration, and I_a is an average current response at the first measurement period (base line period)
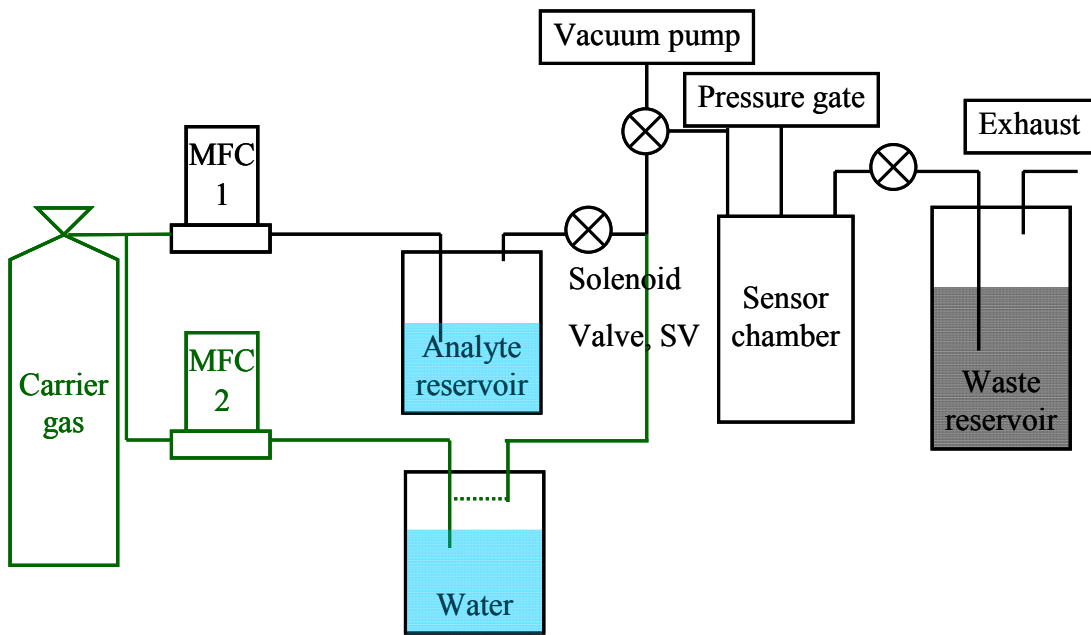
Figure 3.8: Homebuilt gas measurement system; dotted line represents the shortcut path when the dry measurement starts.

CHAPTER IV

TAILORING DEEP LEVEL SURFACE DEFECTS IN ZnO NANORODS FOR HIGH SENSITIVITY AMMONIA GAS SENSING

4.1 Summary

The influence of deep level surface defects on electrical and gas sensing properties of ZnO nanorod NH_3 (g) sensors was studied. ZnO nanorods 50−60 nm in diameter were synthesized via low-temperature hydrothermal growth at 90 °C on sapphire substrates. The as-grown nanorods exhibited a cathodoluminescence (CL) peak centered at 1.90 eV (YL), attributed to Li_{Zn} deep acceptors or O interstitials. Subsequent annealing in O_2 at 1 atm and Zn_{vap} at 650 °C produced broad CL peaks centered at 1.70 eV (RL) and 2.44 eV (GL), respectively. The RL and GL have been ascribed to acceptor-like V_{Zn} and donor-like V_O related centers, respectively. Electrical and gas sensing measurements established that the NH_3 gas response sensitivity was 22.6 for O_2 anneal (RL), 1.4 for Zn_{vap} anneal (GL), and 4.1 for the as-grown (YL) samples. Additionally, treatment in H-plasma quenched the RL and inverted the NH_3 electrical response due to the incorporation of H donors. Changes in the gas sensing response are explained by a shift in the position of the ZnO Fermi level relative to the chemical potential of NH_3 gas due to the creation of near surface donor or acceptors. These data confirm that ZnO nanorods arrays can be tailored to detect specific gas species.

4.2 Introduction

Zinc oxide (ZnO) has attracted great attention over the past few decades to enable applications in optical devices, piezoelectric devices, solar cells, and gas sensors.[2, 4, 161] In general, the gas sensing can be measured by monitoring changes in the surface electrical conductance of ZnO upon exposure, owing to the electron transfer between the ZnO surface and target gas molecules.[162] Because of their high surface area, ZnO nanostructures such as nanoparticles, nanowires,[16, 162-163] nanorods,[164-165] and

nanotubes[166] are fabricated and used as gas sensors having a significantly higher sensitivity in comparison to those using ZnO microcrystal thin films.[165] A number of researchers have confirmed that then sensitivity of these high surface area ZnO gas sensors is strongly dependent on their operating temperature;[115, 165, 167-168] i.e., the higher the temperature, the higher the sensitivity. Accordingly, nanostructured ZnO materials have been extensively reported as highly sensitive gas sensors when operating between 150 and 400 °C[15, 163, 169-170]5, or at above 400 °C.[115, 171] Recently, room temperature gas sensing devices composed of ZnO nanorods were developed to detect: H_2 gas at a lowest concentration of 150 ppm,[165] alcohol gas at concentrations down to 0.5 ppm,[172] and NH_3 gas at concentrations of 300[173] and 500 ppm.[174] Here the gas sensing mechanism that governs the ZnO surface conductivity has been attributed to low-temperature surface reactions, involving adsorbed molecular or atomic oxygen as well as hydroxyl groups. Several works have indicated that the electrical response can be significantly improved in ZnO nanorods by controlling their nanostructural properties specifically their morphology, particle size, and surface area[17, 165] as well as the carrier concentration.[15-16, 18] Moreover, recent experimental and theoretical studies have shown that the surface defect chemistry of ZnO nanorods has a significant effect on the sensitivity to different gas species. Additionally, it has been suggested that the sensing capabilities of ZnO can be improved by incorporating dopants such as Al, Sn, and Fe into the ZnO structure to generate point defects that serve as catalysts enhancing the electron transfer between ZnO and molecular gas[169] or to stabilize oxygen vacancies.[169-170] The exact role of these surface defects on the surface conductivity remains controversial; however, a number of models have been suggested, such as providing reactive sites for oxygen adsorption, inducing surface band bending, and varying the carrier concentration by acting as donors or acceptors.[15-16, 163, 169] This research focuses on the systematic introduction of different types of surface point defects in ZnO nanorods through controlled growth and thermal processing in oxidizing (O_2) and reducing (Zn vapor) atmosphere. The ZnO nanorods arrays were formed on sapphire substrates without the use of a catalyst via a low-temperature (90 °C) hydrothermal growth technique. Scanning cathodoluminescence (CL) spectroscopy and imaging is a useful technique for studying surface defects in semiconducting materials with high spatial resolution. Surface defects in the ZnO nanorods were characterized by measuring low-temperature CL spectra at low

acceleration voltages, at which a surface layer of only a few tens of nanometers is excited. ZnO nanorods having surface defects of various types were further employed for fabrication of gas sensing devices and their electrical responses to gas exposure probed and compared with the surface point defect chemistry. In this work, ammonia gas was employed as a model reductive gas in order to illustrate the inter-relationships between DL defect type, electrical properties, and sensing performance in nanostructured ZnO. The results confirm that post-growth-controlled atmosphere heat treatment can be used to mediate the Fermi level position of the ZnO nanorods through the creation of acceptor or donor native near surface defects, which governs the sign and magnitude of the electrical response to NH_3 gas.

4.3 Experimental Section

4.3.1 Synthesis of ZnO Nanorods and Post-Growth Processing

Nucleation of ZnO was induced by applying a few drops of zinc acetate solution (5 mM in ethanol) on a sapphire substrate, followed by sample baking at 250 °C for 20 min. The nucleated substrates underwent a hydrothermal treatment in seed aqueous mixture containing 0.025 M zinc nitrate hexahydrate ($Zn(NO_3)_2 \cdot 6H_2O$, 98% purity) and 0.025 M hexamethylenetetramine ($C_6H_{12}N_4$, ≥99.0% purity) at 90 °C for 3 h to afford as-grown ZnO nanorods.[175-176] The as-grown samples were then annealed at 650 °C for 30 min in either O_2 or Zn vapor. Hydrogen plasma treatment was carried out using a mild hydrogen radio-frequency plasma for 20 min (10 W, 370 K sample temperature).

4.3.2 Analysis Techniques

The morphologies and crystal structures of as-grown and annealed ZnO nanorods were characterized using field-emission scanning electron microscopy (FE-SEM) and powder X-ray diffraction (XRD), respectively. CL spectra were collected on a FEI Quanta 200 scanning electron microscope equipped with an Ocean Optics QE6500 system. All CL spectra were corrected for the total response of the light

collection system. Measurements of electrical and gas sensing were carried out with a 6157A electrometer (Keithley Co, Ltd.).

4.3.3 Fabrication of ZnO Nanorods Gas Sensor and Gas Sensing Measurement

The 12 fingers interdigitated pattern of aluminum electrodes with 100 μm spacing and 900 μm length was fabricated on the ZnO nanorods using a thermal evaporation technique. To determine the gas response, the nanostructured ZnO-based devices were subjected to ammonia gas exposure at various concentrations in an air carrier gas, with an applied constant voltage (1.0 V) over specifically designed measurement and cleaning cycles (10 min measuring and 10 min cleaning). The electrical response upon exposure to ammonia gas was attained by the measuring current as a function of exposure time.

4.4 Results and Discussion

Figure 4.1a shows SEM images of the as-grown ⟨0001⟩ ZnO nanorod sample, indicating that the hydrothermal growth treatment provided a high density of uniform hexagonal ⟨0001⟩ nanorods approximately 50−60 nm in diameter. The ⟨0001⟩ nanorods are aligned over a range of angles to the substrate normal so that their sidewalls overlap each other, allowing multiple contacts between rods. Cross-sectional SEM images (not shown) indicate that the typical length of the ZnO nanorods is around 2000 nm, which was considerably thicker than a nanoscale wetting layer. No change in the size and shape of the ⟨0001⟩ ZnO nanorods was observed following the controlled atmosphere heating at 650 °C heating, confirming that no overgrowth layer was deposited (SEM images are presented in Figure 4.2).

Powder XRD profiles of the as-grown and annealed samples are given in Figure 4.1b, and diffraction peaks can be indexed to the wurtzite phase of ZnO, hexagonal lattice (P63*mc*) with lattice constants of a = 0.3249 nm and c = 0.5207 nm as calculated from ICSD using POWD-12++. The presence of the Bragg diffraction peaks in addition to the (0002) appears because the ZnO nanorods are not strictly perpendicular to the substrate plane. No significant change in the position of XRD peaks

was observed after annealing in O_2 or Zn atmosphere, indicating that no microstrain or extended defects were introduced during the thermal processing. The change in the relative intensity of the XRD peaks after heating arises from slight reorientation of the ⟨0001⟩ ZnO nanowires relative to the substrate plane.
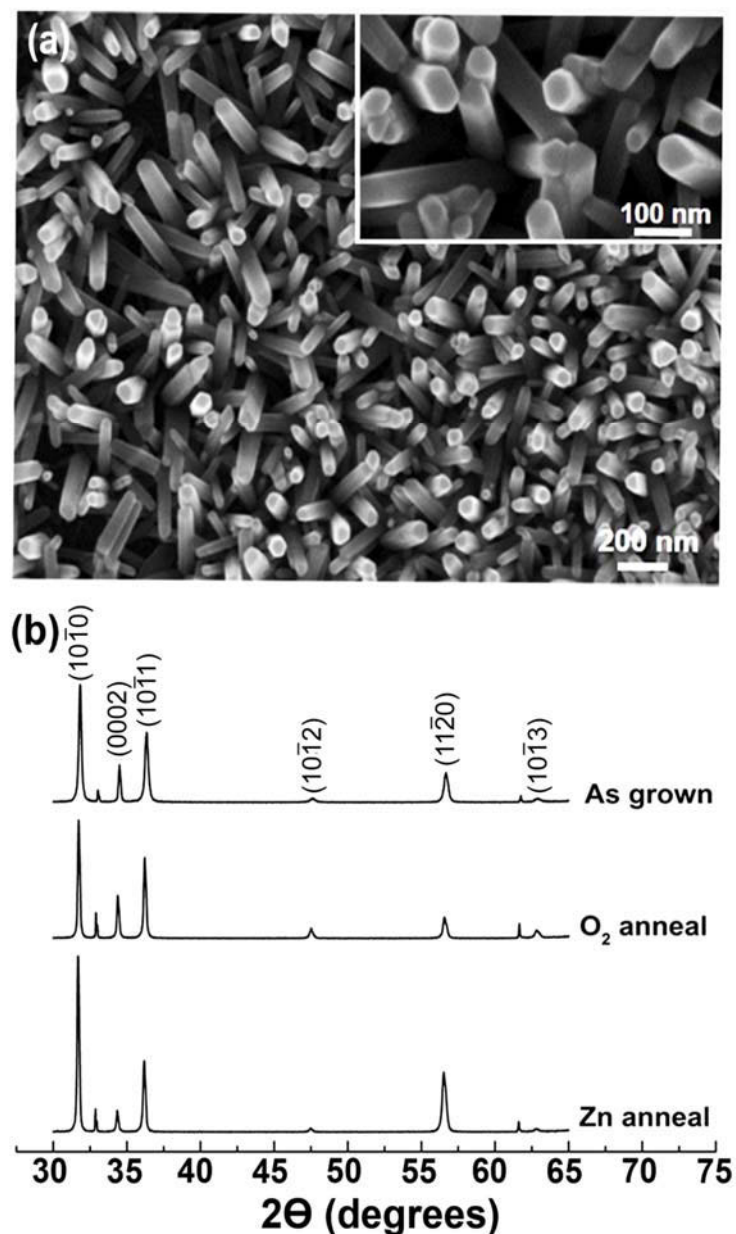
Figure 4.1: (a) SEM images of as-grown ZnO ⟨0001⟩ nanorods on a sapphire substrate and (b) PXRD patterns of as-grown, O_2 and Zn atmosphere annealed ZnO nanorods exhibiting the wurtzite crystal structure. The change in the relative intensity of the diffraction peaks arises from a slight reorientation of the nanorods relative to the substrate after thermal annealing.
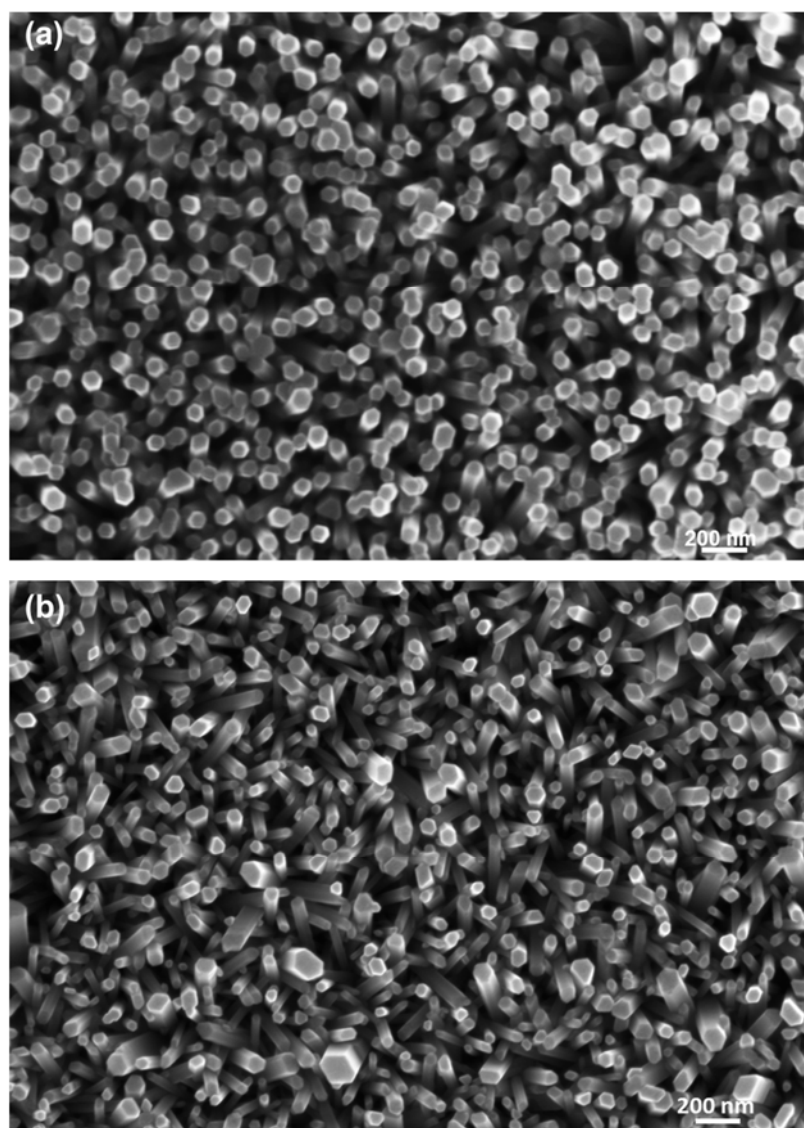
Figure 4.2: SEM images of ZnO nanorods after annealing in (a) O_2 and (b) Zn atmosphere.

Figure 4.3a highlights the CL spectra of the Zn vapor annealed, as-grown, and O_2 annealed ZnO nanorods at 80 K, which exhibit predominantly green luminescence (denoted as GL), yellow luminescence (denoted as YL), and red luminescence (denoted as RL) centered at 2.44, 1.90, and 1.70 eV, respectively. In order to probe defects on the nanorod surface, CL spectra were collected at a low acceleration voltage of 5 kV where the maximum photon generation depth is approximately 37 nm using the CASINO simulation code.[177] The CL spectra clearly show that each ZnO sample exhibits a specific broad signature luminescence band, reflecting the different types of DL defects at the ZnO surface following growth and postgrowth annealing. The

results in Figure 4.3a indicate that the hydrothermally synthesized ZnO nanorods produce a visible emission corresponding to YL. On the other hand, annealing the as-grown ZnO nanorods under an oxidative atmosphere resulted in ZnO producing RL, whereas annealing under Zn vapor led to ZnO producing GL. These CL data confirm that different DL types of point defect can be incorporated into the ZnO nanorods using controlled gas atmosphere heat treatment.
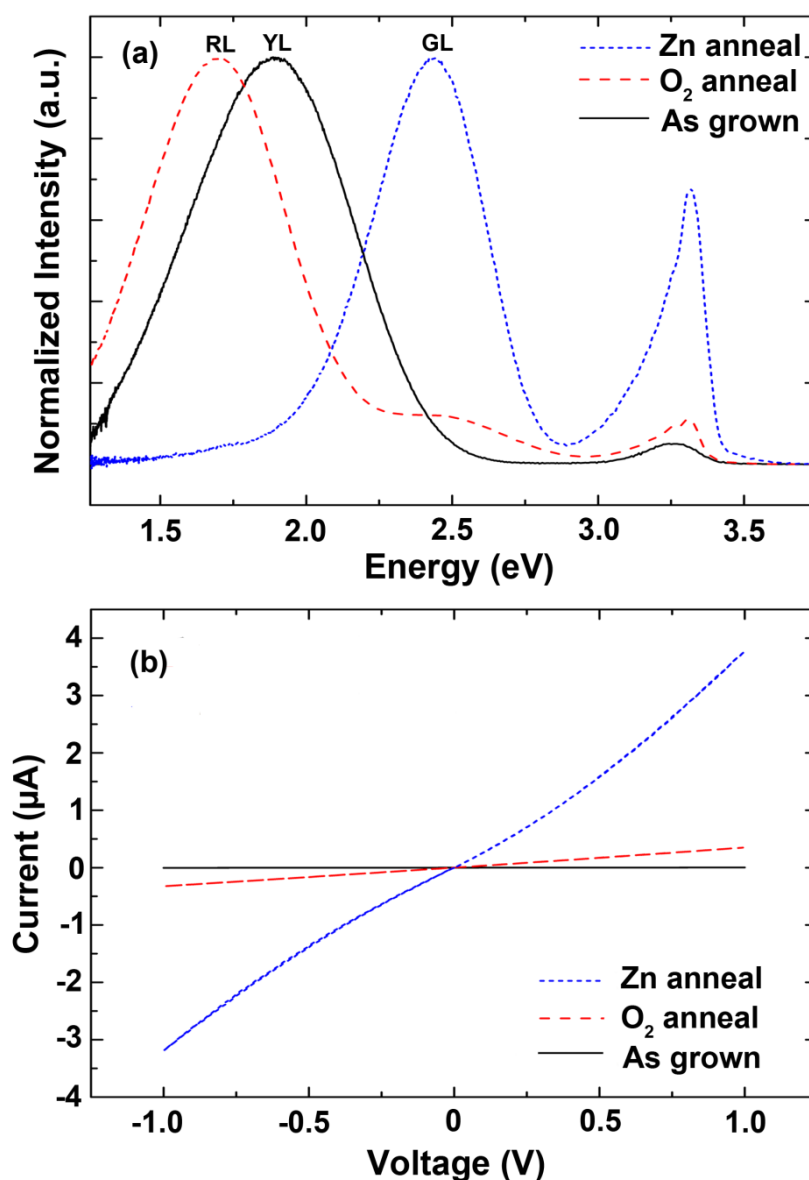
Figure 4.3: (a) Normalized CL spectra collected from Zn annealed, as-grown, and O_2 atmosphere annealed ZnO nanorods at 5 kV, 80 K, scan area = 50 μm × 43 μm, and beam current of 0.2 ± 0.02 nA. The ratio of raw intensities of GL, YL, and RL centered at 2.44, 1.90, and 1.70 eV, respectively, is 0.057:0.204:1. All spectra were normalized

to the DL peaks. (b) Room temperature I−V characteristics of the Zn annealed, as-grown, and O_2 atmosphere annealed ZnO nanorods measured under an ambient atmosphere.

The point defects formation reactions upon annealing the as-grown ZnO nanorods under oxygen and Zn vapor atmosphere are given in equation 4.1 and 4.2. In addition, the intensity ratio of near-band-edge (NBE) to DL emissions at approximately 3.3 eV was increased after annealing, especially in Zn atmosphere annealed ZnO nanorods, suggesting that defect concentrations were lowered by thermal annealing.
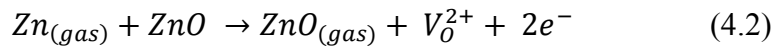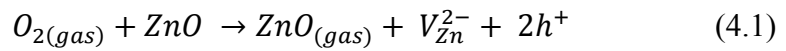
$$O_{2(gas)} + ZnO \rightarrow ZnO_{(gas)} + V_{Zn}^{2-} + 2h^+ \qquad (4.1)$$

$$Zn_{(gas)} + ZnO \rightarrow ZnO_{(gas)} + V_O^{2+} + 2e^- \qquad (4.2)$$

The production of YL from the hydrothermally grown ZnO nanorods was also observed and systematically studied by photoluminescence.[79] It was also suggested that the PL yellow emission was due to the presence of OH groups or $Zn(OH)_2$ on the surface of ZnO nanorods rather than oxygen interstitials. It has been shown that the YL in hydrothermally grown ZnO could be related to deep Li_{Zn} acceptors.[55, 83] Notably, adsorption of OH groups on the ZnO surface is favourable under hydrothermal treatments, and the chemical origin of YL produced by hydrothermally grown ZnO could be different than those obtained by other preparation methods.

From the CL spectra (Figure 4.3a), the appearance of RL due to annealing in an oxygen atmosphere indicates the generation of a different type of point defect at the ZnO nanorod surface. It should be highlighted that the shift of YL to RL upon oxidative annealing was in excellent agreement with Djurisic's report, [79] suggesting that RL originates from zinc vacancy defects. The red and orange-red emissions were previously assigned as originating from oxygen interstitials (O_i),[80, 82] zinc vacancies (V_{Zn}),[79] and substitutional nitrogen defects on oxygen sites.[178] Our view is that the RL is related to V_{Zn} or V_{Zn} related complex due to a surface chemical reaction where the $O_2(g)$ reacts with the ZnO surface removing a Zn atom and creating a V_{Zn} and ZnO vapor as shown in equation 4.1. This assignment is consistent with theoretical calculations[40] that V_{Zn} with the lowest formation energy can be easily formed in O-rich ZnO. Electron paramagnetic resonance (EPR) and X-ray absorption spectroscopies were employed to probe the presence of nitrogen defects. No EPR hyperfine signal corresponding to nitrogen was observed. X-ray absorption near-edge structure

(XANES) spectra at the N K-edge (Figure 4.4) were collected from the as-grown and annealed ZnO nanorods and compared with nitrogen-implanted ZnO nanoparticles and bulk ZnO crystals. These data confirm the absence of N in the ZnO nanorods studied in this work. To elucidate the chemical nature of the defect involved in the RL, the O_2 atmosphere annealed ZnO was subjected to a hydrogen plasma treatment, causing the RL to completely quench (Figure 4.5).
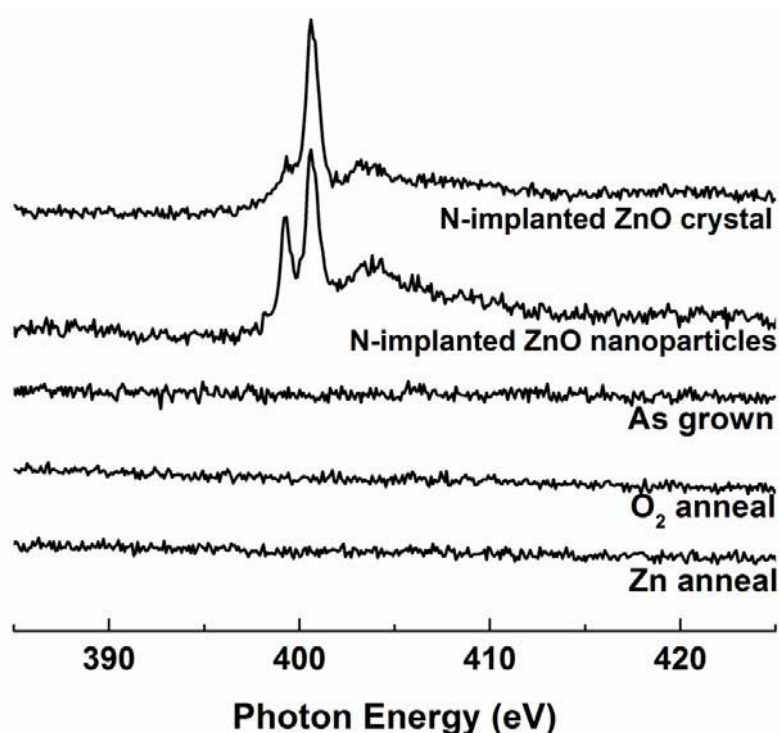
Figure 4.4: N *K*-edge XANES spectra of Nitrogen implanted ZnO crystal and ZnO nanoparticles, and as grown, O2, and Zn atmosphere annealed ZnO nanorods.

The RL suppression can be explained by the passivation of V_{Zn} by hydrogen donors through the formation of either (V_{Zn}−H) or (H−V_{Zn}−H) complexes.[179] These results suggest that the RL may originate from either V_{Zn} or a V_{Zn}-related center, consistent with an assignment by Wang et al.[180]

The presence of the GL after annealing in a zinc-rich atmosphere is evidence of a creation of another different type of defect type at the ZnO nanorod surface (see equation 4.2). It is widely agreed that GL at around 2.5 eV is initiated from singly ionized oxygen vacancies (V_O^+), neutral V_O^0, or V$_o$-related centers.[181-183] Recently it has suggested that this emission may be due to V_{Zn} centers;[184] however, none of the

experimental results in this work support this assignment in our low temperature grown hydrothermal ZnO nanorods.

Figure 4.3b reveals the current−voltage (I−V) characteristics, under an ambient air atmosphere, of ZnO nanorod gas sensors fabricated from the as-grown, O_2, and Zn atmosphere annealed ZnO. The electrical conductivity of the samples substantially increases after annealing, particularly in a Zn-rich atmosphere. In addition, the maximum current (measured at 1.0 V) obtained from the as-grown ZnO based device was 3.34 nA. In comparison, an approximately 100- and 1000-fold enhancement in current resulted after annealing in O_2 and Zn vapor atmosphere, respectively. It is important to note that only a 20- fold enhancement in current was found following annealing in an Ar atmosphere under identical conditions to the O_2 and Zn vapor heat treatments (Figure 4.6). This observation conclusively shows that the increase in conductivity following O_2 and Zn atmosphere annealing was the result of modification to the surface defect chemistry with thermally induced improvement in the crystallinity of the ZnO nanorods playing only a minor role.
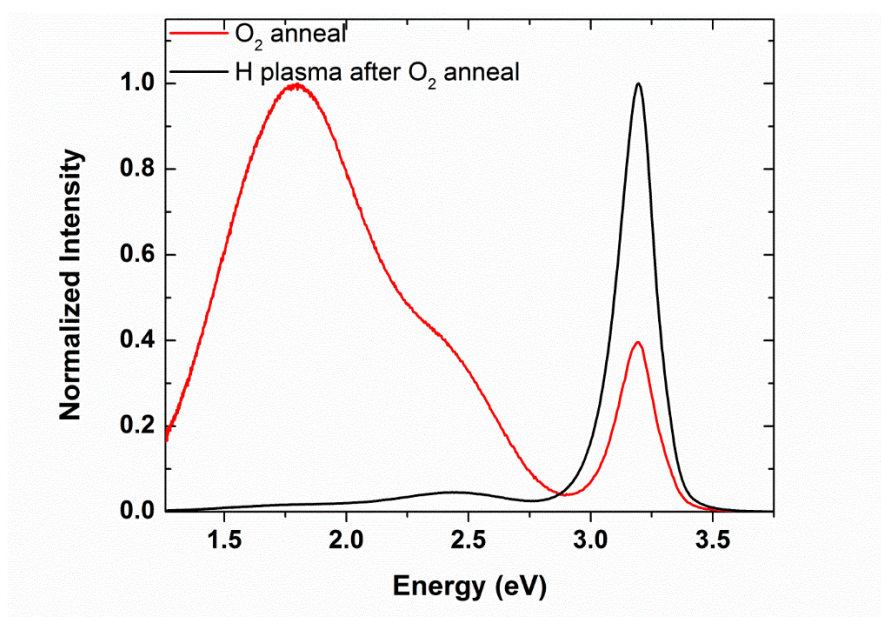
Figure 4.5: CL spectra collected from O_2 atmosphere annealed and H plasma of O_2 annealed ZnO nanorods at 5kV, 80K. The spectra were normalized to the maximum intensity peaks.

The ammonia gas sensing properties of ZnO nanorod sensors were examined at room temperature in order to avoid any alteration of surface defects, which may occur at elevated temperatures and to evaluate the performance of these ZnO

sensors under practical operating conditions. Note that all $I{-}V$ curves in Figure 4.3 show linear characteristics indicating good Ohmic behavior, which is ideal for sensor applications. The NH₃ gas response data (Figure 4.7) were collected in five measurement cycles, with higher concentrations of gas being employed in subsequent runs. The gas sensor was purged with air prior to each measurement cycle. The NH₃ response sensitivity (S) can be determined using the expression $S = I_g/I_a$, where I_g is the current measured during NH₃ gas flow and I_a is the baseline current (air flow) before exposure. From Figure 4.7, it was found as expected that the sensitivity was enhanced when NH₃ gas concentration increased from 20 to 100 ppm for all samples. Variation in gas sensing properties of ZnO with different defect types (YL, RL, and GL) was observed. At 100 ppm of NH₃ gas, the highest sensitivity was observed from the sensor fabricated from the O2 annealed ZnO (S = 22.6; RL) in comparison to the as-grown nanorods (S = 4.1; YL) and the Zn vapor annealed ZnO (S = 1.4; GL). Although the sensitivity of the as-grown nanorod-based sensor is relatively low, it is ca. 50 times higher than the room temperature NH₃ gas sensor based on hydrothermally grown ZnO nanorods previously reported by Ang et al.,[174] measured at 500 ppm (when S was calculated by the same equation above). The sensitivity of O₂ atmosphere annealed ZnO based device was found to be ca. 280 times higher than that reported by Ang et al.[174] More importantly, the NH₃ gas sensitivity of hydrothermally grown oriented ZnO nanorod arrays (S < 8.5)[185] sensor at a temperature of 250 °C with a gas concentration of 200 ppm was not significantly higher than our ZnO nanorod device operating at room temperature. Possible surface reactions related to the NH₃ gas response sensitivity of sensors fabricated by the ZnO nanorods having particular DL defect emission are given as follows.

$$O_{2(gas)} + e^- \leftrightarrow O_{2(ads)}^- ; \quad \text{T} < 150\,°\text{C} \tag{4.3}$$

$$4NH_{3(gas)} + 3O_{2(ads)}^- \leftrightarrow 6H_2O_{(gas)} + 2N_{2(gas)} + 3e^- \tag{4.4}$$
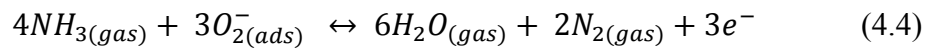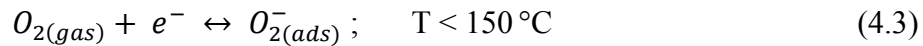
The observed increase in electrical conductivity of the ZnO nanowires is generally ascribed in the literature to the following surface chemistry model. Under air flow, O₂ molecules are absorbed on the ZnO surface and convert to oxygen ions through depletion of electrons from the conduction band of ZnO, equation 4.3, lowering its electrical conductivity.[164-165, 186-187] Upon exposure to NH₃ gas, the increase in the electrical conductivity response of the ZnO gas sensor (I_g) is attributed to surface

reactions between NH_3 with adsorbed oxygen ions. This process induces desorption of the surface O_2 as shown in equation 4.4, resulting in electrons being released back to the ZnO conduction band subsequently reverting the electrical conductivity toward the initial pre-NH_3 exposure levels. This particular model, however, is inconsistent with the CL spectroscopy analysis of the ZnO surface defects in this work. It is widely reported in both theoretical[188] and experimental[189] studies that surface oxygen vacancies enhance the adsorption of O_2 via a dissociative adsorption process. Accordingly, the ZnO nanorod sample annealed in Zn vapor with the high Vo concentration, as evidenced by the strong GL, should exhibit the highest coverage of adsorbed O_2 and consequently the highest sensitivity to the NH_3 gas. Conversely, the ZnO nanorod specimen annealed in O_2 with its V_{Zn}-rich surface, as indicated by the strong RL, should display a lower sensitivity. However, the NH_3 sensitivity results shown in Figure 4.7 reveal exactly opposite behavior with the RL sample exhibiting the greatest NH_3 sensitivity and the GL sample the weakest. Significantly, RL samples exposed to H-plasma exhibited a negative electrical response (Figure 4.7g,h). Given these data, an alternate model involving annealing induced shifts of the Fermi level position of the ZnO nanorod is presented to explain the NH_3 conductivity and its relationship to the ZnO surface defect chemistry.
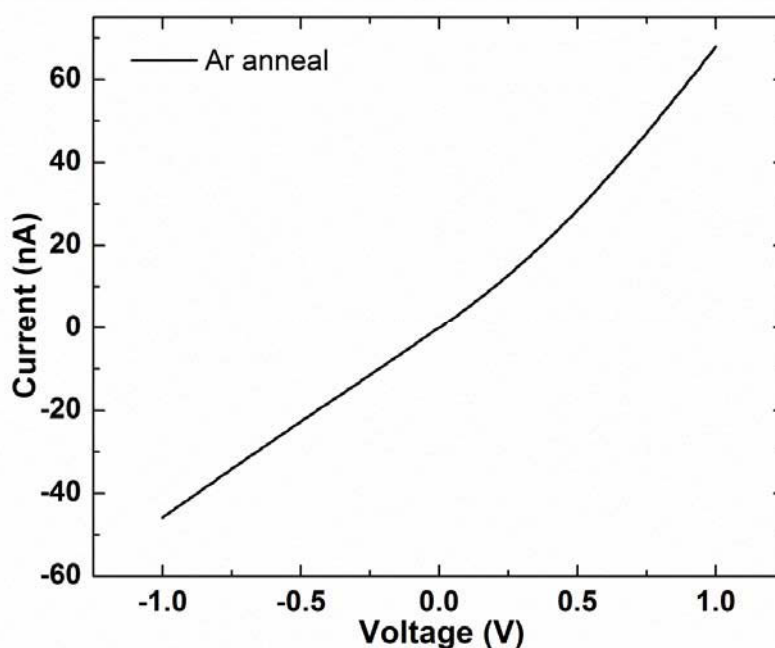
Figure 4.6: Room temperature *I-V* characteristic of the Argon atmosphere annealed ZnO nanorod gas sensor.
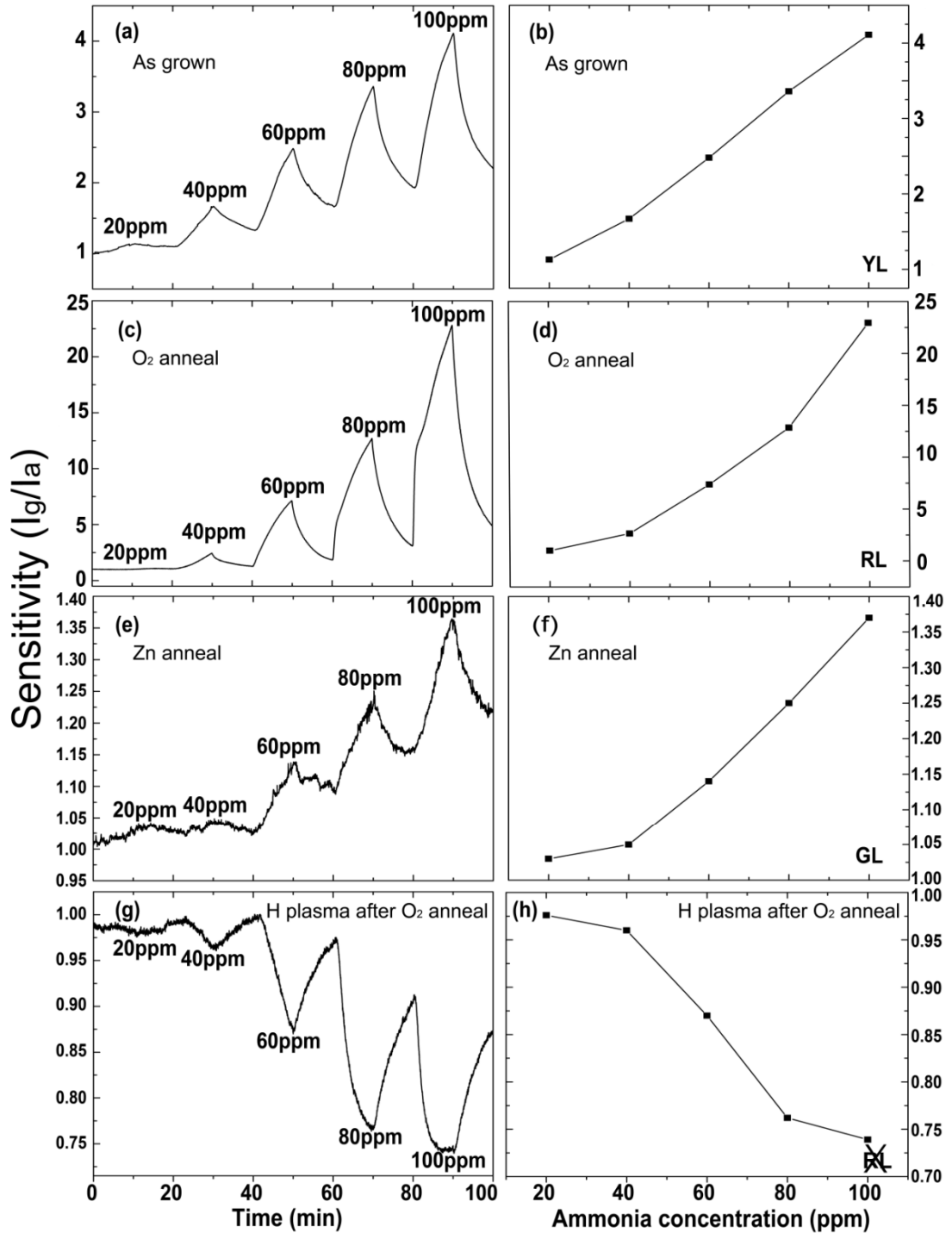
Figure 4.7: Sensitivity as a function of measurement time for (a) as-grown, (c) O_2, (e) Zn, and (g) H plasma after O_2 annealed ZnO nanorod sensors and sensitivity as a function of ammonia gas concentration for (b) as-grown, (d) O_2, (f) Zn, and (h) H plasma after O_2 annealed ZnO nanorods sensors at room temperature. Labels in the bottom right corner of (b), (d), (f), and (h) indicate the signature luminescence (YL, RL, GL, and RL suppression) exhibited by ZnO nanorods employed in the fabrication of each gas sensor.

Both bulk and nanostructured ZnO are n-type due to an autodoping process inducing the inadvertent incorporation of intrinsic donors, such as H, Zn_i, and V_o as well as their complexes that push the Fermi level (EF) toward the conduction band.[40] Charge will flow either to or from the ZnO surface and the adsorbed NH_3 gas species, depending on the position of the ZnO EF compared with chemical potential (ECP) of the adsorbed NH_3 gas.[105, 190] If the EF is below the NH_3 ECP, then charge with be transferred from the gas species to the surface and vice versa for EF above the NH_3 ECP. Accordingly, annealing ZnO in O_2 atmosphere produces V_{Zn} acceptors lowering the EF toward valence below ECP, promoting electrons to move from the NH_3 to the ZnO nanorod and increasing the surface conductivity. Conversely, the generation of V_o donors by annealing in Zn vapor raises EF toward the conduction band above ECP, causing electrons to shift from the ZnO to the adsorbed NH_3 and decreasing the surface conductivity. Additionally, the negative electrical response (Figure 4.7g) following hydrogen plasma treatment of the O_2 anneal sample clearly confirms this alternate model. The hydrogen in ZnO always acts as a donor.[94, 191] Consequently, H incorporation via the hydrogen plasma treatment pushes the EF toward the conduction band above the NH_3 chemical potential, leading to electron flow in the opposite direction.
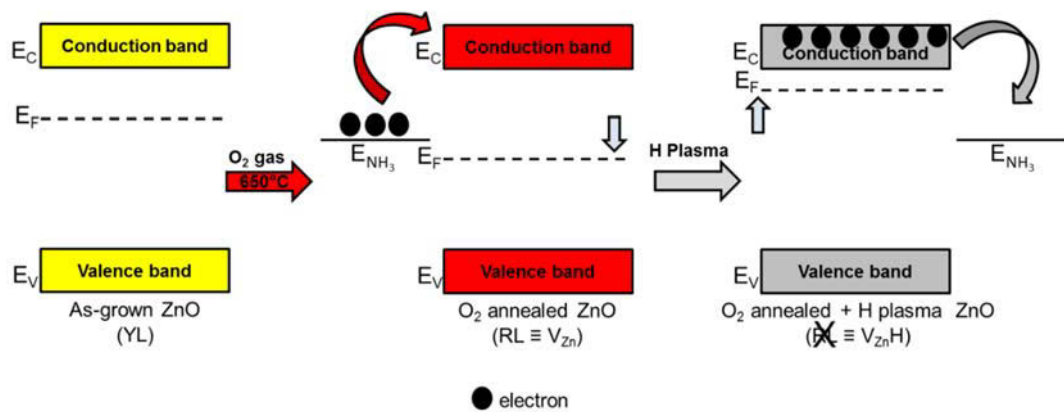
Scheme 4.1: The alteration of the ZnO Fermi level position owing to near surface acceptor (RL: V_{Zn}) and donor (RL suppression: Hydrogen) after post growth processes.

4.5 Conclusions

In summary, the low temperature (90 °C) growth technique employed in the preparation of ZnO nanorods in sensor devices shows great promise as an alternative

method to the existing high temperature routes due to its simplicity, application to temperature sensitive substrates, energy efficiency, and reproducibility in obtaining nanostructured ZnO for room temperature NH_3 sensor applications. CL spectroscopy confirmed that post-growth-controlled atmosphere heat treatment can be used to mediate the Fermi level position of the ZnO nanorods through the creation of acceptor or donor native near surface defects, which governs the sign and magnitude of the electrical response to NH_3 gas. Specifically a room temperature NH_3 sensitivity of S = 22.6 was achieved by heating in O_2 atmosphere at 650 °C that was 5 times greater than S for as-grown ZnO nanorods. The reported findings on the inter-relationship between surface point defects, electrical properties, and gas sensing properties of nanostructured ZnO will facilitate the development of future, low cost, high-sensitivity, room temperature gas sensor devices tailored for specific applications.

CHAPTER V

THE SURFACE ELECTRONIC STRUCTURE OF ZnO

NANORODS: THE ROLE OF SURFACE DEFECTS

5.1 Summary

The effect of native point defects on the surface electronic structure of low temperature (90 °C) hydrothermally grown ZnO nanorods is investigated using X-ray photoemission spectroscopy (XPS), X-ray Absorption Near-Edge Structure (XANES), electron spin resonance (ESR), low voltage cathodoluminescence spectroscopy, sub band gap photoluminescence spectroscopy as well as electrical I-V measurements. The as-grown surface defect structure was altered by controlled atmosphere annealing at 650ºC in both O_2 gas and Zn vapor environments. From the correlative characterization measurements it is established that the degree of surface band bending and surface conductivity is controlled by amount of adsorbed ambient gas species (O_2, H_2O and OH), which is mediated by type and concentration of intrinsic surface point defects. Specifically a direct relationship is established between peaks at 532.0 eV and 532.7 eV in O1s XPS spectra attributed to presence of surface oxygen vacancies and oxygen in adsorbed gas species. Singly ionized oxygen vacancies are confirmed to be stable on the ZnO nanorod surface producing (i) a pronounced shoulder feature in the valence band XPS spectra around 3 eV below the Fermi level, (ii) a strong broad green CL peak positioned at 2.43 eV (300K) and (iii) an intense ESR line at $g \cong 2.01$ (10 K).

5.2 Introduction

A key attraction of ZnO relates to it useful and interesting surface electronic properties, which are significantly enhanced in ZnO nanostructures with their extreme surface-to-volume ratios.[192-195] Gas – solid interfacial chemical reactions can produce either a low conductivity surface electron depletion layer or a high conductivity surface electron accumulation layer via physisorption and chemisorption of ambient or target

gas species on the ZnO surface. For instance, electron acceptor O_2 gas molecules can capture electrons from the bulk creating a negative surface charge above an electron depletion layer with corresponding upward band bending. Conversely electron donor gas species such as water vapor molecules and hydroxyl groups can cause the opposite effect and accordingly form an electron accumulation layer with downward band bending. In typical semiconductors the type of surface adsorbed gas depends on the bulk electrical properties: n – type, acceptor surface states with upward band bending and p – type, donor surface states with downward band bending.[196-197] However, both upward and downward band bending has been reported for bulk and nanostructured ZnO despite being a naturally n-type semiconductor.[196-200] This behaviour has been attributed to variation in the type and density of native defects on the ZnO surface which affects the adsorption efficiency of different ambient gas species.[143, 197-208] To understand these gas - surface mechanisms in detail, ZnO nanorod surfaces have been modified using controlled atmosphere annealing techniques by design to produce surfaces with different distributions of native point defect.[202, 209-214] A range of complementary spectroscopy techniques have been used to investigate interactions between native ZnO point defects and ambient gas species to establish their effect on the surface optical and electrical properties of ZnO nanorods.

5.3 Experimental section

ZnO nanorods were grown hydrothermally at 90°C for 3 hours in a seed aqueous mixture containing 0.025 M zinc nitrate hexahydrate ($Zn(NO_3)_2$ $6H_2O$, 98% purity) and 0.025 M hexamethylenetetramine ($C_6H_{12}N_4$, ≥ 99.0% purity). Nucleation of ZnO nanorods was achieved by applying a few drops of zinc acetate solution (5mM in ethanol) on a sapphire substrate, which was then baked at 250°C for 20 minutes. The hydrothermal synthesis parameters were chosen so that the nanorods elongated over a range of angles with respect to the substrate normal to promote contact of the sidewall surfaces, leading to good electrical conductivity across the entire nanorod ensemble. The as-grown samples were annealed at 650°C for 30 minutes in O_2 and in Zn vapor to produce samples with three different surface electronic structures. The morphology of

ZnO nanorods was not changed by the post-growth heat treatment. The size and shape as well as the crystal structure of as-grown and annealed ZnO nanorods were characterized using field-emission scanning electron microscopy (FE-SEM) and powder X-ray diffraction (XRD) respectively.

Electrical I-V curve measurements were conducted using a 6157A electrometer (Keithley Co, Ltd). Aluminum electrodes consisting of pattern of 12 interdigitated fingers 900 μm length with 100 μm spacing, were deposited onto the surface ZnO nanorod ensemble using a thermal evaporation technique.

Cathodoluminescence (CL) spectra were measured using a FEI Quanta 200 scanning electron microscope equipped with a retractable diamond machined parabolic mirror light collector and a liquid nitrogen (80 K) cold stage. CL spectra were collected using an Ocean Optics QE6500 optical spectrometer 300-1000 nm with a spectral resolution of 0.9 nm. In all CL measurements, the accelerating voltage of the electron beam was 5 kV, corresponding to a maximum CL generation depth of around 37 nm. All CL spectra were corrected for the total response of the light collection system.

X-ray photoemission spectroscopy (XPS) and X-ray Absorption Near-Edge Structure (XANES) were performed on the soft X-ray spectroscopy beamline at the Australian Synchrotron. In photoemission experiments, the energy of incident X-ray photon was adjusted to achieve a similar photoelectron kinetic energy with a ~ 3 nm probing depth. The O1s spectra were acquired at hv = 650 eV, while the valence band spectra were acquired at hv = 150 eV. XANES was implemented in the Total Fluorescence Yield (TFY) mode around the O K-edge. The photon energy scale was calibrated against the Au $4f_{7/2}$ peak at 84 eV from a clean gold film in electrical contact with the samples. For each measurement, several scans were registered on the same spot in order to monitor x-ray beam damage; no significant changes within the measurement time (approximately 10 minutes) were detected.

Electron Spin Resonance (ESR) analysis was carried out at 10 K using a Bruker Elexys E500 cw X-band ESR spectrometer equipped with an Oxford ITC605 temperature controller. All presented ESR spectra were measured using a power of 2.0 mW at a frequency of 9.4 GHz and modulation amplitude of 5.0 G.

The photoluminescence (PL) spectra were recorded using a home-built confocal microscope with 500 nm resolution. Optical excitation was implemented using

continuous-wave blue (λ = 405 nm) and green (λ = 532 nm) lasers through a high numerical aperture (NA = 0.9) objective. The PL signal was collected using the same objective and sent to a Princeton Instruments, 300 lines/nm grating spectrometer. The PL signal was measured using an Excelitas SPCM-AQRH-14Avalanche Photo Diode. A dichoric mirror was used in all measurements to filter out the laser excitation emission, and a band-pass filter was employed to select only the defect emission. The measurements were done at room temperature and were corrected for system response.

5.4 Results and discussion

The 90°C hydrothermal growth technique yielded a continuous high-density layer of uniform ZnO nanorods which exhibit a highly regular hexagonal cross-section with a diameter and length of 55 ±5 nm and around 2000 nm respectively (Figure 5.1). X-ray diffraction analysis (Figure 4.1(b)) confirmed that the nanorods are high quality hexagonal wurtzite single crystals and that their growth axis is along the <0001> direction.
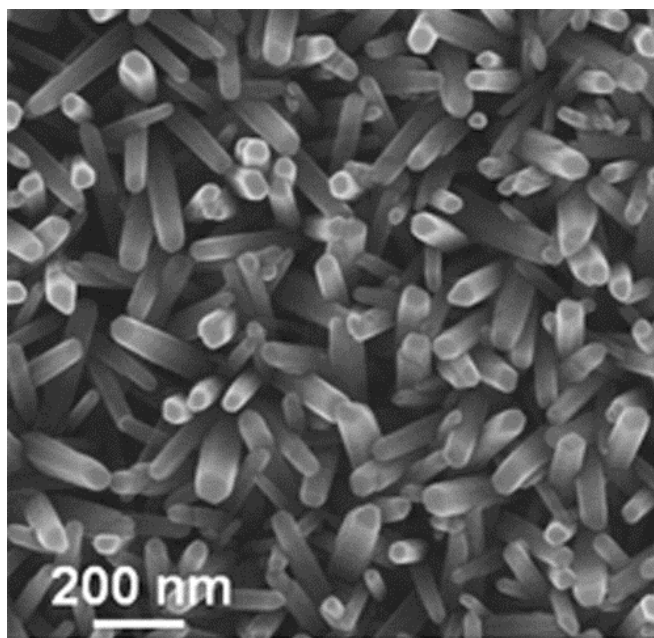
Figure 5.1 shows SEM images of the as-grown hydrothermal ZnO nanorod ensemble containing a high density of uniform hexagonal <0001> nanorods 50 ± 5 nm in diameter. The oblique nanorod growth habit promotes multiple contact of the sidewalls providing good electrical conductivity across the ensemble.

Typical low voltage CL spectra at 80 K are presented in Figure 5.2. The CL peak at 3.37eV results from the ZnO near band edge (NBE) emission, containing highly overlapped peaks from free exciton recombination and its associated phonon replicas.[32] Deep level emission bands in the yellow (YL) at 1.90 eV, red (RL) at 1.70 eV and green at 2.43 eV are observed in the as-grown, O_2 and Zn vapor annealed nanorods respectively. These broad CL peaks has been attributed in the literature to different types of intrinsic defect centers: YL - oxygen interstitials (O_i) and Li_{Zn} acceptors,[55, 79-80, 83, 215] RL - zinc vacancies (V_{Zn})[79, 82, 178, 180] and GL - oxygen and zinc vacancies V_O[40, 182-183, 216]. The low voltage CL measurements shown in Figure 5.2 confirm that each of the three separate nanorod samples, as-grown, O_2 and Zn vapor anneal, exhibit significantly different surface defect structures. The appearance of the LO-phonon replica peaks on the low energy side of the NBE indicates that the crystal quality of ZnO nanorods was improved by the annealing process. This is also evidenced by the blue shift in the as-grown NBE due to a decrease in carrier concentration due to the thermal removal of inadvertently incorporated shallow donors, most likely hydrogen.[217]
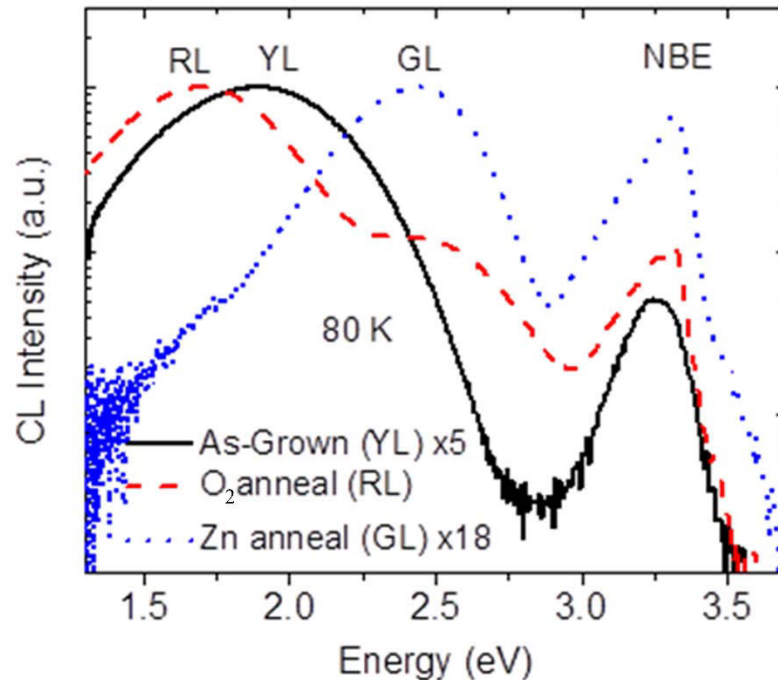
Figure 5.2 Typical 5 kV CL spectra collected from as-grown, O_2 atmosphere and Zn vapor annealed ZnO nanorods at 80K, a scan area = 50 μm x 43 μm and beam current of 0.2±0.02nA, showing yellow (YL) at 1.90 eV, green (YL) at 2.44 eV and red (RL) at 1.70 eV.

Differences in the surface defect structure are also evidenced by the I-V results (Figure. 4.3(b)) which reveal large changes in the surface conductivity between the three sample types. The low current observed in the as-grown samples arises from the chemisorption of oxygen molecules which capture electrons forming charged oxygen species (O_2^-) and creating a resistive surface depletion layer.[202, 204-206] After annealing in Zn vapor a three orders of magnitude increase in the measured I-V current was observed (Figure 5.3). This result is consistent with a high surface coverage of water molecules and hydroxyl groups that release electrons to the ZnO nanorod surface producing and electron accumulation layer, increasing the electrical conductivity.[202, 204, 218-220] Here *chemisorbed* and physisorbed ambient water molecules efficiently bond and dissociate on Zn sites at surface oxygen vacancies[218] which renders the ZnO nanorod surface hydrophilic. Lastly the O_2 annealed nanorods produced a two orders of magnitude current increase from the as-grown result due to the change in the type and density of surface defect gas adsorption sites. This result emphasizes the effect of the competitive nature of the oxygen and water vapor surface adsorption and its dependence on the surface defect chemistry.
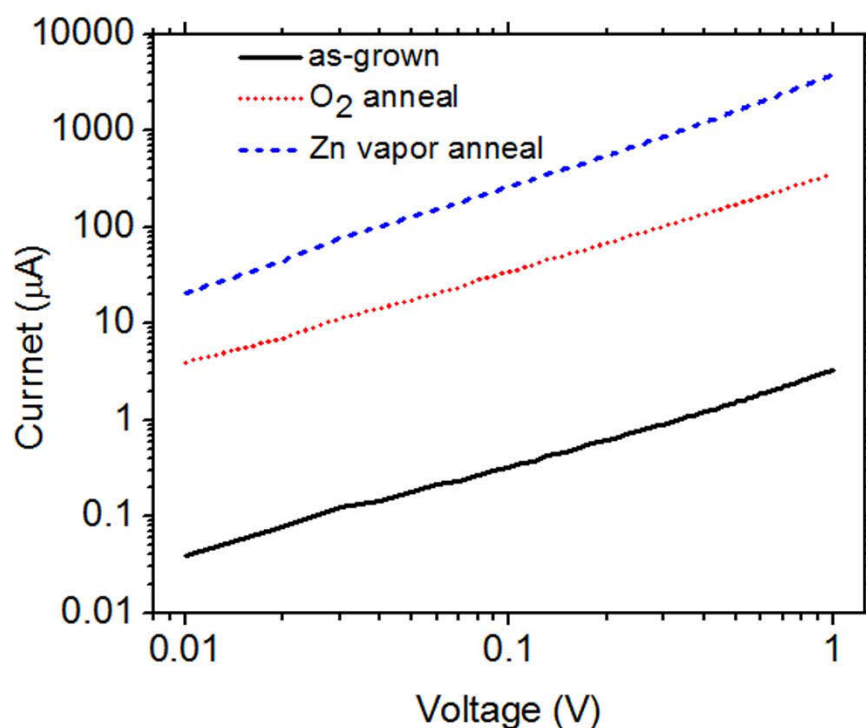
Figure 5.3 presents a log I vs log V showing the 1000x and 100x increase in the measured current after Zn vapor and O_2 annealing respectively.
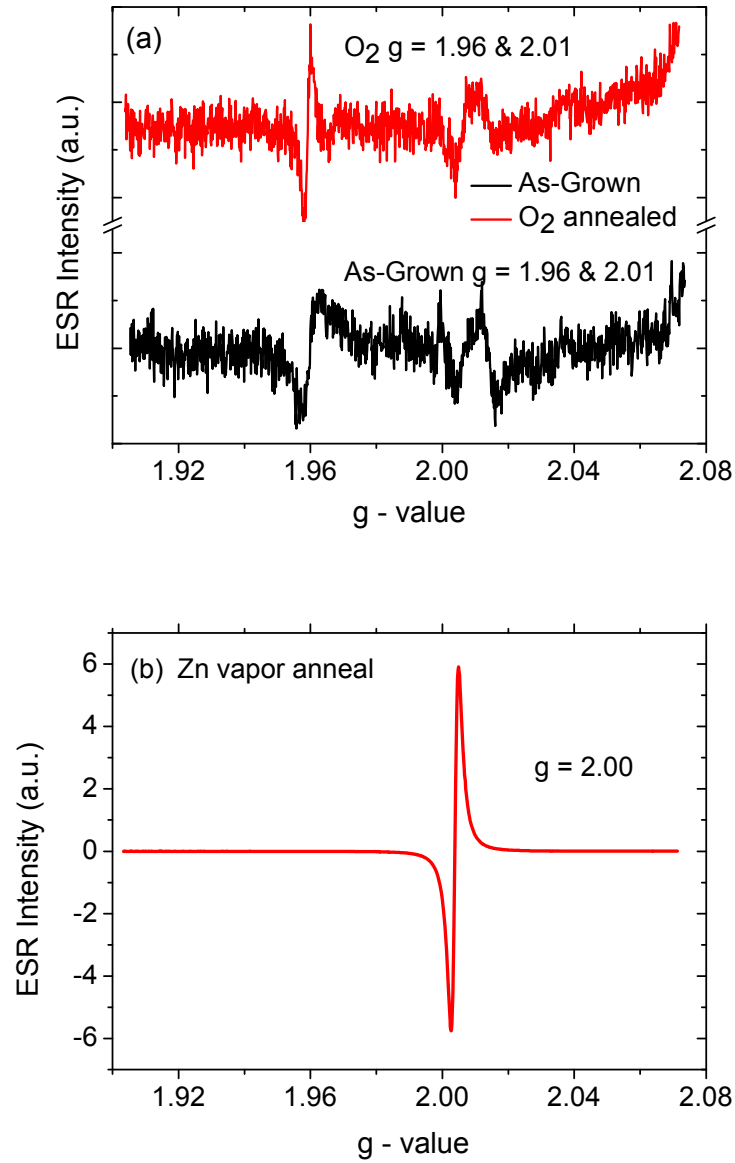
Figure 5.4 (a) ESR spectra of the as-grown and O_2 annealed ZnO nanorods. Two main paramagnetic ESR signals at $g \cong 2.01$ and 1.96 are assigned to singly ionized surface oxygen vacancy defects and localized donors, respectively. (b) ESR spectrum following Zn vapor annealing showing a significant intensity increase is $g \cong 2.00$ line after the appearance of a broad green CL emission centered at 2.44 eV and a pronounced shoulder in the valence band photoemission spectrum ~ 3 eV below the Fermi level.

ESR spectroscopy of the as-grown nanorods revealed weak signals at $g = 1.96$ and $g = 2.01$ (Figure. 5.4(a) and 5.4(b)). Both these ESR lines became slightly

sharper following annealing in O_2 with no significant increase in intensity most likely due to an increase in the mean spin-spin separation following the thermal enhancement in the crystal quality.[221] The g = 1.96 signal has been attributed to a number of different point defects in ZnO, including zinc interstitials (Zn_i^{2+}),[222] oxygen interstitials (O_i^-)[223] and zinc vacancies (V_{Zn}^-)[223] as well as conduction band states related to shallow donor impurities, such as H[224] and Ga, In and Al.[225] Centers involving Zn_i^{2+} and H can be ruled out as these defects have high thermal mobilities in ZnO.[226-227] Consequently in ZnO nanostructures Zn_i^{2+} and H should easily diffuse to the surface and expelled during high temperature heat treatment. Furthermore since there was no change in the intensity of g = 1.96 with O_2 annealing O_i^- and V_{Zn}^- can be excluded as well leaving Ga, In and Al shallow donor impurities as the most likely chemical origin of the g = 1.96 ESR line.

The weak g $\cong$ 2.01 signal has been attributed to singly ionized surface oxygen vacancies V_o^+ in photo-ionization experiments,[228] however, its assignment remains controversial. In this work it was found that the intensity of the ESR line around g $\cong$ 2.02 increased significantly after the ZnO nanorods were annealed in Zn vapor (Figure 5.4(b)). This result provides compelling support for the assignment of the g = 2.02 line to surface V_o^+ since it is expected that Zn_{vap} annealing will cause strong gas-solid surface reduction reactions that create oxygen vacancies as substantiated by the presence of strong GL band in the CL analysis (Figure 5.2). Although the V_o^+ is theoretically predicted to spontaneously transform to either a doubly ionized V_o^{2+} center or a neutral V_o^O by either emitting or capturing an electron respectively,[40] the correlative surface characterization results in this work strongly suggest that V_o^+ center is energetically stable at the surface of ZnO nanorods.

The O1s XPS spectra for RL, GL and YL ZnO nanorod samples presented in Figure 5.5. These XPS data were all curve fitted into three peaks using a pseudo-Voigt function with a consistent set of peak position and FWHM curve fitting parameters at 530.5 eV (Peak O_I), 532.0 eV (Peak O_{II}) and 532.7 eV (Peak O_{III}). Peak O_I is ascribed to O^{2-} ions surrounded by fully co-ordinated by Zn and O atoms in the fully stoichiometric wurtzite crystal structure, peak O_{II} is related to either O^{2-} ions in the vicinity of V_O defects or OH groups and peak O_{III} is attributed to oxygen in strongly bound adsorbed gases, specifically H_2O and O_2 molecules.[188, 229-232] The relative

percentage for each of these three peaks for the as-grown, Zn annealed and O_2 annealed specimens are as follows: as-grown O_I – 31%, O_{II} 41% and O_{III} 28%; O_2 anneal O_I – 38%, O_{II} 38% and O_{III} 24%; and Zn vapour anneal - O_I – 18%, O_{II} 51% and O_{III} 31% (as shown in table 5.1).
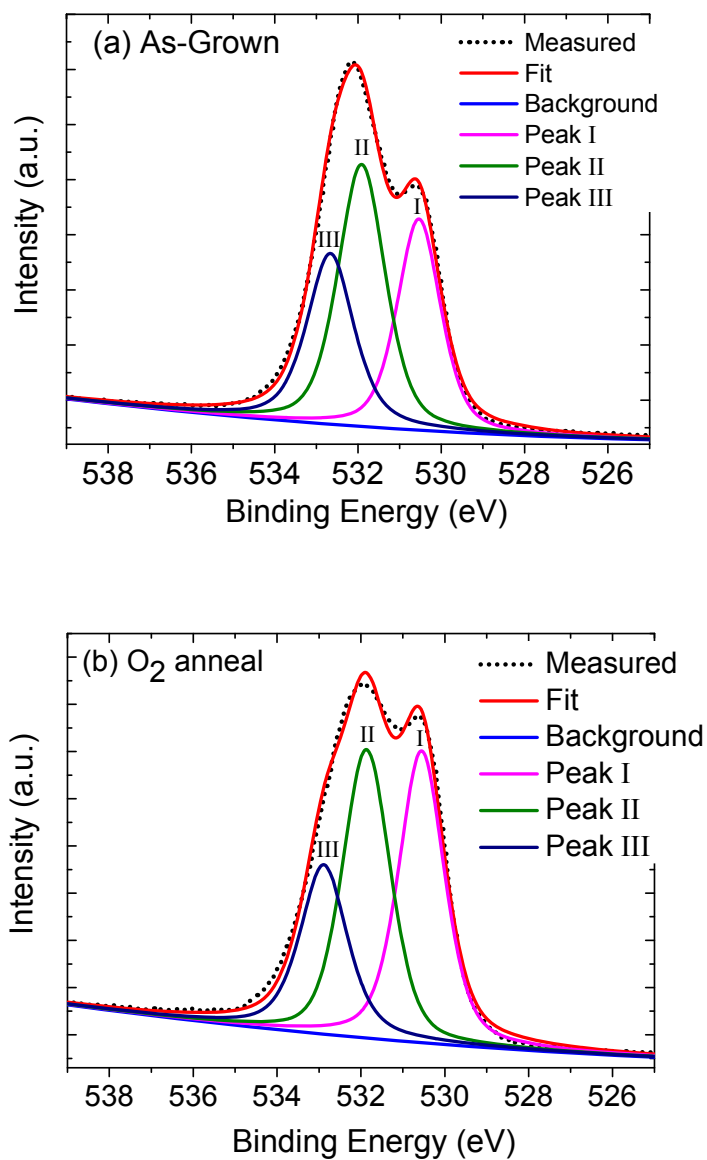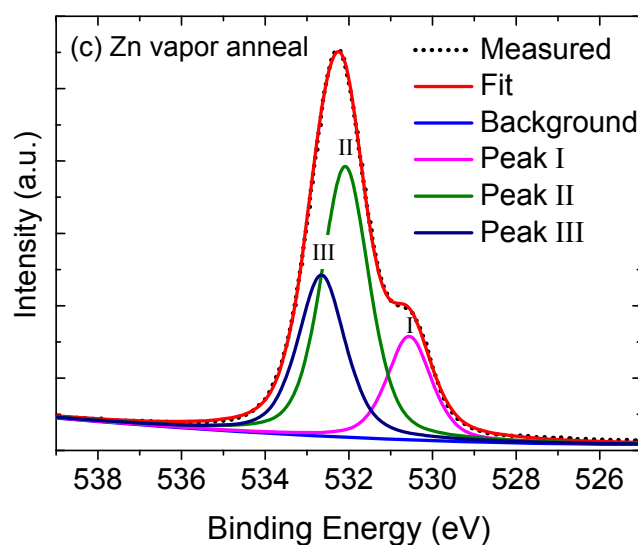
Figure 5.5 The O1s XPS spectra for YL, RL and GL ZnO nanorod samples are shown in Figures 5.5(a), 5.5(b) and 5.5(c) respectively. The XPS profiles are all curve fitted into three peaks at 530.5 eV (Peak O_I), 532.0 eV (Peak O_{II}) and 532.7 eV (Peak O_{III}). Peak O_I results from O^{2-} ions fully co-ordinated by Zn and O atoms in the fully stoichiometric wurtzite crystal structure, peak O_{II} is due to either O^{2-} ions in the vicinity of V_O defects and peak O_{III} arises from oxygen in strongly bound adsorbed gases, specifically H_2O and O_2 molecules.

Table 5.1 The relative percentage of the integrated intensity of the O_I, O_{II} and O_{III} peaks from the O1s XPS emission for the as-grown, Zn annealed and O_2 annealed specimens.

	Peak O_I Crystalline ZnO	Peak O_{II} O Vacancies	Peak O_{III} Absorbed Gas
As grown	31%	41%	28%
O_2 anneal	38%	38%	24%
Zn anneal	18%	51%	31%

The XPS results show that annealing in O_2 leads an increase in fully coordinated oxygen and stoichiometry (peak O_I) with a corresponding decrease in the concentration of oxygen vacancies $[V_O]$ (peak O_{II}). While annealing in Zn vapor increases the $[V_O]$ from 30% to 50%. This direct correlation between the O_I and O_{II} fractions is in agreement with their relationship to the degree of stoichiometry of the O^{2-} ions or more specifically the density of oxygen vacancies and is consistent with the ESR and CL findings unequivocally confirming the presence of surface V_O centers. These data also strongly suggest that in our ZnO nanorods the O_{II} peak is related to V_O defects rather than adsorbed surface OH groups. The ratio between the O_{III} / O_{II} percentages is around ~0.6 for all three samples indicating that the amount of the adsorbed gas species (O_{III}) is directly proportional to the surface V_o concentration and that these centers play an important role in surface gas adsorption as suggested by in other theoretical and experimental work.[189, 207, 218]

Valence band X-ray Photoemission Spectroscopy (VB-XPS) spectra taken from the ZnO nanorod samples are presented in Figure 5.6(a). The VB-XPS spectra for all three samples consist of two dominant near edge peaks one centered at ~ 5 eV ascribed to O 2p related states the other ~ 7 eV attributed to hybridized Zn 4s + O 2p states.[233-236] The Zn 3d peak is located ~13 eV at its signature position for wurtzite ZnO. Using the VB-XPS spectra, the magnitude of surface band bending, V_{BB}, can be determined using the following relationship:

$$V_{bb} = E_g - E_{BEcutoff} - E_{CF}$$

where E_g is the ZnO band gap (= 3.37 eV) and E_{CF} is the energy difference between the Fermi level and the conduction band with $E_{CF} = \frac{k_b T}{e} \ln \left[\frac{N_c}{n_e} \right]$, N_c is the conduction band effective density of states [= 2.94×10^{18} cm^{-3} for $m_e^* = 0.24\, m_e$], n_e is the bulk carrier density and e, T and k_b all have their usual meaning. The $E_{BEcutoff}$ was found using the intersection of extrapolated linear fits to the leading edge of valence band photoemission and the photoemission background as shown in Figure 5.6(b). Using typically reported literature values for the electron density in ZnO nanowires, n_e = ~ 1 x 10^{17} cm^{-3},[237] surface band bending values of - 0.42 ± 0.02V and - 0.24 ± 0.02V for the as-grown and O_2 annealed samples respectively. These negative values indicate downward band bending due to surface electron accumulation on the ZnO nanorod, which is attributed

to adsorbed water molecules and hydroxyl groups (Figure. 5.7.). Less downward band bending after O_2 annealing indicates a smaller amount of negative charge transfer to the surface by a reduced number of adsorbed water molecules and hydroxyl groups on the ZnO nanorods due to the change in the surface defect chemistry.

Thermally induced changes in n_e during O_2 annealing can be dismissed because heating at elevated temperatures should produce a reduction in n_e either through the loss of H or Zn_i donors because of their high mobility or via the formation of compensating acceptor defects. Both these processes would cause a corresponding increase in the degree of band bending rather than a decrease. Given this, the decrease in negative band bending after O_2 annealing is attributed to a reduction in the number of adsorbed water and hydroxyl donors as established with the I-V results. However, it is important to note that the I-V data was collected under ambient conditions with both physisorbed and chemisorbed molecules on the ZnO nanorods whereas the XPS measurements are taken under ultra high vacuum conditions were physisorbed species are pumped away leaving strongly bound chemisorbed species.

Heating in zinc vapor produced a strong shoulder feature in the VB-XPS spectra around ~ 3eV below the E_F with a shift of the VB photoemission onset to ~ 1 eV below the E_F (Figure. 5.6(b)). These results together with the corresponding CL data showing strong GL as well as the ESR results and the O 1s XPS data unequivocally confirm the presence of electron populated surface oxygen vacancy states above the valence band following Zn vapor annealing. The corresponding strong ESR signal indicates that these centers must be paramagnetic singly ionized surface oxygen vacancies. The presence of surface oxygen vacancies is also supported by the observed broadening of the O 2p + 4 s and O 2p states due to lattice disordering (Figure. 5.6(b)).
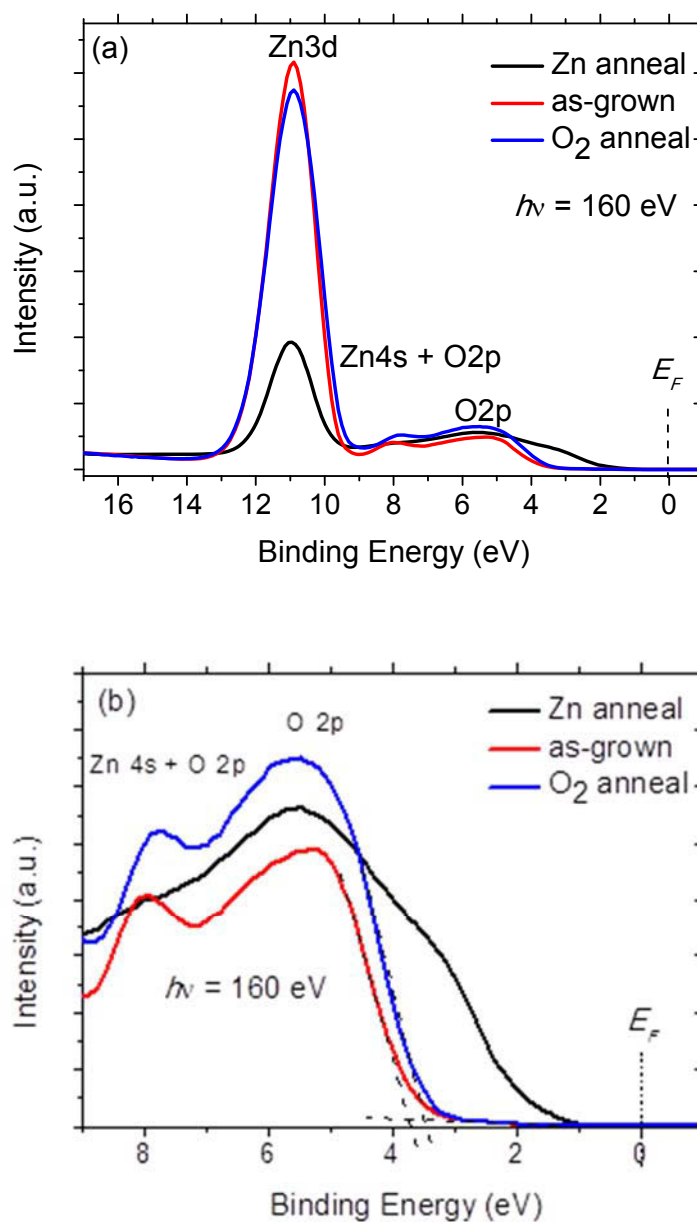
Figure 5.6 Valence band X-ray Photoemission Spectroscopy (VB-XPS) spectra taken from the as-grown, O_2 anneal and Zn vapor anneal ZnO nanorod samples are presented in Figure. 5.6(a). The VB-XPS spectra for all three samples consist of two dominant near edge peaks one centered at ~ 5 eV ascribed to O 2p related states the other ~ 7 eV attributed to hybridized Zn 4s + O 2p states. The leading edge of the valence band photoemission showing the pronounced shoulder around 3 eV below the Fermi level that forms after Zn vapour annealing is shown in Figure 5.6(b).
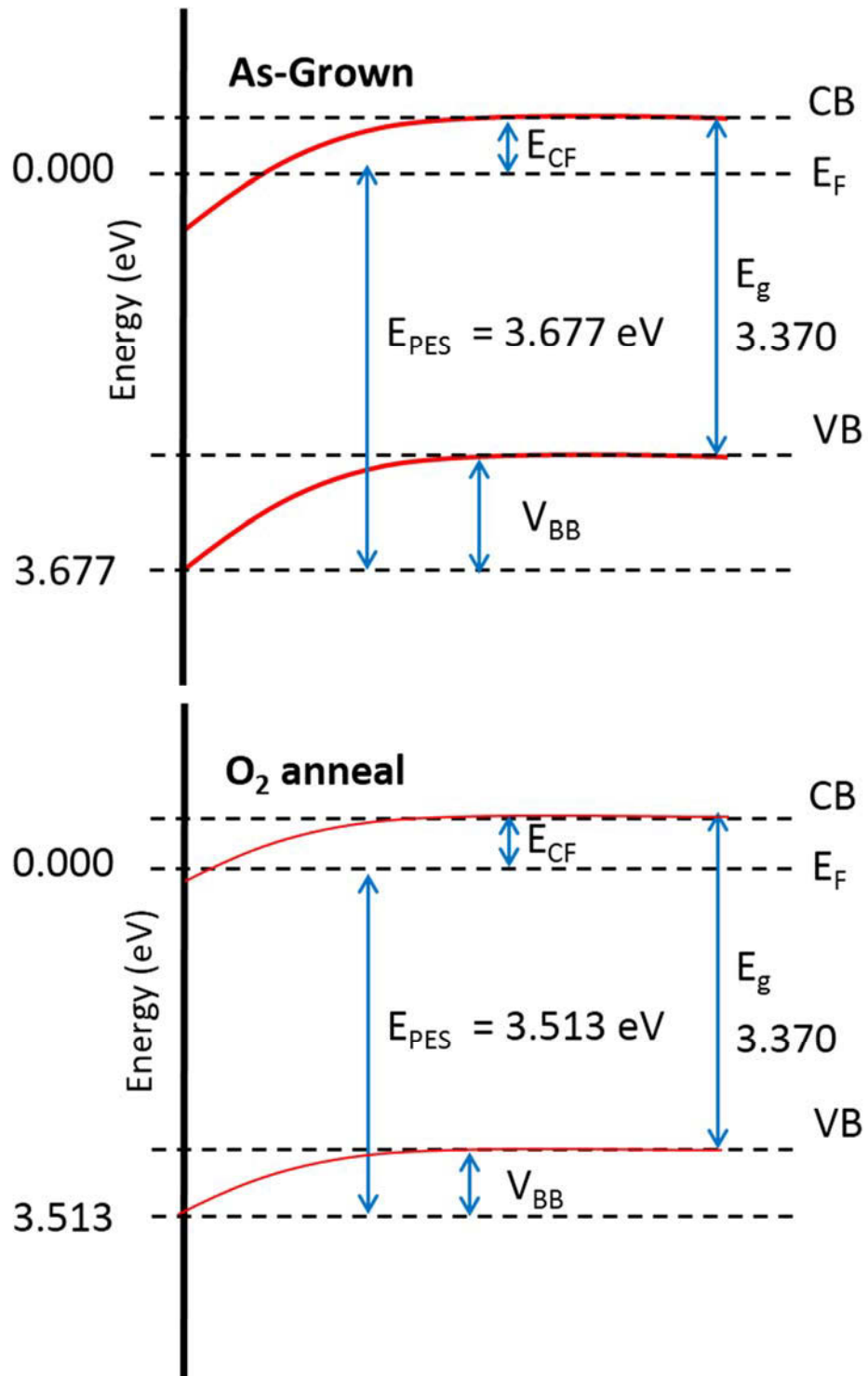
Figure 5.7 Downward band bending on the as-grown ZnO nanorod due to electron accumulation and its decrease following O_2 annealing using the valence band photoemission spectroscopy results in Figure 5.6 (a) and 5.6 (b).
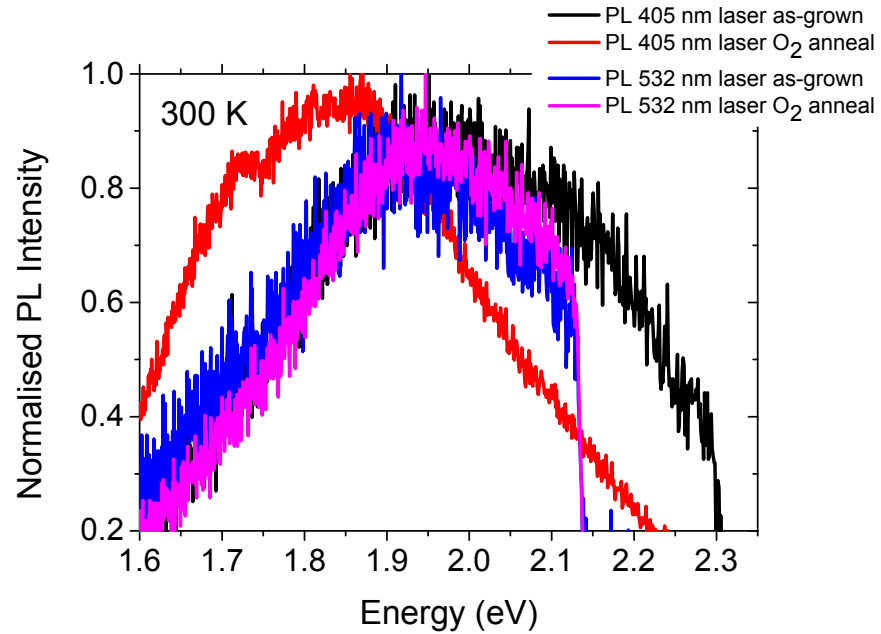
Figure 5.8 Comparison of continuous-wave 532 and 405 nm sub band gap laser excitation PL spectra at 300 K for ZnO nanorods as-grown and annealed in O_2 gas. The sub band gap excited spectra reveal a common broad OL emission at 1.95 eV except for the O_2 annealed sample illuminated with blue light which emits a broad RL around 1.83 eV indicated a different defect structure.

Finally sub-band gap excitation photoluminescence spectroscopy using both a blue (3.06 eV) and green laser (2.39 eV) was employed to establish if there were any additional defect structure differences between the as-grown and O_2 annealed ZnO nanorods. This technique enables the detection of defect centers that not usually accessible with CL and above band gap PL excitation because of the presence of more efficient recombination channels. Bulk defects can be probed as well. These sub-band gap generated PL emission peaks are attributed to both excitation and radiative relaxation of (i) electrons in ionized acceptor centers and (ii) valence band electrons to shallow donor states[178, 180] Normalized PL spectra at 300 K excited using blue and green laser light from the as-grown and O_2 annealed ZnO nanorods are shown in Figure. 5.8. A broad orange emission band positioned at 1.95 eV (OL) is observed in as-grown ZnO nanorods with both laser excitation sources. Green laser light illumination produced an identical OL in the O_2 annealed sample, however, the higher energy blue laser excited a broad red emission centered around 1.83 eV comprised of a number of broad emission

peaks. Although it is highly likely that the RL and OL sub band gap emission bands relate to native acceptor centers involving V_{Zn} or O_i defects respectively, the assignment of these PL peaks to specific defects requires further work. Nevertheless, the sub-band gap laser PL results confirm that O_2 annealing changes the defect structure of the ZnO nanorods through the formation surface V_{Zn} related centers. The presence of these centers could account for the observed decrease in the magnitude of negative band bending.

5.5 Conclusions

Optical and electrical characterization studies of ZnO nanorods before and after annealing in O_2 gas and Zn vapor have confirmed that the surface electronic structure can be bespoke for specific sensor applications. These correlative spectroscopy measurements reveal clear evidence of direct interrelationship between the electronic properties of the ZnO nanorod surface and its surface defect structure. In particular, the role of intrinsic point defects on the physisorption and chemisorption of water molecules and hydroxyl groups which, through charge transfer mechanisms, govern both the surface band bending effects and the surface conductivity. Additionally O1s XPS spectra established that the number of adsorbed water and hydroxyl species on the ZnO nanorod is directly proportional to the concentration of surface oxygen vacancies. An important result of these studies is compelling experimental evidence for the existence of stable singly ionized oxygen vacancies (V_O^+) at the ZnO nanorod surface. Furthermore, it was shown that (i) a broad green CL peak centered at 2.43 eV, (ii) an intense ESR line at g $\cong 2.01$ and (iii) a pronounced shoulder in the valence band X-ray photoemission spectra ~ 3.0 eV below the Fermi level, can all be attributed to centers involving surface V_O^+ centers.

CHAPTER VI

NATURE OF RED LUMINESCENCE IN OXYGEN TREATED HYDROTHERMALLY GROWN ZINC OXIDE NANORODS

6.1 Summary

A strong broad red luminescence (RL) peak centered at 1.69 eV (FWHM = 0.57 eV) at 15K [1.78 eV (FWHM = 0.69 eV) at 300 K] is formed in ZnO nanorods hydrothermally grown at low temperature following thermal annealing at 650°C for 30 minutes in an O_2 gas environment. The optical properties of this peak were comprehensively studied using a range of characterization techniques, including photoluminescence and cathodoluminescence spectroscopy, X-ray absorption near edge spectroscopy and electron paramagnetic resonance spectroscopy. With decreasing temperature the RL peak position red shifted and its FWHM became narrower in accordance with the configuration coordinate model. Using these results, the RL has been assigned to highly lattice coupled V_{Zn}-related acceptor-like centers. No correlation was found between the observed red luminescence and nitrogen impurities.

6.2 Introduction

Of particular importance is the luminescence of ZnO with optical emission that spans the ultra-violet, visible and near infrared spectral range. In the ultra-violet the emission is dominated by radiative near band edge (NBE) recombination mechanisms including, free and bound excitons as well as free-to-bound and donor acceptor pair transitions involving shallow defects. While deep level defects produce broad emission peaks via a variety of recombination and internal mechanisms in the green (~2.5 eV and 2.3 eV) [181-183, 216], yellow (~2.1 eV) [55, 79, 83], orange (~1.9 eV) [80] and red (1.7 eV) [79, 82, 178] at 300 K.

Despite considerable research effort unequivocal assignment of these luminescence peaks to specific dopants, impurities as well as defects and their

complexes has not been realized up to now. Nevertheless there is general agreement that oxygen (V_O) and zinc (V_{Zn}) vacancies and interstitials (O_i and Zn_i) play a major role in these luminescence processes in undoped ZnO. To date most optical characterisation studies have focused on the green luminescence and to a lesser extent the yellow and orange emission in ZnO. However, there is currently growing interest in the red luminescence (RL) for a number of reasons. First it has been recently suggested that the RL could be a signature emission for N acceptors in ZnO [13] which is of importance to the development of stable p-type material. However, RL has also been attributed to zinc vacancies (V_{Zn}) [79, 180], oxygen interstitials (O_i) [80, 82], oxygen vacancies (V_O) [238] as well as the Zn_i-V_O complex or $V_{Zn}V_O$ di-vacancies.[88] Second gas sensor studies have revealed a significant enhancement in the electrical sensitivity of the ZnO surface to specific target gases, such as NH_3, when RL dominates the luminescence spectrum.[113] Finally the second-order correlation [$g^2(0)$=0.1] of photons in the red-orange spectral range confirming single photon emission in ZnO has been recently reported.[215, 239]

In this work the temperature and power density dependence of the RL in ZnO have been systematically investigated using cathodoluminescence spectroscopy. These data have been compared to ESR and photoluminescence NBE spectroscopy results as well as ESR and XANES data. Collectively these correlative studies indicate that the RL is associated with highly lattice coupled V_{Zn}-related acceptor –like radiative recombination centers.

6.3 Samples and Experiments

6.3.1 Fabrication and Post Growth Processing of ZnO Nanorods

Zinc acetate solution (5mM in ethanol) was dropped on a silicon wafer to induce ZnO nucleation and then baked at 250°C in air for 20 minutes. ZnO nanorods were grown using a hydrothermal treatment by placing the nucleated substrates in seed aqueous mixture containing 0.025 M zinc nitrate hexahydrate and 0.025 M hexamethylenetetramine at 90°C for 3 hours.[175-176] Analytical reagent grade zinc acetate dihydrate (>98%, $(C_2H_3O_2)_2Zn\cdot 2H_2O$), zinc nitrate hexahydrate, (98%, $Zn(NO_3)_2$ $6H_2O$), and hexamethylenetetramine (HMT, ≥99.0%, $C_6H_{12}N_4$) from Aldrich

were employed as received with no further purification. The as-grown nanorod samples were annealed at 650°C for 30 minutes in O_2 gas environment. Hydrogen plasma treatment was conducted at a sample temperature of 100 °C using a mild 10 W hydrogen radio-frequency plasma for 20 minutes with 10 sccm H_2 flow rate.

6.3.2 Characterization of hydrothermally grown ZnO Nanorods

6.3.2.1 Cathodoluminescence

The cathodoluminescence (CL) spectra were collected using a FEI Quanta 200 scanning electron microscope equipped with the option of either an Ocean Optics QE6500 system or a Hamamatsu S7011-1007 CCD sensor. The Ocean Optics QE65000 system provides CL collection from 300-1000 nm with a spectral resolution of 0.9 nm. CL was collected by a diamond machined parabolic mirror positioned above the sample with an aperture to facilitate transmission of the electron beam. In temperature resolved experiments, the sample was placed on a liquid helium cold stage with the temperature varying from approximately12 K to 300 K. In all CL experiments, the accelerating voltage of the electron beam was 5 kV which corresponds to a maximum photon generation depth of around 37 nm.[177] The electron beam current was varied from around 0.013 nA to 2.54 nA in power-density measurements. All CL spectra were corrected for the total response of the light collection system

6.3.2.2 Photoluminescence

High resolution PL was done utilizing the fourth harmonic generation (266 nm) of a Nd:YAG laser. A monochromator with a 1200 lines/mm grating (spectral resolution 0.2 meV) was used to disperse the emitted light. In temperature resolved experiments, the PL measurements were performed in a liquid helium bath cryostat allowing measurements from 7K to 300 K. A HeCd Laser with the 325 nm emission line and an output power of 36 mW was used to excite the ZnO samples above the band gap. The emitted light was dispersed by a Spex-1404 double monochromator (spectral resolution 50 μeV) and detected by a bi-alkali photodetector.

6.3.2.3 X-Ray Absorption Near Edge Spectroscopy (XANES)

Total Fluorescence Yield (TFY) and Total Electron Yield (TEY) mode XANES analysis were performed around the N *K*-edge on the soft X-ray Spectroscopy beamline at the Australian Synchrotron. The incident X-ray beam was linearly polarized and perpendicular to the substrate surface. The photon energy scale was calibrated against the Au $4f_{7/2}$ peak at 84 eV from a clean gold film in electrical contact with samples.

6.3.2.4 Electron Spin Resonance

The ESR spectra were collected using a Bruker Elexys E500 cw X-band ESR spectrometer equipped with an Oxford ITC605 temperature controller. All presented ESR spectra were measured at 10 K using a power of 2.0 mW at a frequency of 9.4 GHz and modulation amplitude of 5.0 G.

6.4 Results and Discussion

The low temperature 90 °C hydrothermal growth technique produced a continuous high density film of ZnO nanorods approximately 55 nm in diameter and 2000 nm in length (Figure 6.1). XRD analysis (Figure 4.1(b)) confirmed that the ZnO nanorods have a hexagonal wurtzite structure (P63mc) with lattice constants of $a = 0.3249$ nm and $c = 0.5207$ nm and that their longitudinal axis was normal to the c-plane. The <0001> ZnO nanorod ensemble are oriented at various angles to the normal direction of the substrate plane. No change in the crystal structure, morphology or orientation of the ZnO nanorods was observed after annealing at 650 ºC in either O_2 or Ar.
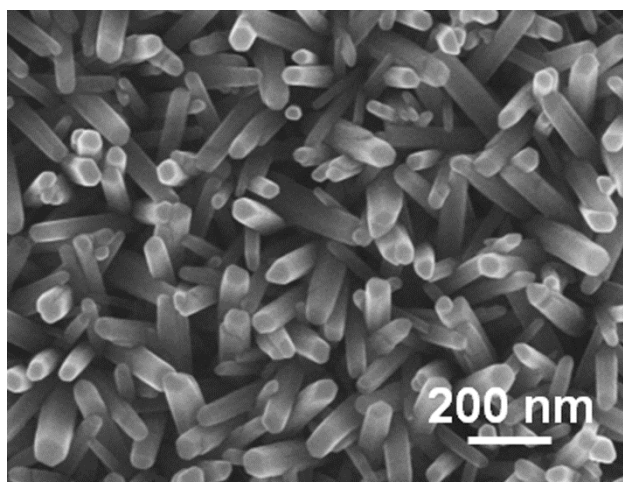
Figure 6.1: SEM image of the as-grown <0001> ZnO nanorod ensemble, showing that the low temperature hydrothermal growth treatment produced a high density of uniform hexagonal <0001> nanorods approximately 55 nm in diameter orientated at different angles to the normal direction of the substrate.

Figure 6.2a shows before and after annealing CL spectra at 300 K from the "as-grown" and O_2 heat treated nanorod films. The "as-grown" sample exhibits a ultra-violet peak centered at 3.17 eV arising from a number of highly overlapped thermally broadened LO-phonon replicas of the free exciton (FX) emission. A broad orange peak positioned at 1.99 eV is also observed in the as-grown nanorods which has been previously attributed to Li acceptors [240] and O_i related centers [215]. After annealing in O_2 at 900 °C the NBE emission increases in intensity by a factor of 5 due to a thermally induced improvement in the quality of the ZnO nanorods following a reduction in the number of point and extended defects that provide non-radiative recombination pathways. Additionally and more significantly the O_2 heat treatment created a strong, highly symmetric red luminescence at 1.78 eV and FWHM of 0.69 eV. Figure 6.2b shows that this emission was found to rapidly quench following exposure to a mild H_2 plasma strongly suggesting that the chemical origin of the RL is related to acceptor-like centers as hydrogen is a well-known donor in ZnO. The accompanying large increase in the NBE could indicate that the RL centre acts as an efficient competitive recombination channel to the NBE, however, further H passivation of non-radiative pathways cannot be ruled out. At 15 K the RL peak position, see Figure 6.2c, slightly red shifts to 1.69 eV and the FWHM narrows to 0.57 eV, which can be interpreted by a

configurational coordinate (CC) model [241]. Furthermore the absence of any fine structure in the peak at 15 K eliminates the assignment of the observed RL to transition metal impurities, such as Fe, Co and Ni, which exhibit characteristic sharp features due to internal 3d transitions [242-243]. The presence of a broad emission at 2.5 eV has been attributed to surface and bulk V_O centers at 5 K [179, 215]. In addition at 15 K the NBE blue shifts revealing a structured UV emission at 3.31 eV. This peak and its phonon replicas have been attributed to acceptors in ZnO involved in donor acceptor pairs and free-to-bound acceptor transitions as well as to excitons bound to structural or surface or defects. [244-245]

CL spectra as a function of electron beam excitation current at 80 K and 300 K normalized at the maximum of the RL peak are shown in Figure 6.3a and 6.3b respectively. The RL does not exhibit a blue shift with increasing power-density a typical hallmark characteristic of the donor acceptor pair (DAP) recombination mechanism. The CL intensity versus electron beam current displays a power-law dependence on beam current with $I_{CL} \propto I_B^n$. Log (I_{CL}) versus log (I_b) plots at 300 K using the data in Figure 6.4a and 6.4b provide power law exponent: $n_{RL} = 0.74 \pm 0.03$ and $n_{NBE} = 1.22 \pm 0.04$ at 80 K, and $n_{RL} = 0.81 \pm 0.02$ and $n_{NBE} = 1.08 \pm 0.09$ at 300 K.

The linear excitation power dependence of the NBE is expected as the excitonic recombination rate is faster than the carrier injection rate by the energetic electron beam. The n_{RL} values are larger than expected for typical phonon-coupled defect transitions which are typically around n ~ 0.5 because of the longer radiative relaxation times. However, the slightly high n value of the RL could possibly be explained by either a high RL defect concentration or possibly increased RL emission due to excitation via an energy exchange mechanism involving the relaxation of free excitons [240].
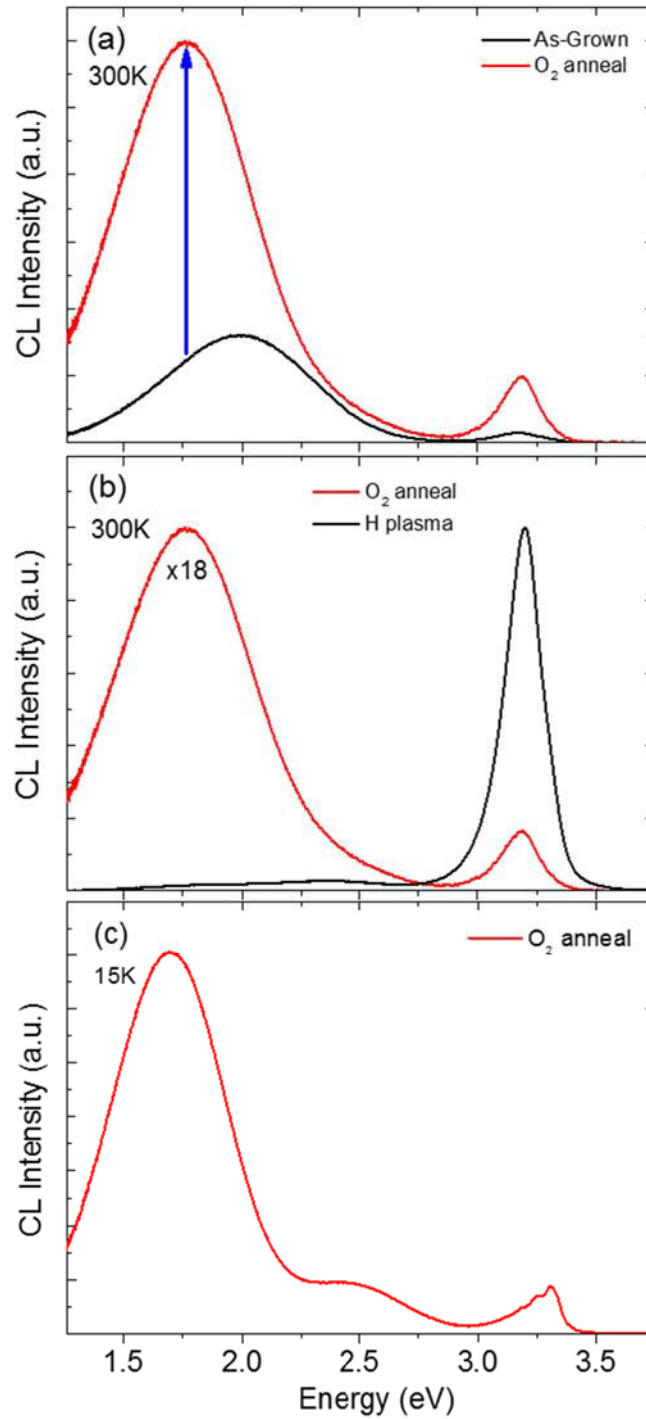
Figure 6.2: Typical cathodoluminescence spectra collected with 5 kV, I_B = 0.2 ± 0.02 nA and scan area = 50 μm ×43 μm. Figure 6.2a ZnO nanorods before ("as-grown") and after annealing at 650 °C in O_2 gas for 30 minutes, showing the creation of the red luminescence (RL) peak centered at 1.78 eV with a FWHM = 0.69 eV. Figure 6.2b illustrates rapid quenching of the RL following exposure to a mild hydrogen plasma

indicating that the RL relates to an acceptor-like center as hydrogen is a donor in ZnO. Figure 6.2c. RL spectrum at 15 K showing the peak red shifted to 1.69 eV and narrowing of the FWHM to 0.57 eV. The assignment of the RL to transition metal impurities is ruled out because of the absence of fine structure arising from internal 3d transitions.
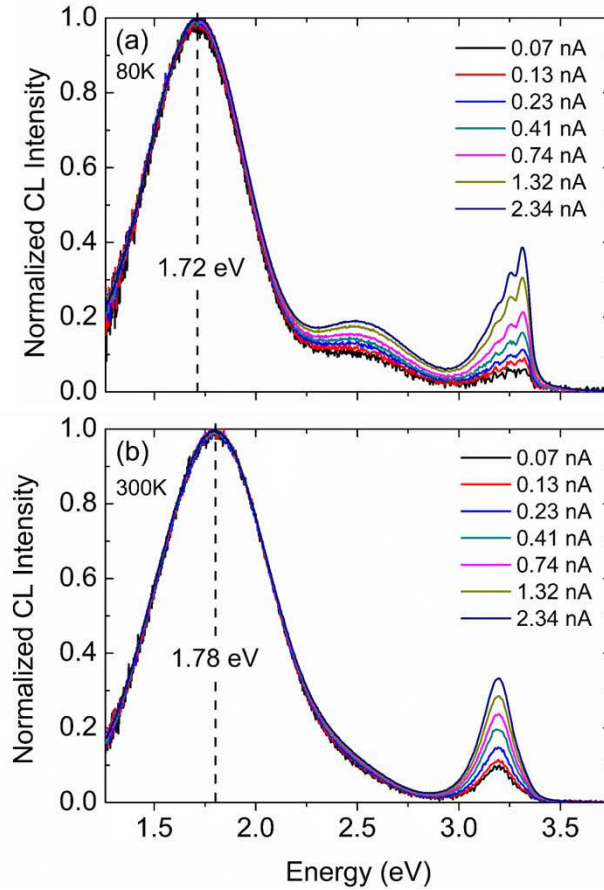
Figure 6.3: Normalized RL intensity versus excitation power (5 kV x I_B) at 80 K (a) and 300 K (b). The absence of a blue peak shift with increasing beam current eliminates the assignment of the RL to donor acceptor pair recombination transitions.

The temperature resolved CL spectroscopy of the O_2 annealed ZnO nanorods sample is presented in Figure 6.5 from 93 K increasing to 300 K. Figure 6.6 presents the temperature dependence of the peak position (Figure 6.6a), FWHM (Figure 6.6b), and emission intensity (Figure 6.6c), of the RL. The peak position $E_{RL}(T)$ exhibits a roughly linear blue shift with increasing temperature with $E_{RL}(T) = E(0K) + \alpha k_b T$,

where $E(0K) = 1.66$ eV and $\alpha = 0.296 \pm 0.009$ meV / K in agreement with the CC model. The FWHM of the RL can be expressed below derived from the CC model.[246]

$$FWHM\ (T) = A.\sqrt{coth\left[\frac{\hbar\omega}{2k_bT}\right]}$$

The vibrational energy of the excited state, $\hbar\omega$, for the RL was found to be 34.7 ± 0.6 meV, where FWHM(0) is the peak width approaching 0 K.
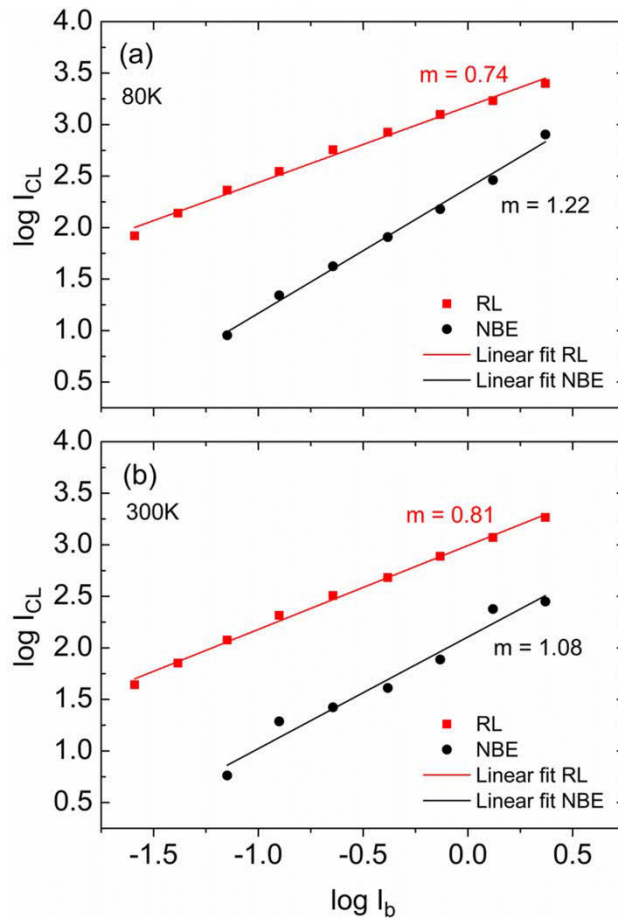
Figure 6.4: Plot of log (I_{CL}) versus log (I_B) at 80 K (a) and 300 K (b) with I_B in nA. The gradient, n, is the power law exponent in the relationship, $I_{CL} \propto I_B^n$. The $n_{NBE} \sim 1$ is expected for excitonic recombination. The $n_{RL} \sim 0.8$ is higher than expected for a lattice coupled defect most likely due to a high concentration of RL centers.

The CL intensity (I_{CL}) versus temperature dependence for RL is presented in Figure 6.6c for temperatures decreasing from 300 to 93 K following the usual thermal quenching relationship

$$I_{CL}(T) = \frac{I(0)}{\left[1 + Aexp\left(\frac{-E_A}{k_bT}\right)\right]}$$

where E_A is the activation energy for thermal quenching and A is a constant. An activation energy of E_A = 78.8 ± 5.1 meV was obtained from an Arrhenius plot (not shown) using the data in Figure 6.6c which is most likely due to thermal quenching of competitive non-radiative recombination centers. Remarkably a different I_{CL} versus temperature profile is observed when heating from 93 to 300 K compared to cooling from 300 to 93 K. Specifically with increasing temperature a faster thermal quenching of the luminescence is observed followed by an anomalous increase in I_{CL} at around 180 K then further decay to 300 K. This thermal behavior can be explained by the presence of competitive charge traps that are created during the O_2 thermal annealing process. These traps capture carriers at low temperature which are subsequently released with further heating and recombine radiatively producing an increase in intensity of the RL [247]. The existence of excess carriers arising from thermal depopulation of charge traps filled at low temperature is also evidenced by a corresponding "negative" thermal quenching of the NBE as shown in Figure 6.4a and 6.4b.

The RL has been ascribed to both singly ionized N on an oxygen site, N_O^- [178] and a doubly ionized zinc vacancy, V_{Zn}^{2-} [180]. Although the chemical origin of the ionized acceptor is different in these two models, the underlying luminescence mechanism is the same. Here, the electron at a singly (doubly) ionized acceptor, A^- (A^{2-}) is photoexcited creating an electron in the conduction band, e_{CB}, and a neutral (singly ionized) acceptor, A^o (A^-) which induces a large lattice dilation, producing a strong Jahn-Teller distortion. The excited A^o (A^-) radiatively relaxes to A^- (A^{2-}), via capture of a conduction band electron, generating RL due to the Stokes shift caused by the Jahn-Teller distortion. The excitation and relaxation cycles for singly and doubly ionized acceptors are given below.

$$A^- + \hbar\omega \xrightarrow{excitation} A^0 + e_{CB} \xrightarrow{relaxation} A^- + RL$$
$$A^{2-} + \hbar\omega \xrightarrow{excitation} A^- + e_{CB} \xrightarrow{relaxation} A^{2-} + RL$$
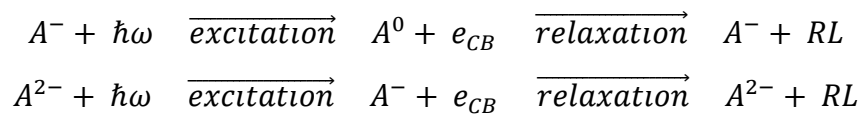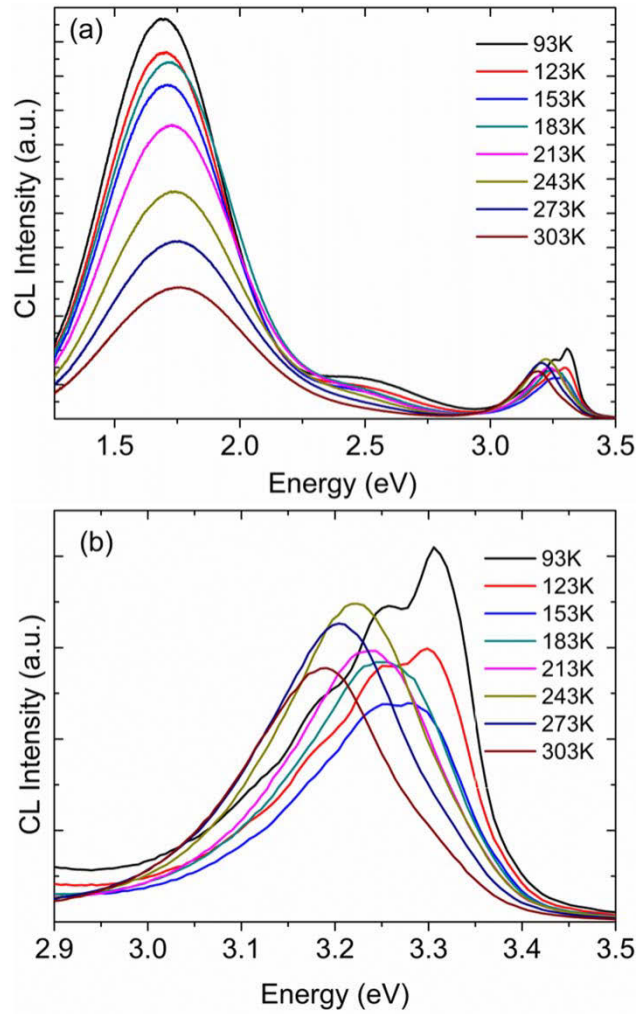
Figure 6.5: CL intensity versus temperature at 80 K for the RL (a) and NBE (b) with 300 K with 5 kV, $I_B = 0.2 \pm 0.02$ nA and scan area = 50 μm × 43 μm. The red shift and narrowing of the RL with decreasing temperature is consistent with configuration coordinate model for radiative recombination. The blue shift and appearance of phonon replicas as the temperature approaches 93 K is expected for excitonic emission with the bandgap shrinkage. The intensity of the RL and NBE exhibits "negative" thermal quenching with increasing temperature.

It is important to note that in CL the recombination energy provides the excitation energy for these processes. CL spectra of the NBE (Figure 6.7a) show three peaks, the first at 3.36 eV ascribed to a donor bound exciton, D^oX, and two others positioned at 3.32 and 3.26 eV. The latter two peaks have been attributed to nitrogen acceptors in DAPs [32] by other works, however, this assignment in our ZnO nanorod is implausible as no nitrogen was detected using high sensitivity chemical analysis, as

discussed below. The corresponding CL spectra shown in (Figure 6.7b) reveal an anti-correlation between the intensity of the RL and the NBE peaks at 3.32 and 3.26 eV. It is also noteworthy that the peak position of these two NBE peaks is fixed as the temperature increases from 7 to 100 K (Figure 6.8a and 6.8b) despite the red shift of the D^oX with the increase in the band gap due to electron-phonon scattering and lattice expansion. The absence of a thermal shift can be accounted for by a free-to-bound transition (FBT) not a DAP recombination mechanism. In FBT recombination at temperatures from 7 to 100 K the thermal energy of the free carrier, k_bT, roughly offsets the red shift of the bandgap with increasing temperature with $E_{FBT} = E_g - E_A + k_bT$, where E_{FBT} is the position of the FBT peak and E_A is the ionization energy of the acceptor.

ZnO nanorods exposed to a mild nitrogen plasma show a well-defined set of N kα peaks in the Total Fluorescence Yield (TFY) XANES spectroscopy results (Figure 6.9) which are clearly absent in the as-grown and O_2 anneal samples. TFY mode was select to collect XANES data from the entire volume of the nanowire ensemble. These results strongly suggest that the concentration of N in the ZnO nanorods studied in this work is extremely low and consequently the RL at 1.76 eV and the NBE peaks at 3.32 and 3.26 eV are all not related to recombination centers involving N. Electron Spin Resonance (ESR) spectroscopy results are shown in Figure 5.4(a). No ESR hyperfine signal corresponding to nitrogen was detected. Two very weak resonances at g $\sim$ 1.96 and g $\sim$ 2.01 with similar intensities are observed before and after annealing in O_2. These ESR lines, attributed to shallow donor impurities and singly ionized surface oxygen vacancies respectively[215], clearly have no connection with the appearance of the RL following O_2 annealing and the RL has no correlated ESR resonance over the range of measured g-values supporting its assignment to the non-paramagnetic V_{Zn}^{2-} center.
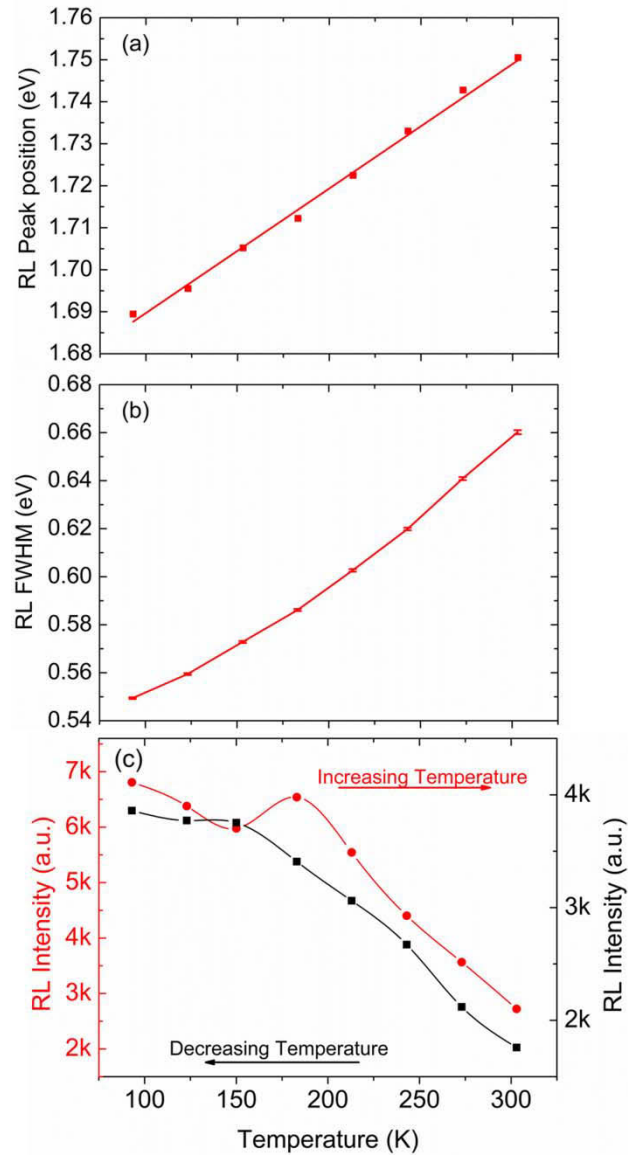
Figure 6.6: The plot of the RL peak position and peak width as a function of temperature are shown in Figure 6.6a and Figure 6.6b. Figure 5.6c displays the RL intensity dependence on temperature. With decreasing temperature from 300 K to 93 K a typical thermal response relationship with an activation energy of $E_A = 78.8$ meV is found. However, increasing the temperature from 93 K to 300 K "negative" thermal quenching is observed arising from the presence of shallow levels that fill with carriers at low temperature during electron beam excitation and depopulate with rising temperature increasing the luminescence intensity.
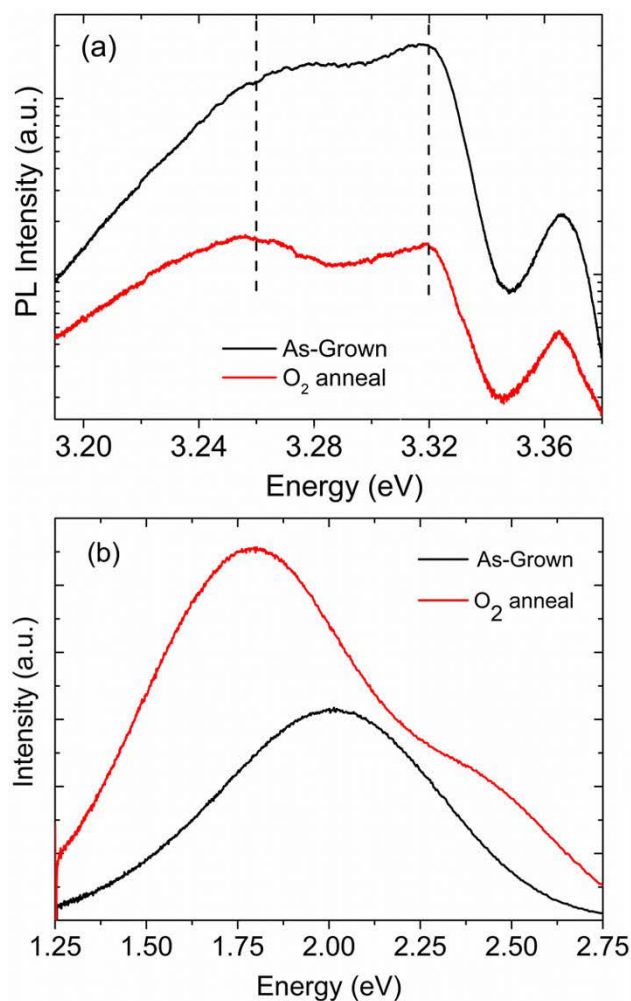
Figure 6.7: CL spectra at 80 K of the NBE and RL before and after thermal annealing in O$_2$ are shown in Figure 6.7a with corresponding CL spectra in Figure 6.7b. Figure 6.7a reveals emission due to donor bound exciton around 3.36 eV and peaks at 3.32 and 3.26 eV ascribed to the presence of acceptors in either DAP or free-to-bound transitions. No interrelationship between the 3.32 and 3.26 eV NBE peaks and the RL in the CL spectra is observed. Additionally there is no correlation between the free-to-bound NBE and RL peaks and nitrogen as confirmed in the N kα XANES results in Figure 6.9.
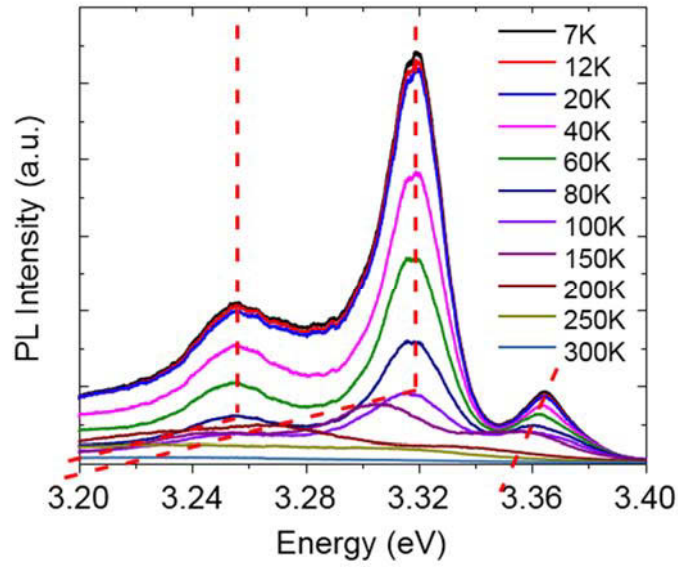
Figure 6.8: The temperature dependence of the DᵒX and peaks at 3.32 and 3.26 eV are shown in Figure 6.8. The data show the usual red shift of the DᵒX with increasing temperature as the band gap widens due to lattice expansion and the electron-phonon effect. The absence of a corresponding shift of the 3.32 and 3.26 eV peaks between 7 and 100 K indicates that free carriers are involved in the recombination process providing thermal energy (k_bT) which offsets the band gap red shift. This result suggests that these emission peaks arise from free-to-bound transition rather than a DAP recombination process.

From the characterization studies above, the broad RL positioned at 1.78 eV at 300 K in our O$_2$ annealed ZnO nanorods has been cautiously ascribed to highly lattice coupled V$_{Zn}$-related acceptor like centers. Its CL excitation and relaxation cycle is as follows:

$$V_{Zn}^{2-} + E_{recombination} \quad \overrightarrow{excitation} \quad V_{Zn}^{-} + e_{CB} \quad \overrightarrow{relaxation} \quad V_{Zn}^{2-} + RL$$
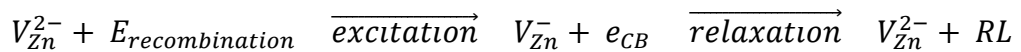
This is assignment is consistent with: (i) the observed quenching of the RL on exposure to a H plasma forming V$_{Zn}$-H complexes, (ii) the low formation energy of V$_{Zn}$ point defects under oxygen rich annealing conditions, (iii) the absence of nitrogen in our ZnO nanorod samples, (iv) the large lattice dilation induced by creation of neutral V_{Zn}^{o} centers and (v) the temperature dependence of the RL peak position and FWHM with the configurational co-ordinate model.
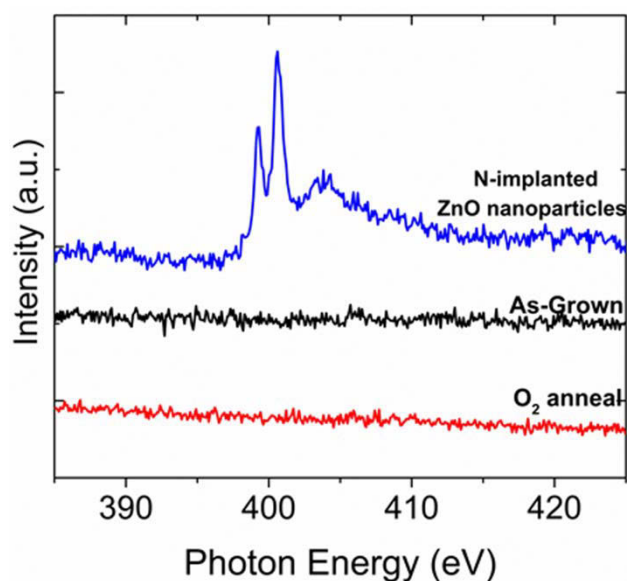
Figure 6.9: XANES spectra around the N kα energy from the "as-grown" and O_2 annealed samples, as well as from ZnO nano-particles implanted with nitrogen, are shown in Figure 6.9. The results show that no nitrogen is present in both the "as-grown" and O_2 annealed samples.

6.5 Conclusions

A strong broad red luminescence (RL) centered at 1.69 eV (FWHM = 0.57 eV) at 15K and 1.78 eV (FWHM = 0.69 eV) at 300 K is formed in ZnO nanorods following thermal annealing at 650°C for 30 minutes in an O_2 gas environment. The optical properties of this peak were comprehensively studied using a range of characterization techniques, in particular photoluminescence and cathodoluminescence spectroscopy. Using these results, the RL has been assigned to highly lattice coupled V_{Zn}-related acceptor-like centers. No correlation was found between the RL and nitrogen impurities.

CHAPTER VII
CONCLUSIONS

The main aim of this thesis was to investigate the effect of deep level surface point defects on optical and electrical properties, gas sensing properties and the surface electronic structure of ZnO nanorods. Additionally, the emission properties of red luminescence at 1.78 eV were systematically characterized as a function of temperature and excitation density to gain a deeper insight into its chemical origin. These key finding of this research are summarized below.

ZnO nanorods were successfully grown by low temperature (90 °C) hydrothermal method. The various types of surface point defects were also systematically introduce into ZnO nanorods by thermal treatments in oxidative and reductive environments. The low temperature growth technique employed in the preparation of ZnO nanorods in sensor devices shows great promise as an alternative method to the existing high temperature routes due to its simplicity, application to temperature sensitive substrates, energy efficiency, and reproducibility in obtaining nanostructured ZnO for room temperature NH_3 gas sensor applications. CL spectroscopy confirmed that post-growth-controlled atmosphere heat treatment can be used to mediate the Fermi level position of the ZnO nanorods through the creation of acceptor or donor native near surface defects, which governs the sign and magnitude of the electrical response to NH_3 gas. Specifically a room temperature NH_3 gas sensitivity of S = 22.6 was achieved by heating in O_2 atmosphere at 650 °C that was 5 times greater than S for as-grown ZnO nanorods. The reported findings on the inter-relationship between surface point defects, electrical properties, and gas sensing properties of nanostructured ZnO will facilitate the development of future, low cost, high-sensitivity, room temperature gas sensor devices tailored for specific applications.

Optical and electrical characterization studies of ZnO nanorods before and after annealing in O_2 gas and Zn vapor have confirmed that the surface electronic structure can be bespoke for specific sensor applications. These correlative spectroscopy measurements reveal clear evidence of direct interrelationship between the electronic

properties of the ZnO nanorod surface and its surface defect structure. In particular, the role of intrinsic point defects on the physisorption and chemisorption of water molecules and hydroxyl groups which, through charge transfer mechanisms, govern both the surface band bending effects and the surface conductivity. Additionally O1s XPS spectra established that the number of adsorbed water and hydroxyl species on the ZnO nanorod is directly proportional to the concentration of surface oxygen vacancies. An important result of these studies is compelling experimental evidence for the existence of stable singly ionized oxygen vacancies (V_O^+) at the ZnO nanorod surface. Furthermore, it was shown that (i) a broad green CL peak centered at 2.43 eV, (ii) an intense ESR line at $g \cong 2.01$ and (iii) a pronounced shoulder in the valence band X-ray photoemission spectra ~ 3.0 eV below the Fermi level, can all be attributed to centers involving surface V_O^+ centers.

A strong broad red luminescence (RL) centered at 1.69 eV (FWHM = 0.57 eV) at 15K and 1.78 eV (FWHM = 0.69 eV) at 300 K is formed in ZnO nanorods following thermal annealing at 650°C for 30 minutes in an O_2 gas environment. The optical properties of this peak were comprehensively studied using a range of characterization techniques, in particular photoluminescence and cathodoluminescence spectroscopy. Using these results, the RL has been assigned to highly lattice coupled V_{Zn}-related acceptor-like centers. No correlation was found between the RL and nitrogen impurities.

REFERENCES

1. Aslani, A.; Arefi, M. R.; Babapoor, A.; Amiri, A.; Beyki-Shuraki, K., Solvothermal Synthesis, Characterization and Optical Properties of ZnO, ZnO–MgO and ZnO–NiO, Mixed Oxide Nanoparticles. *Applied Surface Science* **2011**, *257*, 4885-4889.

2. Ozgur, U.; Alivov, Y. I.; Liu, C.; Teke, A.; Reshchikov, M. A.; Dogan, S.; Avrutin, V.; Cho, S. J.; Morkoc, H., A Comprehensive Review of ZnO Materials and Devices. *Journal of Applied Physics* **2005**, *98*, 041301-103.

3. Huang, M. H.; Mao, S.; Feick, H.; Yan, H.; Wu, Y.; Kind, H.; Weber, E.; Russo, R.; Yang, P., Room-Temperature Ultraviolet Nanowire Nanolasers. *Science* **2001**, *292*, 1897-1899.

4. Li, H.; Huang, Y.; Zhang, Q.; Liu, J.; Zhang, Y., Influence of Electromechanical Coupling and Electron Irradiation on the Conductivity of Individual ZnO Nanowire. *Solid State Sciences* **2011**, *13*, 658-661.

5. Gao, P.; Wang, Z. Z.; Liu, K. H.; Xu, Z.; Wang, W. L.; Bai, X. D.; Wang, E. G., Photoconducting Response on Bending of Individual ZnO Nanowires. *Journal of Materials Chemistry* **2009**, *19*.

6. Anderson, J.; Chris, G. V. d. W., Fundamentals of Zinc Oxide as a Semiconductor. *Reports on Progress in Physics* **2009**, *72*, 126501.

7. Wei, A.; Pan, L.; Huang, W., Recent Progress in the ZnO Nanostructure-Based Sensors. *Materials Science and Engineering: B* **2011**, *176*, 1409-1421.

8. Han, J.; Mantas, P. Q.; Senos, A. M. R., Defect Chemistry and Electrical Characteristics of Undoped and Mn-Doped ZnO. *Journal of the European Ceramic Society* **2002**, *22*, 49-59.

9. Charnhattakorn, B.; Charinpanitkul, T.; Sirisuk, A.; Pavarajarn, V., Controlled Synthesis of Defects-Containing ZnO by the French Process Modified with Pulsed Injection and Its Luminescence Properties. *Ceramics International* **2011**, *37*, 2021-2024.

10. Lim, S. H.; Shindo, D.; Kang, H. B.; Nakamura, K., Study of Defects and Interfaces in Epitaxial ZnO Films on (1 $\bar{1}$2 0) Al_2O_3 Grown by Electron Cyclotron

Resonance-Assisted Molecular Beam Epitaxy. *Journal of Crystal Growth* **2001**, *225*, 202-207.

11. Ament, W.; Huizenga, J.; Kort, E.; Van Der Mark, T.; Grevink, R.; Verkerke, G., Respiratory Ammonia Output and Blood Ammonia Concentration During Incremental Exercise. *International Journal of Sports Medicine* **1999**, *20*, 71-77.

12. Narasimhan, L.; Goodman, W.; Patel, C. K. N., Correlation of Breath Ammonia with Blood Urea Nitrogen and Creatinine During Hemodialysis. *Proceedings of the National Academy of Sciences* **2001**, *98*, 4617-4621.

13. Kearney, D. J.; Hubbard, T.; Putnam, D., Breath Ammonia Measurement in Helicobacter Pylori Infection. *Digestive Diseases and Sciences* **2002**, *47*, 2523-2530.

14. Hassan, J.; Mahdi, M.; Chin, C.; Abu-Hassan, H.; Hassan, Z., Room Temperature Hydrogen Gas Sensor Based on ZnO Nanorod Arrays Grown on a SiO_2/Si Substrate Via a Microwave-Assisted Chemical Solution Method. *Journal of Alloys and Compounds* **2013**, *546*, 107-111.

15. Chang, C. M.; Hon, M. H.; Leu, I. C., Preparation of ZnO Nanorod Arrays with Tailored Defect-Related Characterisitcs and Their Effect on the Ethanol Gas Sensing Performance. *Sensors and Actuators B: Chemical* **2010**, *151*, 15-20.

16. Law, J.; Thong, J., Improving the NH_3 Gas Sensitivity of ZnO Nanowire Sensors by Reducing the Carrier Concentration. *Nanotechnology* **2008**, *19*, 205502.

17. Spencer, M. J., Gas Sensing Applications of 1D-Nanostructured Zinc Oxide: Insights from Density Functional Theory Calculations. *Progress in Materials Science* **2012**, *57*, 437-486.

18. Xue, X.; Nie, Y.; He, B.; Xing, L.; Zhang, Y.; Wang, Z. L., Surface Free-Carrier Screening Effect on the Output of a ZnO Nanowire Nanogenerator and Its Potential as a Self-Powered Active Gas Sensor. *Nanotechnology* **2013**, *24*, 225501.

19. Timmer, B.; Olthuis, W.; Van Den Berg, A., Ammonia Sensors and Their Applications—a Review. *Sensors and Actuators B: Chemical* **2005**, *107*, 666-677.

20. Erisman, J. W.; Otjes, R.; Hensen, A.; Jongejan, P.; van den Bulk, P.; Khlystov, A.; Möls, H.; Slanina, S., Instrument Development and Application in Studies and Monitoring of Ambient Ammonia. *Atmospheric Environment* **2001**, *35*, 1913-1922.

21. Mount, G. H.; Rumburg, B.; Havig, J.; Lamb, B.; Westberg, H.; Yonge, D.; Johnson, K.; Kincaid, R., Measurement of Atmospheric Ammonia at a Dairy Using Differential Optical Absorption Spectroscopy in the Mid-Ultraviolet. *Atmospheric Environment* **2002**, *36*, 1799-1810.

22. Durbin, T. D.; Wilson, R. D.; Norbeck, J. M.; Miller, J. W.; Huai, T.; Rhee, S. H., Estimates of the Emission Rates of Ammonia from Light-Duty Vehicles Using Standard Chassis Dynamometer Test Cycles. *Atmospheric Environment* **2002**, *36*, 1475-1482.

23. Budavari, S.; O'Neil, M.; Smith, A., The Merck Index: An Encyclopedia of Chemicals, Drugs and Biologicals, Rahway, New Jersey, Merck and Co. *Inc.* **1989**.

24. Moos, R.; Müller, R.; Plog, C.; Knezevic, A.; Leye, H.; Irion, E.; Braun, T.; Marquardt, K.-J.; Binder, K., Selective Ammonia Exhaust Gas Sensor for Automotive Applications. *Sensors and Actuators B: Chemical* **2002**, *83*, 181-189.

25. de la Hoz, R. E.; Schlueter, D. P.; Rom, W. N., Chronic Lung Disease Secondary to Ammonia Inhalation Injury: A Report on Three Cases. *American Journal of Industrial Medicine* **1996**, *29*, 209-214.

26. Lide, D. R., *Crc Handbook of Chemistry and Physics*; CRC press, 2004.

27. Schmidt-Mende, L.; MacManus-Driscoll, J. L., ZnO–Nanostructures, Defects, and Devices. *Materials today* **2007**, *10*, 40-48.

28. Wöll, C., The Chemistry and Physics of Zinc Oxide Surfaces. *Progress in Surface Science* **2007**, *82*, 55-120.

29. Özgür, Ü.; Alivov, Y. I.; Liu, C.; Teke, A.; Reshchikov, M.; Doğan, S.; Avrutin, V.; Cho, S.-J.; Morkoc, H., A Comprehensive Review of ZnO Materials and Devices. *Journal of applied physics* **2005**, *98*, 041301.

30. Laskowski, R.; Christensen, N. E., Ab Initio Calculation of Excitons in ZnO. *Physical Review B* **2006**, *73*, 045201.

31. Janotti, A.; Van de Walle, C. G., Fundamentals of Zinc Oxide as a Semiconductor. *Reports on Progress in Physics* **2009**, *72*, 126501.

32. Meyer, B.; Alves, H.; Hofmann, D.; Kriegseis, W.; Forster, D.; Bertram, F.; Christen, J.; Hoffmann, A.; Straßburg, M.; Dworzak, M., Bound Exciton and Donor–Acceptor Pair Recombinations in ZnO. *Physica Status Solidi (b)* **2004**, *241*, 231-260.

33. Cobet, M.; Cobet, C.; Wagner, M. R.; Esser, N.; Thomsen, C.; Hoffmann, A., Polariton Effects in the Dielectric Function of ZnO Excitons Obtained by Ellipsometry. *Applied Physics Letters* **2010**, *96*, 031904.

34. Varshni, Y., Temperature Dependence of the Energy Gap in Semiconductors. *Physica* **1967**, *34*, 149-154.

35. Jagadish, C.; Pearton, S. J., *Zinc Oxide Bulk, Thin Films and Nanostructures: Processing, Properties, and Applications*; Elsevier, 2011.

36. Shluger, A.; Foster, A.; Gavartin, J.; Sushko, P.; Greer, J.; Korkin, A., Models of Defects in Wide-Gap Oxides: Perspective and Challenges. *Nano and Giga Challenges in Microelectronics* **2003**, 151-222.

37. Morris Jr, J., A Survey of Materials Science I. Structure *University of California, Berkeley* **2007**.

38. Jacobs, K., Fa Kröger. The Chemistry of Imperfect Crystals. Volume 1: Preparation, Purification, Crystal Growth and Phase Theory. North-Holland Publishing Company-Amsterdam/London 1973 American Elsevier Publishing Company, Inc.-New York 313 Seiten, Zahlreiche Abbildungen Und Tabellen, Kunstleder Preis Dfl. 70.00. *Kristall und Technik* **1974**, *9*, K67-K68.

39. Kohan, A.; Ceder, G.; Morgan, D.; Van de Walle, C. G., First-Principles Study of Native Point Defects in ZnO. *Physical Review B* **2000**, *61*, 15019.

40. Janotti, A.; Van de Walle, C. G., Native Point Defects in ZnO. *Physical Review B* **2007**, *76*, 165202.

41. Evans, S.; Giles, N.; Halliburton, L.; Kappers, L., Further Characterization of Oxygen Vacancies and Zinc Vacancies in Electron-Irradiated ZnO. *Journal of Applied Physics* **2008**, *103*, 043710-043710-7.

42. Reynolds, D.; Look, D.; Jogai, B.; Van Nostrand, J.; Jones, R.; Jenny, J., Source of the Yellow Luminescence Band in GaN Grown by Gas-Source Molecular Beam Epitaxy and the Green Luminescence Band in Single Crystal ZnO. *Solid State Communications* **1998**, *106*, 701-704.

43. Reynolds, D. C.; Look, D. C.; Jogai, B.; Morkoc, H., Similarities in the Bandedge and Deep-Centre Photoluminescence Mechanisms of ZnO and GaN. *Solid State Communications* **1997**, *101*, 643-646.

44. Janotti, A.; Van de Walle, C. G., Oxygen Vacancies in ZnO. *Applied Physics Letters* **2005**, *87*, 122102.

45. Erhart, P.; Klein, A.; Albe, K., First-Principles Study of the Structure and Stability of Oxygen Defects in Zinc Oxide. *Physical Review B* **2005**, *72*, 085213.

46. Paudel, T. R.; Lambrecht, W. R., First-Principles Calculation of the O Vacancy in ZnO: A Self-Consistent Gap-Corrected Approach. *Physical Review B* **2008**, *77*, 205202.

47. Erhart, P.; Albe, K.; Klein, A., First-Principles Study of Intrinsic Point Defects in ZnO: Role of Band Structure, Volume Relaxation, and Finite-Size Effects. *Physical Review B* **2006**, *73*, 205203.

48. Oba, F.; Togo, A.; Tanaka, I.; Paier, J.; Kresse, G., Defect Energetics in ZnO: A Hybrid Hartree-Fock Density Functional Study. *Physical Review B* **2008**, *77*, 245202.

49. Janotti, A.; Van de Walle, C. G., Hydrogen Multicentre Bonds. *Nature materials* **2006**, *6*, 44-47.

50. Vanheusden, K.; Warren, W.; Seager, C.; Tallant, D.; Voigt, J.; Gnade, B., Mechanisms Behind Green Photoluminescence in ZnO Phosphor Powders. *Journal of Applied Physics* **1996**, *79*, 7983-7990.

51. Vlasenko, L.; Watkins, G., Optical Detection of Electron Paramagnetic Resonance in Room-Temperature Electron-Irradiated ZnO. *Physical Review B* **2005**, *71*, 125210.

52. Hofmann, D.; Pfisterer, D.; Sann, J.; Meyer, B.; Tena-Zaera, R.; Munoz-Sanjose, V.; Frank, T.; Pensl, G., Properties of the Oxygen Vacancy in ZnO. *Applied Physics A* **2007**, *88*, 147-151.

53. Sann, J.; Stehr, J.; Hofstaetter, A.; Hofmann, D.; Neumann, A.; Lerch, M.; Haboeck, U.; Hoffmann, A.; Thomsen, C., Zn Interstitial Related Donors in Ammonia-Treated ZnO Powders. *Physical Review B* **2007**, *76*, 195203.

54. Dingle, R., Luminescent Transitions Associated with Divalent Copper Impurities and the Green Emission from Semiconducting Zinc Oxide. *Physical Review Letters* **1969**, *23*, 579.

55. Schirmer, O.; Zwingel, D., The Yellow Luminescence of Zinc Oxide. *Solid State Communications* **1970**, *8*, 1559-1563.

56. Pantelides, S. T., Deep Centers in Semiconductors; *CRC Press*, **1992**.

57. Glicksman, M., Diffusion in Solids: Field Theory, Solid-State Principles, and Applications, **2000**. *John Wiley & Sons, Inc., New York.*

58. Kador, L., Cathodoluminescence. Theory and Applications. ; *Weinheim/VCH Publishers, New York/Kodansha, Tokio*, **1990**.

59. Yacobi, B., Semiconductor Materials: An Introduction to Basic Principles; *Springer*, **2003**.

60. Reynolds, D.; Litton, C.; Collins, T., Zeeman Effects in the Edge Emission and Absorption of ZnO. *Physical Review* **1965**, *140*, A1726-A1734.

61. Zwingel, D., Trapping and Recombination Processes in the Thermoluminescence of Li-Doped ZnO Single Crystals. *Journal of Luminescence* **1972**, *5*, 385-405.

62. Boemare, C.; Monteiro, T.; Soares, M.; Guilherme, J.; Alves, E., Photoluminescence Studies in ZnO Samples. *Physica B: Condensed Matter* **2001**, *308*, 985-988.

63. Teke, A.; Özgür, Ü.; Doğan, S.; Gu, X.; Morkoç, H.; Nemeth, B.; Nause, J.; Everitt, H., Excitonic Fine Structure and Recombination Dynamics in Single-Crystalline ZnO. *Physical Review B* **2004**, *70*, 195207.

64. Reynolds, D.; Look, D. C.; Jogai, B.; Litton, C.; Collins, T.; Harsch, W.; Cantwell, G., Neutral-Donor–Bound-Exciton Complexes in ZnO Crystals. *Physical Review B* **1998**, *57*, 12151.

65. Alves, H.; Pfisterer, D.; Zeuner, A.; Riemann, T.; Christen, J.; Hofmann, D.; Meyer, B., Optical Investigations on Excitons Bound to Impurities and Dislocations in ZnO. *Optical Materials* **2003**, *23*, 33-37.

66. Thonke, K.; Gruber, T.; Teofilov, N.; Schönfelder, R.; Waag, A.; Sauer, R., Donor–Acceptor Pair Transitions in ZnO Substrate Material. *Physica B: Condensed Matter* **2001**, *308*, 945-948.

67. Dietz, R.; Kamimura, H.; Sturge, M.; Yariv, A., Electronic Structure of Copper Impurities in ZnO. *Physical Review* **1963**, *132*, 1559.

68. Yang, X.; Du, G.; Wang, X.; Wang, J.; Liu, B.; Zhang, Y.; Liu, D.; Liu, D.; Ong, H.; Yang, S., Effect of Post-Thermal Annealing on Properties of ZnO Thin Film Grown on C-Al_2O_3 by Metal-Organic Chemical Vapor Deposition. *Journal of Crystal Growth* **2003**, *252*, 275-278.

69. Korsunska, N.; Borkovska, L.; Bulakh, B.; Khomenkova, L. Y.; Kushnirenko, V.; Markevich, I., The Influence of Defect Drift in External Electric Field on Green Luminescence of ZnO Single Crystals. *Journal of Luminescence* **2003**, *102*, 733-736.

70. Lin, B.; Fu, Z.; Jia, Y., Green Luminescent Center in Undoped Zinc Oxide Films Deposited on Silicon Substrates. *Applied Physics Letters* **2001**, *79*, 943-945.

71. Vanheusden, K.; Seager, C.; Warren, W. t.; Tallant, D.; Voigt, J., Correlation between Photoluminescence and Oxygen Vacancies in ZnO Phosphors. *Applied Physics Letters* **1996**, *68*, 403-405.

72. Vanheusden, K.; Seager, C.; Warren, W.; Tallant, D.; Caruso, J.; Hampden-Smith, M.; Kodas, T., Green Photoluminescence Efficiency and Free-Carrier Density in ZnO Phosphor Powders Prepared by Spray Pyrolysis. *Journal of luminescence* **1997**, *75*, 11-16.

73. Leiter, F.; Alves, H.; Hofstaetter, A.; Hofmann, D.; Meyer, B., The Oxygen Vacancy as the Origin of a Green Emission in Undoped ZnO. *Physica Status Solidi (b)* **2001**, *226*, R4-R5.

74. Leiter, F.; Alves, H.; Pfisterer, D.; Romanov, N.; Hofmann, D.; Meyer, B., Oxygen Vacancies in ZnO. *Physica B: Condensed Matter* **2003**, *340*, 201-204.

75. Studenikin, S.; Golego, N.; Cocivera, M., Fabrication of Green and Orange Photoluminescent, Undoped ZnO Films Using Spray Pyrolysis. *Journal of Applied Physics* **1998**, *84*, 2287-2294.

76. Kwok, W.; Djurišić, A.; Leung, Y.; Chan, W.; Phillips, D., Time-Resolved Photoluminescence Study of the Stimulated Emission in ZnO Nanoneedles. *Applied Physics Letters* **2005**, *87*, 093108.

77. Liu, M.; Kitai, A.; Mascher, P., Point Defects and Luminescence Centres in Zinc Oxide and Zinc Oxide Doped with Manganese. *Journal of Luminescence* **1992**, *54*, 35-42.

78. Greene, L. E.; Law, M.; Goldberger, J.; Kim, F.; Johnson, J. C.; Zhang, Y.; Saykally, R. J.; Yang, P., Low-Temperature Wafer-Scale Production of ZnO Nanowire Arrays. *Angew Chem Int Ed Engl* **2003**, *42*, 3031-3034.

79. Djurišić, A.; Leung, Y.; Tam, K.; Hsu, Y.; Ding, L.; Ge, W.; Zhong, Y.; Wong, K.; Chan, W.; Tam, H., Defect Emissions in ZnO Nanostructures. *Nanotechnology* **2007**, *18*, 095702.

80. Liu, X.; Wu, X.; Cao, H.; Chang, R., Growth Mechanism and Properties of ZnO Nanorods Synthesized by Plasma-Enhanced Chemical Vapor Deposition. *Journal of Applied Physics* **2004**, *95*, 3141-3147.

81. Cox, R.; Block, D.; Hervé, A.; Picard, R.; Santier, C.; Helbig, R., Exchange Broadened, Optically Detected ESR Spectra for Luminescent Donor-Acceptor Pairs in Li Doped ZnO. *Solid State Communications* **1978**, *25*, 77-80.

82. Alvi, N.; Ul Hasan, K.; Nur, O.; Willander, M., The Origin of the Red Emission in N-ZnO Nanotubes/P-GaN White Light Emitting Diodes. *Nanoscale research letters* **2011**, *6*, 1-7.

83. Li, D.; Leung, Y.; Djurišić, A.; Liu, Z.; Xie, M.; Shi, S.; Xu, S.; Chan, W., Different Origins of Visible Luminescence in ZnO Nanostructures Fabricated by the Chemical and Evaporation Methods. *Applied Physics Letters* **2004**, *85*, 1601-1603.

84. Tarun, M.; Iqbal, M. Z.; McCluskey, M., Nitrogen Is a Deep Acceptor in ZnO. *AIP Advances*, **2011**, *1*, 022105.

85. Ehret, W.; Greenstone, A., Red Zinc Oxide. *Journal of the American Chemical Society* **1943**, *65*, 872-877.

86. Halliburton, L.; Giles, N.; Garces, N.; Luo, M.; Xu, C.; Bai, L.; Boatner, L. A., Production of Native Donors in ZnO by Annealing at High Temperature in Zn Vapor. *Applied Physics Letters* **2005**, *87*, 172108.

87. Weber, M.; Parmar, N.; Jones, K.; Lynn, K., Oxygen Deficiency and Hydrogen Turn ZnO Red. *Journal of Electronic Materials* **2010**, *39*, 573-576.

88. Chen, Y.; Xu, S.; Zheng, C.; Ning, J.; Ling, F.; Anwand, W.; Brauer, G.; Skorupa, W., Nature of Red Luminescence Band in Research-Grade ZnO Single Crystals: A "Self-Activated" Configurational Transition. *Applied Physics Letters* **2014**, *105*, 041912.

89. Hamby, D.; Lucca, D.; Klopfstein, M.; Cantwell, G., Temperature Dependent Exciton Photoluminescence of Bulk ZnO. *Journal of Applied Physics* **2003**, *93*, 3214-3217.

90. Hauschild, R.; Priller, H.; Decker, M.; Brückner, J.; Kalt, H.; Klingshirn, C., Temperature Dependent Band Gap and Homogeneous Line Broadening of the Exciton Emission in ZnO. *Physica Status Solidi (c)* **2006**, *3*, 976-979.

91. Li, J.; Ong, H., Temperature Dependence of Surface Plasmon Mediated Emission from Metal-Capped ZnO Films. *Applied Physics Letters* **2008**, *92*, 121107.

92. Morkoç, H.; Özgür, Ü., *Zinc Oxide: Fundamentals, Materials and Device Technology*; John Wiley & Sons, 2008.

93. Adachi, S., *Properties of Semiconductor Alloys: Group-Iv, Iii-V and Ii-Vi Semiconductors*; John Wiley & Sons, 2009; Vol. 28.

94. Van de Walle, C. G., Hydrogen as a Cause of Doping in Zinc Oxide. *Physical Review Letters* **2000**, *85*, 1012.

95. Strzhemechny, Y. M.; Mosbacker, H. L.; Look, D. C.; Reynolds, D. C.; Litton, C. W.; Garces, N. Y.; Giles, N. C.; Halliburton, L. E.; Niki, S.; Brillson, L. J., Remote Hydrogen Plasma Doping of Single Crystal ZnO. *Applied physics letters* **2004**, *84*, 2545-2547.

96. Nickel, N.; Fleischer, K., Hydrogen Local Vibrational Modes in Zinc Oxide. *Physical review letters* **2003**, *90*, 197402.

97. Ip, K.; Overberg, M.; Heo, Y.; Norton, D.; Pearton, S.; Stutz, C.; Luo, B.; Ren, F.; Look, D. C.; Zavada, J., Hydrogen Incorporation and Diffusivity in Plasma-Exposed Bulk ZnO. *Applied physics letters* **2003**, *82*, 385-387.

98. Oba, F.; Nishitani, S. R.; Isotani, S.; Adachi, H.; Tanaka, I., Energetics of Native Defects in ZnO. *Journal of Applied Physics* **2001**, *90*, 824-828.

99. Zhang, S.; Wei, S.-H.; Zunger, A., Intrinsic N-Type Versus P-Type Doping Asymmetry and the Defect Physics of ZnO. *Physical Review B* **2001**, *63*, 075205.

100. Look, D. C.; Farlow, G. C.; Reunchan, P.; Limpijumnong, S.; Zhang, S.; Nordlund, K., Evidence for Native-Defect Donors in N-Type ZnO. *Physical review letters* **2005**, *95*, 225502.

101. Hoppe, U.; Stachel, D.; Beyer, D., The Oxygen Coordination of Metal Ions in Phosphate and Silicate Glasses Studied by a Combination of X-Ray and Neutron Diffraction. *Physica Scripta* **1995**, *1995*, 122.

102. Iliadis, A.; Vispute, R.; Venkatesan, T.; Jones, K., Ohmic Metallization Technology for Wide Band-Gap Semiconductors. *Thin Solid Films* **2002**, *420*, 478-486.

103. Sheng, H.; Emanetoglu, N.; Muthukumar, S.; Feng, S.; Lu, Y., Nonalloyed Al Ohmic Contacts to $Mg_xZn_{1-}X_o$. *Journal of Electronic Materials* **2002**, *31*, 811-814.

104. Brillson, L. J.; Lu, Y., ZnO Schottky Barriers and Ohmic Contacts. *Journal of Applied Physics* **2011**, *109*, 121301.

105. Zhang, D.; Li, C.; Liu, X.; Han, S.; Tang, T.; Zhou, C., Doping Dependent NH_3 Sensing of Indium Oxide Nanowires. *Applied Physics Letters* **2003**, *83*, 1845-1847.

106. Wan, Q.; Wang, T., Single-Crystalline Sb-Doped SnO_2 Nanowires: Synthesis and Gas Sensor Application. *Chemical Communications* **2005**, 3841-3843.

107. Li, Q.; Liang, Y.; Wan, Q.; Wang, T., Oxygen Sensing Characteristics of Individual ZnO Nanowire Transistors. *Applied Physics Letters* **2004**, *85*, 6389-6391.

108. Basu, S.; Dutta, A., Modified Heterojunction Based on Zinc Oxide Thin Film for Hydrogen Gas-Sensor Application. *Sensors and Actuators B: Chemical* **1994**, *22*, 83-87.

109. Rout, C. S.; Raju, A.; Govindaraj, A.; Rao, C., Hydrogen Sensors Based on ZnO Nanoparticles. *Solid state communications* **2006**, *138*, 136-138.

110. Wang, H. T.; Kang, B. S.; Ren, F.; Tien, L. C.; Sadik, P. W.; Norton, D. P.; Pearton, S. J.; Lin, J., Hydrogen-Selective Sensing at Room Temperature with ZnO Nanorods. *Applied Physics Letters* **2005**, *86*, -.

111. Kang, B.; Heo, Y.; Tien, L.; Norton, D.; Ren, F.; Gila, B.; Pearton, S., Hydrogen and Ozone Gas Sensing Using Multiple ZnO Nanorods. *Applied Physics A* **2005**, *80*, 1029-1032.

112. Sarala Devi, G.; Bala Subrahmanyam, V.; Gadkari, S. C.; Gupta, S. K., Nh3 Gas Sensing Properties of Nanocrystalline ZnO Based Thick Films. *Analytica Chimica Acta* **2006**, *568*, 41-46.

113. Anantachaisilp, S.; Smith, S. M.; Ton-That, C.; Osotchan, T.; Moon, A. R.; Phillips, M. R., Tailoring Deep Level Surface Defects in ZnO Nanorods for High Sensitivity Ammonia Gas Sensing. *The Journal of Physical Chemistry C* **2014**, *118*, 27150-27156.

114. Nanto, H.; Minami, T.; Takata, S., Zinc-Oxide Thin-Film Ammonia Gas Sensors with High Sensitivity and Excellent Selectivity. *Journal of Applied Physics* **1986**, *60*, 482-484.

115. Kim, J.; Yong, K., Mechanism Study of ZnO Nanorod-Bundle Sensors for H_2S Gas Sensing. *The Journal of Physical Chemistry C* **2011**, *115*, 7218-7224.

116. Wang, C.; Chu, X.; Wu, M., Detection of H2s Down to ppb Levels at Room Temperature Using Sensors Based on ZnO Nanorods. *Sensors and Actuators B: Chemical* **2006**, *113*, 320-323.

117. Chang, J. F.; Kuo, H. H.; Leu, I. C.; Hon, M. H., The Effects of Thickness and Operation Temperature on ZnO:Al Thin Film CO Gas Sensor. *Sensors and Actuators B: Chemical* **2002**, *84*, 258-264.

118. Gong, H.; Hu, J. Q.; Wang, J. H.; Ong, C. H.; Zhu, F. R., Nano-Crystalline Cu-Doped ZnO Thin Film Gas Sensor for CO. *Sensors and Actuators B: Chemical* **2006**, *115*, 247-251.

119. Gao, T.; Wang, T. H., Synthesis and Properties of Multipod-Shaped ZnO Nanorods for Gas-Sensor Applications. *Applied Physics A* **2005**, *80*, 1451-1454.

120. Wang, X.-H.; Ding, Y.-F.; Zhang, J.; Zhu, Z.-Q.; You, S.-Z.; Chen, S.-Q.; Zhu, J., Humidity Sensitive Properties of ZnO Nanotetrapods Investigated by a Quartz Crystal Microbalance. *Sensors and Actuators B: Chemical* **2006**, *115*, 421-427.

121. Zhou, X.; Zhang, J.; Jiang, T.; Wang, X.; Zhu, Z., Humidity Detection by Nanostructured ZnO: A Wireless Quartz Crystal Microbalance Investigation. *Sensors and Actuators A: Physical* **2007**, *135*, 209-214.

122. Sberveglieri, G.; Nelli, P.; Groppelli, S.; Quaranta, F.; Valentini, A.; Vasanelli, L., Oxygen Gas Sensing Characteristics at Ambient Pressure of Undoped and Lithium-Doped ZnO-Sputtered Thin Films. *Materials Science and Engineering: B* **1990**, *7*, 63-68.

123. Martins, R.; Fortunato, E.; Nunes, P.; Ferreira, I.; Marques, A.; Bender, M.; Katsarakis, N.; Cimalla, V.; Kiriakidis, G., Zinc Oxide as an Ozone Sensor. *Journal of Applied Physics* **2004**, *96*, 1398-1408.

124. Baratto, C.; Sberveglieri, G.; Onischuk, A.; Caruso, B.; di Stasio, S., Low Temperature Selective NO_2 Sensors by Nanostructured Fibres of ZnO. *Sensors and Actuators B: Chemical* **2004**, *100*, 261-265.

125. Cho, P.-S.; Kim, K.-W.; Lee, J.-H., NO_2 Sensing Characteristics of ZnO Nanorods Prepared by Hydrothermal Method. *Journal of Electroceramics* **2006**, *17*, 975-978.

126. Hung, N. L.; Ahn, E. S.; Jung, H. C.; Kim, H. J.; Kim, D. J., Synthesis and Gas Sensing Properties of ZnO Nanostructures. *Journal of the Korean Physical Society* **2010**, *57*, 1784-1788.

127. Huang, X.-J.; Choi, Y.-K., Chemical Sensors Based on Nanostructured Materials. *Sensors and Actuators B: Chemical* **2007**, *122*, 659-671.

128. Fang, X.; Hu, L.; Ye, C.; Zhang, L., One-Dimensional Inorganic Semiconductor Nanostructures: A New Carrier for Nanosensors. *Pure and Applied Chemistry* **2010**, *82*, 2185-2198.

129. Kolmakov, A.; Zhang, Y.; Cheng, G.; Moskovits, M., Detection of CO and O_2 Using Tin Oxide Nanowire Sensors. *Advanced Materials* **2003**, *15*, 997-1000.

130. Williams, D. E., Semiconducting Oxides as Gas-Sensitive Resistors. *Sensors and Actuators B: Chemical* **1999**, *57*, 1-16.

131. Kolmakov, A.; Moskovits, M., Chemical Sensing and Catalysis by One-Dimensional Metal-Oxide Nanostructures. *Annu. Rev. Mater. Res.* **2004**, *34*, 151-180.

132. Huang, M. H.; Wu, Y.; Feick, H.; Tran, N.; Weber, E.; Yang, P., Catalytic Growth of Zinc Oxide Nanowires by Vapor Transport. *Advanced Materials* **2001**, *13*, 113-116.

133. Lu, C.; Qi, L.; Yang, J.; Tang, L.; Zhang, D.; Ma, J., Hydrothermal Growth of Large-Scale Micropatterned Arrays of Ultralong ZnO Nanowires and Nanobelts on Zinc Substrate. *Chemical Communications* **2006**.

134. Wu, J. J.; Liu, S. C., Low-Temperature Growth of Well-Aligned ZnO Nanorods by Chemical Vapor Deposition. *Advanced Materials* **2002**, *14*, 215-218.

135. Park, W. I.; Yi, G. C.; Kim, M.; Pennycook, S. J., ZnO Nanoneedles Grown Vertically on Si Substrates by Non-Catalytic Vapor-Phase Epitaxy. *Advanced Materials* **2002**, *14*, 1841-1843.

136. Tang, C. C.; Fan, S. S.; Chapelle, M. L. d. l.; Li, P., Silica-Assisted Catalytic Growth of Oxide and Nitride Nanowires. *Chemical Physics Letters* **2001**, *333*, 12-15.

137. Pan, Z. W.; Dai, Z. R.; Wang, Z. L., Nanobelts of Semiconducting Oxides. *Science* **2001**, *291*, 1947-1949.

138. Wang, Z.; Li, H. L., Highly Ordered Zinc Oxide Nanotubules Synthesized within the Anodic Aluminum Oxide Template. *Applied Physics A* **2002**, *74*, 201-203.

139. Miao, L.; Ieda, Y.; Tanemura, S.; Cao, Y.; Tanemura, M.; Hayashi, Y.; Toh, S.; Kaneko, K., Synthesis, Microstructure and Photoluminescence of Well-Aligned ZnO Nanorods on Si Substrate. *Science and Technology of Advanced Materials* **2007**, *8*, 443-447.

140. Dalal, S. H.; Baptista, D. L.; Teo, K. B. K.; Lacerda, R. G.; Jefferson, D. A.; Milne, W. I., Controllable Growth of Vertically Aligned Zinc Oxide Nanowires Using Vapour Deposition. *Nanotechnology* **2006**, *17*, 4811.

141. Satoh, Y.; Ohshio, S.; Saitoh, H., Photoluminescence Spectroscopy of Highly Oriented Y_2O_3: Tb Crystalline Whiskers. *Science and Technology of Advanced Materials* **2005**, *6*, 215-218.

142. Yasuda, T.; Segawa, Y., Zinc Oxide Thin Films Synthesized by Metal Organic Chemical Reactions. *Physica Status Solidi (b)* **2004**, *241*, 676-679.

143. Soci, C.; Zhang, A.; Xiang, B.; Dayeh, S. A.; Aplin, D.; Park, J.; Bao, X.; Lo, Y.-H.; Wang, D., ZnO Nanowire UV Photodetectors with High Internal Gain. *Nano Letters* **2007**, *7*, 1003-1009.

144. Lagashetty, A.; Havanoor, V.; Basavaraja, S.; Balaji, S.; Venkataraman, A., Microwave-Assisted Route for Synthesis of Nanosized Metal Oxides. *Science and Technology of Advanced Materials* **2007**, *8*, 484-493.

145. Spanhel, L., Colloidal ZnO Nanostructures and Functional Coatings: A Survey. *J Sol-Gel Sci Technol* **2006**, *39*, 7-24.

146. Ma, X.; Zhang, H.; Ji, Y.; Xu, J.; Yang, D., Sequential Occurrence of ZnO Nanopaticles, Nanorods, and Nanotips During Hydrothermal Process in a Dilute Aqueous Solution. *Materials Letters* **2005**, *59*, 3393-3397.

147. Kohls, M.; Bonanni, M.; Spanhel, L.; Su, D.; Giersig, M., Green Eriii Luminescence in Fractal ZnO Nanolattices. *Applied Physics Letters* **2002**, *81*, 3858-3860.

148. Xu, H.; Wang, H.; Zhang, Y.; Wang, S.; Zhu, M.; Yan, H., Asymmetric Twinning Crystals of Zinc Oxide Formed in a Hydrothermal Process. *Crystal Research and Technology* **2003**, *38*, 429-432.

149. Shingubara, S., Fabrication of Nanomaterials Using Porous Alumina Templates. *Journal of Nanoparticle Research* **2003**, *5*, 17-30.

150. Krunks, M.; Mellikov, E., Zinc Oxide Thin Films by the Spray Pyrolysis Method. *Thin Solid Films* **1995**, *270*, 33-36.

151. Ayouchi, R.; Martin, F.; Leinen, D.; Ramos-Barrado, J. R., Growth of Pure ZnO Thin Films Prepared by Chemical Spray Pyrolysis on Silicon. *Journal of Crystal Growth* **2003**, *247*, 497-504.

152. Lee, J.-H.; Leu, C.; Chung, Y.-W.; Hon, M.-H., Fabrication of Ordered ZnO Hierarchical Structures Controlled Via Surface Charge in the Electrophoretic Deposition Process. *Nanotechnology* **2006**, *17*, 4445.

153. Xu, S.; Wang, Z. L., One-Dimensional ZnO Nanostructures: Solution Growth and Functional Properties. *Nano Research* **2011**, *4*, 1013-1098.

154. Tam, K. H., et al., Defects in ZnO Nanorods Prepared by a Hydrothermal Method. *The Journal of Physical Chemistry B* **2006**, *110*, 20865-20871.

155. Amin, G.; Asif, M. H.; Zainelabdin, A.; Zaman, S.; Nur, O.; Willander, M., Influence of PH, Precursor Concentration, Growth Time, and Temperature on the Morphology of ZnO Nanostructures Grown by the Hydrothermal Method. *Journal of Nanomaterials* **2011**, *2011*.

156. Tao, Y.; Fu, M.; Zhao, A.; He, D.; Wang, Y., The Effect of Seed Layer on Morphology of ZnO Nanorod Arrays Grown by Hydrothermal Method. *Journal of Alloys and Compounds* **2010**, *489*, 99-102.

157. Usman Ali, S. M.; Nur, O.; Willander, M.; Danielsson, B., A Fast and Sensitive Potentiometric Glucose Microsensor Based on Glucose Oxidase Coated ZnO Nanowires Grown on a Thin Silver Wire. *Sensors and Actuators B: Chemical* **2010**, *145*, 869-874.

158. Israr, M. Q.; Sadaf, J. R.; Asif, M.; Nur, O.; Willander, M.; Danielsson, B., Potentiometric Cholesterol Biosensor Based on ZnO Nanorods Chemically Grown on Ag Wire. *Thin solid films* **2010**, *519*, 1106-1109.

159. Hafner, B., Energy Dispersive Spectroscopy on the SEM: A Primer. *Characterization Facility, University of Minnesota* **2006**, 1-26.

160. Australian Synchrotron, Synchrotron Science. http://www.synchrotron.org.au/synchrotron-science (accessed October 23, 2014).

161. Ozgur, U.; Hofstetter, D.; Morkoc, H., ZnO Devices and Applications: A Review of Current Status and Future Prospects. *Proceedings of the IEEE* **2010**, *98*, 1255-1268.

162. Zhang, D.; Chava, S.; Berven, C.; Lee, S. K.; Devitt, R.; Katkanant, V., Experimental Study of Electrical Properties of ZnO Nanowire Random Networks for Gas Sensing and Electronic Devices. *Applied Physics A* **2010**, *100*, 145-150.

163. Ahn, M. W.; Park, K. S.; Heo, J. H.; Park, J. G.; Kim, D. W.; Choi, K. J.; Lee, J. H.; Hong, S. H., Gas Sensing Properties of Defect-Controlled ZnO-Nanowire Gas Sensor. *Applied Physics Letters* **2008**, *93*, 263103-263103-3.

164. Hassan, J. J.; Mahdi, M. A.; Chin, C. W.; Abu-Hassan, H.; Hassan, Z., Room-Temperature Hydrogen Gas Sensor with ZnO Nanorod Arrays Grown on a Quartz Substrate. *Physica E: Low-dimensional Systems and Nanostructures* **2012**, *46*, 254-258.

165. Hassan, J. J.; Mahdi, M. A.; Chin, C. W.; Abu-Hassan, H.; Hassan, Z., Room Temperature Hydrogen Gas Sensor Based on ZnO Nanorod Arrays Grown on a SiO_2/Si Substrate Via a Microwave-Assisted Chemical Solution Method. *Journal of Alloys and Compounds* **2013**, *546*, 107-111.

166. Wang, J.; Sun, X.; Yang, Y.; Wu, C., N–P Transition Sensing Behaviors of ZnO Nanotubes Exposed to NO_2 Gas. *Nanotechnology* **2009**, *20*, 465501.

167. Wang, D.; Chu, X.; Gong, M., Hydrothermal Growth of ZnO Nanoscrewdrivers and Their Gas Sensing Properties. *Nanotechnology* **2007**, *18*, 185601.

168. Xiangfeng, C.; Dongli, J.; Djurišic, A. B.; Leung, Y. H., Gas-Sensing Properties of Thick Film Based on ZnO Nano-Tetrapods. *Chemical Physics Letters* **2005**, *401*, 426-429.

169. Han, N.; Chai, L.; Wang, Q.; Tian, Y.; Deng, P.; Chen, Y., Evaluating the Doping Effect of Fe, Ti and Sn on Gas Sensing Property of ZnO. *Sensors and Actuators B: Chemical* **2010**, *147*, 525-530.

170. Li, L. M.; Du, Z. F.; Wang, T. H., Enhanced Sensing Properties of Defect-Controlled ZnO Nanotetrapods Arising from Aluminum Doping. *Sensors and Actuators B: Chemical* **2010**, *147*, 165-169.

171. Ueda, T.; Plashnitsa, V. V.; Nakatou, M.; Miura, N., Zirconia-Based Amperometric Sensor Using ZnO Sensing-Electrode for Selective Detection of Propene. *Electrochemistry Communications* **2007**, *9*, 197-200.

172. Cheng, X.; Zhao, H.; Huo, L.; Gao, S.; Zhao, J., ZnO Nanoparticulate Thin Film: Preparation, Characterization and Gas-Sensing Property. *Sensors and Actuators B: Chemical* **2004**, *102*, 248-252.

173. Dhingra, M.; Kumar, L.; Shrivastava, S.; Kumar, P.; Annapoorni, S., Impact of Interfacial Interactions on Optical and Ammonia Sensing in Zinc Oxide/Polyaniline Structures. *Bull Mater Sci* **2013**, *36*, 647-652.

174. Wei, A.; Wang, Z.; Pan, L.-H.; Li, W.-W.; Xiong, L.; Dong, X.-C.; Huang, W., Room-Temperature NH_3 Gas Sensor Based on Hydrothermally Grown ZnO Nanorods. *Chinese Physics Letters* **2011**, *28*.

175. Greene, L. E.; Law, M.; Tan, D. H.; Montano, M.; Goldberger, J.; Somorjai, G.; Yang, P., General Route to Vertical ZnO Nanowire Arrays Using Textured ZnO Seeds. *Nano Letters* **2005**, *5*, 1231-1236.

176. Xu, S.; Lao, C.; Weintraub, B.; Wang, Z. L., Density-Controlled Growth of Aligned ZnO Nanowire Arrays by Seedless Chemical Approach on Smooth Surfaces. *Journal of Materials Research* **2008**, *23*, 2072-2077.

177. Drouin, D.; Couture, A. R.; Joly, D.; Tastet, X.; Aimez, V.; Gauvin, R., Casino V2. 42—a Fast and Easy-to-Use Modeling Tool for Scanning Electron Microscopy and Microanalysis Users. *Scanning* **2007**, *29*, 92-101.

178. Tarun, M.; Iqbal, M. Z.; McCluskey, M., Nitrogen Is a Deep Acceptor in ZnO. *AIP Advances* **2011**, *1*, 022105.

179. Ton-That, C.; Weston, L.; Phillips, M., Characteristics of Point Defects in the Green Luminescence from Zn-and O-Rich ZnO. *Physical Review B* **2012**, *86*, 115205.

180. Wang, X.; Vlasenko, L.; Pearton, S.; Chen, W.; Buyanova, I. A., Oxygen and Zinc Vacancies in as-Grown ZnO Single Crystals. *Journal of Physics D: Applied Physics* **2009**, *42*, 175411.

181. Morkoç, H.; Özgür, Ü., Zinc Oxide: Fundamentals, Materials and Device Technology; *Wiley*, 2009.

182. Foley, M.; Ton-That, C.; Phillips, M. R., Cathodoluminescence Inhomogeneity in ZnO Nanorods. *Applied Physics Letters* **2008**, *93*, 243104.

183. Phillips, M. R.; Gelhausen, O.; Goldys, E., Cathodoluminescence Properties of Zinc Oxide Nanoparticles. *Physica Status Solidi (a)* **2004**, *201*, 229-234.

184. Fabbri, F., et al., Zn Vacancy Induced Green Luminescence on Non-Polar Surfaces in ZnO Nanostructures. *Sci. Rep.* **2014**, *4*.

185. Wang, J.; Sun, X.; Yang, Y.; Huang, H.; Lee, Y.; Tan, O.; Vayssieres, L., Hydrothermally Grown Oriented ZnO Nanorod Arrays for Gas Sensing Applications. *Nanotechnology* **2006**, *17*, 4995.

186. Lin, Y.; Wang, D.; Zhao, Q.; Li, Z.; Ma, Y.; Yang, M., Influence of Adsorbed Oxygen on the Surface Photovoltage and Photoluminescence of ZnO Nanorods. *Nanotechnology* **2006**, *17*, 2110.

187. Bao, J.; Shalish, I.; Su, Z.; Gurwitz, R.; Capasso, F.; Wang, X.; Ren, Z., Photoinduced Oxygen Release and Persistent Photoconductivity in ZnO Nanowires. *Nanoscale Research Letters* **2011**, *6*, 1-7.

188. Yan, Y.; Al-Jassim, M.; Wei, S.-H., Oxygen-Vacancy Mediated Adsorption and Reactions of Molecular Oxygen on the ZnO ($10\bar{1}0$) Surface. *Physical Review B* **2005**, *72*, 161307.

189. Reyes, P. I.; Ku, C.-J.; Duan, Z.; Xu, Y.; Garfunkel, E.; Lu, Y., Reduction of Persistent Photoconductivity in ZnO Thin Film Transistor-Based UV Photodetector. *Applied Physics Letters* **2012**, *101*, 031118.

190. Li, C.; Zhang, D.; Lei, B.; Han, S.; Liu, X.; Zhou, C., Surface Treatment and Doping Dependence of In_2O_3 Nanowires as Ammonia Sensors. *The Journal of Physical Chemistry B* **2003**, *107*, 12451-12455.

191. Lavrov, E.; Herklotz, F.; Weber, J., Identification of Two Hydrogen Donors in ZnO. *Physical Review B* **2009**, *79*, 165210.

192. Fan, Z.; Dutta, D.; Chien, C.-J.; Chen, H.-Y.; Brown, E. C.; Chang, P.-C.; Lu, J. G., Electrical and Photoconductive Properties of Vertical ZnO Nanowires in High Density Arrays. *Applied Physics Letters* **2006**, *89*, 213110.

193. Fonoberov, V. A.; Balandin, A. A., ZnO Quantum Dots: Physical Properties and Optoelectronic Applications. *Journal of Nanoelectronics and Optoelectronics* **2006**, *1*, 19-38.

194. Pan, H.; Feng, Y. P., Semiconductor Nanowires and Nanotubes: Effects of Size and Surface-to-Volume Ratio. *ACS Nano* **2008**, *2*, 2410-2414.

195. Zhang, X.; Qin, J.; Xue, Y.; Yu, P.; Zhang, B.; Wang, L.; Liu, R., Effect of Aspect Ratio and Surface Defects on the Photocatalytic Activity of ZnO Nanorods. *Scientific Reports* **2014**, *4*.

196. Mönch, W., Semiconductor Surfaces and Interfaces, Springer Series in Surface Sciences; *Springer-Verlag Berlin Heidelberg*, **2001**; Vol. 26.

197. Zhang, Z.; Yates Jr, J. T., Band Bending in Semiconductors: Chemical and Physical Consequences at Surfaces and Interfaces. *Chemical Reviews* **2012**, *112*, 5520-5551.

198. Allen, M.; Swartz, C.; Myers, T.; Veal, T. D.; McConville, C. F.; Durbin, S., Bulk Transport Measurements in ZnO: The Effect of Surface Electron Layers. *Physical Review B* **2010**, *81*, 075211.

199. Heinhold, R.; Williams, G.; Cooil, S.; Evans, D.; Allen, M., Influence of Polarity and Hydroxyl Termination on the Band Bending at ZnO Surfaces. *Physical Review B* **2013**, *88*, 235315.

200. Heinhold, R.; Cooil, S. P.; Evans, D. A.; Allen, M. W., Stability of the Surface Electron Accumulation Layers on the Nonpolar $(10\bar{1}0)$ and $(11\bar{2}0)$ Faces of ZnO. *The Journal of Physical Chemistry C* **2014**, *118*, 24575-24582.

201. Chen, M.-W.; Retamal, J. R. D.; Chen, C.-Y.; He, H., Photocarrier Relaxation Behavior of a Single ZnO Nanowire UV Photodetector: Effect of Surface Band Bending. *Electron Device Letters, IEEE* **2012**, *33*, 411-413.

202. Liao, Z.-M.; Liu, K.-J.; Zhang, J.-M.; Xu, J.; Yu, D.-P., Effect of Surface States on Electron Transport in Individual ZnO Nanowires. *Physics Letters A* **2007**, *367*, 207-210.

203. Li, Q.; Gao, T.; Wang, Y.; Wang, T., Adsorption and Desorption of Oxygen Probed from ZnO Nanowire Films by Photocurrent Measurements. *Applied Physics Letters* **2005**, *86*, 123117.

204. Fan, Z.; Wang, D.; Chang, P.-C.; Tseng, W.-Y.; Lu, J. G., ZnO Nanowire Field-Effect Transistor and Oxygen Sensing Property. *Applied Physics Letters* **2004**, *85*, 5923-5925.

205. Li, Y.; Della Valle, F.; Simonnet, M.; Yamada, I.; Delaunay, J.-J., Competitive Surface Effects of Oxygen and Water on UV Photoresponse of ZnO Nanowires. *Applied Physics Letters* **2009**, *94*, 023110.

206. Chen, C.-Y.; Retamal, J. R. D.; Wu, I.-W.; Lien, D.-H.; Chen, M.-W.; Ding, Y.; Chueh, Y.-L.; Wu, C.-I.; He, J.-H., Probing Surface Band Bending of Surface-Engineered Metal Oxide Nanowires. *ACS Nano* **2012**, *6*, 9366-9372.

207. Bao, J.; Shalish, I.; Su, Z.; Gurwitz, R.; Capasso, F.; Wang, X.; Ren, Z., Photoinduced Oxygen Release and Persistent Photoconductivity in ZnO Nanowires. *Nanoscale Res. Lett* **2011**, *61*, 404.

208. Xu, H.; Fan, W.; Rosa, A.; Zhang, R.; Frauenheim, T., Hydrogen and Oxygen Adsorption on ZnO Nanowires: A First-Principles Study. *Physical Review B* **2009**, *79*, 073402.

209. Gurwitz, R.; Cohen, R.; Shalish, I., Interaction of Light with the ZnO Surface: Photon Induced Oxygen "Breathing," Oxygen Vacancies, Persistent Photoconductivity, and Persistent Photovoltage. *Journal of Applied Physics* **2014**, *115*, 033701.

210. Moormann, H.; Kohl, D.; Heiland, G., Work Function and Band Bending on Clean Cleaved Zinc Oxide Surfaces. *Surface Science* **1979**, *80*, 261-264.

211. An, W.; Wu, X.; Zeng, X., Adsorption of O_2, H_2, CO, NH_3, and NO_2 on ZnO Nanotube: A Density Functional Theory Study. *The Journal of Physical Chemistry C* **2008**, *112*, 5747-5755.

212. Spencer, M. J.; Wong, K. W.; Yarovsky, I., Surface Defects on ZnO Nanowires: Implications for Design of Sensors. *Journal of Physics: Condensed Matter* **2012**, *24*, 305001.

213. Collins, R.; Thomas, D., Photoconduction and Surface Effects with Zinc Oxide Crystals. *Physical Review* **1958**, *112*, 388.

214. Chen, D.; Wang, Z.; Ren, T.; Ding, H.; Yao, W.; Zong, R.; Zhu, Y., Influence of Defects on the Photocatalytic Activity of ZnO. *The Journal of Physical Chemistry C* **2014**, *118*, 15300-15307.

215. Willander, M.; Nur, O.; Sadaf, J. R.; Qadir, M. I.; Zaman, S.; Zainelabdin, A.; Bano, N.; Hussain, I., Luminescence from Zinc Oxide Nanostructures and Polymers and Their Hybrid Devices. *Materials* **2010**, *3*, 2643-2667.

216. Fabbri, F.; Villani, M.; Catellani, A.; Calzolari, A.; Cicero, G.; Calestani, D.; Calestani, G.; Zappettini, A.; Dierre, B.; Sekiguchi, T., Zn Vacancy Induced Green

Luminescence on Non-Polar Surfaces in ZnO Nanostructures. *Scientific Reports* **2014**, *4*.

217. Giles, N.; Xu, C.; Callahan, M.; Wang, B.; Neal, J. S.; Boatner, L. A., Effects of Phonon Coupling and Free Carriers on Band-Edge Emission at Room Temperature in N-Type ZnO Crystals. *Applied Physics Letters* **2006**, *89*, 251906-251906-3.

218. Hu, H.; Ji, H.-F.; Sun, Y., The Effect of Oxygen Vacancies on Water Wettability of a ZnO Surface. *Phys. Chem. Chem. Phys.* **2013**, *15*, 16557-16565.

219. Kiasari, N. M.; Soltanian, S.; Gholamkhass, B.; Servati, P., Room Temperature Ultra-Sensitive Resistive Humidity Sensor Based on Single Zinc Oxide Nanowire. *Sensors and Actuators A: Physical* **2012**, *182*, 101-105.

220. Chen, Q.; Lu, W.; Wu, Y.-k.; Ding, H.-y.; Wang, B.; Chen, L., Probe the Effects of Surface Adsorbates on ZnO Nanowire Conductivity Using Dielectric Force Microscopy. *Chinese Journal of Chemical Physics* **2014**, *27*, 582-586.

221. Murphy, D. M., Metal Oxide Catalysis (Edited by S. D. Jackson and J. S. J. Hargreaves); *Wiley VCH Verlag GmbH & Co. KGaA, Weinheim*, *Germany*, **2008**.

222. Djurišić, A. B.; Leung, Y. H.; Choy, W. C.; Cheah, K. W.; Chan, W. K., Visible Photoluminescence in ZnO Tetrapod and Multipod Structures. *Applied Physics Letters* **2004**, *84*, 2635-2637.

223. Pöppl, A.; Völkel, G., ESR and Photo-ESR Investigations of Zinc Vacancies and Interstitial Oxygen Ions in Undoped ZnO Ceramics. *Physica Status Solidi (a)* **1991**, *125*, 571-581.

224. Larina, L.; Tsvetkov, N.; Yang, J.; Lim, K.-S.; Shevaleevskiy, O., Electron Paramagnetic Resonance Studies of Shallow Donors Behavior in Hydrogenated ZnO Films. *ECS Transactions* **2010**, *28*, 161-167.

225. Geisler, C.; Simmons, G., High Temperature Induced EPR Signals in Zinc Oxide. *Physics Letters* **1964**, *11*, 111-112.

226. Neumann, G., Current Topics in Materials Science, Edited by E. Kaldis. *North-Holland, Amsterdam* **1981**, 269.

227. Erhart, P.; Albe, K., Diffusion of Zinc Vacancies and Interstitials in Zinc Oxide. *Applied Physics Letters* **2006**, *88*, 201918.

228. Smith, J.; Vehse, W., ESR of Electron Irradiated ZnO Confirmation of the F^{+} Center. *Physics Letters A* **1970**, *31*, 147-148.

229. Kotsis, K.; Staemmler, V., Ab Initio Calculations of the O1s XPS Spectra of ZnO and Zn Oxo Compounds. *Physical Chemistry Chemical Physics* **2006**, *8*, 1490-1498.

230. Kumar, V.; Swart, H.; Ntwaeaborwa, O.; Kroon, R.; Terblans, J.; Shaat, S.; Yousif, A.; Duvenhage, M., Origin of the Red Emission in Zinc Oxide Nanophosphors. *Materials Letters* **2013**, *101*, 57-60.

231. Kim, Y.-S.; Tai, W.-P.; Shu, S.-J., Effect of Preheating Temperature on Structural and Optical Properties of ZnO Thin Films by Sol–Gel Process. *Thin Solid Films* **2005**, *491*, 153-160.

232. Wei, X.; Man, B.; Liu, M.; Xue, C.; Zhuang, H.; Yang, C., Blue Luminescent Centers and Microstructural Evaluation by XPS and Raman in ZnO Thin Films Annealed in Vacuum, N_2 and O_2. *Physica B: Condensed Matter* **2007**, *388*, 145-152.

233. Li, G.; Yi, Z.; Wang, H.; Jia, C.; Zhang, W., Factors Impacted on Anisotropic Photocatalytic Oxidization Activity of ZnO: Surface Band Bending, Surface Free Energy and Surface Conductance. *Applied Catalysis B: Environmental* **2014**, *158*, 280-285.

234. Ton-That, C.; Phillips, M. R.; Foley, M.; Moody, S. J.; Stampfl, A. P., Surface Electronic Properties of ZnO Nanoparticles. *Applied Physics Letters* **2008**, *92*, 261916.

235. Girard, R.; Tjernberg, O.; Chiaia, G.; Söderholm, S.; Karlsson, U. O.; Wigren, C.; Nylen, H.; Lindau, I., Electronic Structure of ZnO (0001) Studied by Angle-Resolved Photoelectron Spectroscopy. *Surface Science* **1997**, *373*, 409-417.

236. Chiou, J.; Tsai, H.; Pao, C.; Kumar, K. K.; Ray, S.; Chien, F.; Pong, W.-F.; Tsai, M.-H.; Chen, C.-H.; Lin, H.-J., Comparison of the Electronic Structures of $Zn_{1-X}Co_xO$ and $Zn_{1-X}Mg_xO$ Nanorods Using X-Ray Absorption and Scanning Photoelectron Microscopies. *Applied Physics Letters* **2006**, *89*, 043121.

237. Song, S.; Hong, W.-K.; Kwon, S.-S.; Lee, T., Passivation Effects on ZnO Nanowire Field Effect Transistors under Oxygen, Ambient, and Vacuum Environments. *Applied Physics Letters* **2008**, *92*, 263109.

238. Stavale, F.; Pascua, L.; Nilius, N.; Freund, H.-J., Luminescence Properties of Nitrogen-Doped ZnO. *The Journal of Physical Chemistry C* **2014**, *118*, 13693-13696.

239. Choi, S.; Johnson, B. C.; Castelletto, S.; Ton-That, C.; Phillips, M. R.; Aharonovich, I., Single Photon Emission from ZnO Nanoparticles. *Applied Physics Letters* **2014**, *104*, 261101.

240. Kik, P.; Polman, A., Exciton–Erbium Energy Transfer in Si Nanocrystal-Doped SiO$_2$. *Materials Science and Engineering: B* **2001**, *81*, 3-8.

241. Shionoya, S.; Goldberg, P., Luminescence of Inorganic Solids. *Academic, New York* **1966**, 205.

242. Alemán, B.; Ortega, Y.; García, J. Á.; Fernández, P.; Piqueras, J., Fe Solubility, Growth Mechanism, and Luminescence of Fe Doped ZnO Nanowires and Nanorods Grown by Evaporation-Deposition. *Journal of Applied Physics* **2011**, *110*, 014317.

243. Müller, S.; Zhou, M.; Li, Q.; Ronning, C., Intra-Shell Luminescence of Transition-Metal-Implanted Zinc Oxide Nanowires. *Nanotechnology* **2009**, *20*, 135704.

244. Kurbanov, S. S.; Kang, T. W., Spectral Behavior of the Emission around 3.31 eV (a-Line) from ZnO Nanocrystals. *Journal of Luminescence* **2010**, *130*, 767-770.

245. Tainoff, D.; Masenelli, B.; Mélinon, P.; Belsky, A.; Ledoux, G.; Amans, D.; Dujardin, C.; Fedorov, N.; Martin, P., Competition between Exciton-Phonon Interaction and Defects States in the 3.31 eV Band in ZnO. *Physical Review B* **2010**, *81*, 115304.

246. Bebb, H. B.; Williams, E., Semiconductors and Semimetals. *Academic Press, New York* **1972**, *8*, 181.

247. Shibata, H., Negative Thermal Quenching Curves in Photoluminescence of Solids. *Japanese Journal of Applied Physics* **1998**, *37*, 550.